



TECHNISCHE UNIVERSITÄT MÜNCHEN
Fakultät für Maschinenwesen
Lehrstuhl für Carbon Composites

Forming simulation of AFP material layups: Material characterization, simulation and validation

Daniel Maurice Leutz

Vollständiger Abdruck der von der Fakultät für Maschinenwesen der Technischen Universität München zur Erlangung des akademischen Grades eines

Doktor-Ingenieurs

genehmigten Dissertation.

Vorsitzender: Prof. Dr.-Ing. Manfred Hajek

Prüfer der Dissertation: Prof. Dr.-Ing. Klaus Drechsler
Prof. Philippe Boisse, Ph.D.

Die Dissertation wurde am 01.09.2015 bei der Technischen Universität München eingereicht und durch die Fakultät für Maschinenwesen am 11.04.2016 angenommen.

Technische Universität München
Fakultät für Maschinenwesen
Lehrstuhl für Carbon Composites
Boltzmannstraße 15
D-85748 Garching bei München

Tel.: +49 (0) 89 / 289 – 15092

Fax.: +49 (0) 89 / 289 – 15097

Email: info@lcc.mw.tum.de

Web: www.lcc.mw.tum.de

Acknowledgment

The intention of my acknowledgment is to thank those persons whose support and encouragement have been with me in the last couple of years. My deepest apologies in advance if I happened to leave anyone aside.

The work presented in this thesis was carried out between the years 2009 and 2013 at the Institute for Carbon Composites of the Technische Universität München. The support by General Electric Global Research is gratefully acknowledged.

First, I would like to express my sincere thanks and gratitude to Prof. Dr.-Ing. Klaus Drechsler. Without his support and his kindness this work would never be accomplished. I am also thankful to Prof. Philippe Boisse from LaMCoS of INSA Lyon for agreeing to be second advisor and for his time and interest to review my work.

I would also like to thank Dr.-Ing. Roland Hinterhölzl for his guidance and our fruitful discussions during my time at the LCC. My thanks are also addressed to Dr. mont. Elisabeth Ladstätter and the team assistants of the LCC for their organizational support during my dissertation and beyond.

I am also very grateful to my colleagues and friends at the LCC. Their work and support contributed directly or indirectly to this thesis. And I owe a special thank to Sylvain Bel and Alexane Margossian. Our discussions and teamwork were an important part throughout my whole work. I also thank all my students who supported this work with their theses.

I owe an important debt to Mark Vermilyea. Without his generous support and his helpful comments this thesis would not have been possible.

Finally, I would like to thank my family and my wife for their backing and patience during my dissertation.

Übersicht

Das Automated Fiber Placement (AFP) Verfahren zielt darauf ab große Bauteile aus kohlenstofffaserverstärkten Kunststoffen lastgerecht und direkt herzustellen. Jedoch kann das Verfahren auch genutzt werden, um flächige Lagenaufbauten herzustellen und diese dann in einem nachfolgenden Umformprozess in Bauteilform zu bringen. Diese Methode eignet sich gerade für kleinere, komplexere Geometrien. In der vorliegenden Arbeit wird beschrieben, wie mittels einer Finiten-Element-Simulation die Entwicklung dieses Umformprozesses unterstützt werden kann. Eine geeignete Materialmodellierung wird präsentiert, welche das Umformverhalten der AFP-Einzelschichten aber auch -Laminats beschreiben kann. Die Arbeit befasst sich zudem mit der Materialcharakterisierung der Laminats zur Bestimmung der für die Simulation notwendigen Materialparameter. Dies beinhaltet unter anderem die Wahl geeigneter Prüfverfahren, deren Durchführung, sowie die Auswertung und Interpretation der Versuchsergebnisse. Die ermittelten Materialparameter werden durch Simulationen der Materialprüfungen abgeglichen und anschließend anhand zwei generischer Umformgeometrien validiert. Der Abgleich erfolgt durch die Faserausrichtung, welche im Experiment durch einen optischen Sensor ermittelt wird. Abschließend wird das Materialmodell angewandt, um den Umformprozess eines gekrümmten L- und Z-Profils zu simulieren und mit Umformexperimenten zu vergleichen. Ein CT-Scanner wird verwendet, um die Umformung des Laminats während des Prozesses und die Verschiebung der einzelnen Lagen zueinander zu untersuchen.

Abstract

The Automated Fiber Placement (AFP) process aims to directly produce load optimized large components made of carbon fiber reinforced plastics. However, this process can also be used to produce planar laminates, which are formed in a subsequent step into the final geometry. The latter method is suitable for smaller and more complex geometries. The present work describes a method of how to apply a Finite-Element simulation for supporting the development of this forming process. A suitable material modeling is presented, which allows describing the deformation behavior of the AFP laminates. The work also deals with the material characterization of the laminates, to determine the necessary material parameters for the simulation. This includes, among other things, the selection and development of appropriate test methods and the evaluation and interpretation of the experimental results. The material parameters obtained are compared with simulations of the material characterization tests, recalibrated if needed and finally validated using two generic forming geometries. The comparison is made through the fiber orientation, which is determined in the experiment by an optical sensor. Finally, the material model is used to simulate the forming process of a curved L- and Z-flange and compared with experiments. For this purpose a CT scanner is used to analyze the deformation of the laminate during the forming process and the displacement of the individual layers to each another.

Table of Contents

Nomenclature	xiii
Table of Figures.....	xvii
Table of Tables	xxiii
1 Introduction	25
1.1 Motivation.....	25
1.2 Objectives of thesis	28
1.3 Outline of the thesis	28
2 Composite textiles draping	31
2.1 Deformation modes and mechanisms	31
2.1.1 Intra-ply shear.....	32
2.1.2 Out-of-plane bending.....	35
2.1.3 In-plane tension and compression	38
2.1.4 Inter-ply movement / frictional behavior.....	41
2.1.5 Out-of-plane compression / compaction.....	43
2.2 Defects	44
3 Draping Simulation	47
3.1 Requirements for a draping simulation.....	48
3.2 Numerical approaches.....	49
3.2.1 Kinematic approach	49
3.2.2 Finite Element approach.....	52
3.3 Selected simulation approach	55
3.4 Description of PAM-FORM	55
4 Material characterization	59
4.1 Shear characterization.....	60
4.1.1 Tests methods	61
4.1.2 Test results	67

4.2	Bending Test	74
4.2.1	Test methods	74
4.2.2	Test results	77
4.3	Friction Test	78
4.3.1	Test methods	79
4.3.2	Test Results	81
4.4	Tensile Test	83
4.4.1	Test methods	83
4.4.2	Test results	85
4.5	Thickness measurement	87
4.6	Conclusion.....	88
5	Material characterization simulation.....	91
5.1	Friction test simulation.....	92
5.2	Tensile test simulation.....	94
5.3	Bending test simulation.....	97
5.4	Picture Frame Test simulation.....	103
5.5	Final material card.....	108
5.6	Conclusion.....	109
6	Validation	111
6.1	Experiments.....	111
6.1.1	Geometries	112
6.1.2	Forming process.....	112
6.2	Simulation	113
6.3	Comparison method	113
6.3.1	Measurement method.....	114
6.3.2	MATLAB routine	116
6.4	Validation with the hemisphere.....	118
6.4.1	Experiment.....	118
6.4.2	Simulation.....	119
6.4.3	Comparison.....	121
6.5	Validation with the Double Sine	126

6.5.1	Experiment.....	126
6.5.2	Simulation.....	127
6.5.3	Comparison.....	127
6.6	Conclusion	132
7	Flange forming simulation.....	135
7.1	Forming process.....	136
7.2	Simulation model	137
7.2.1	Model setup	137
7.2.2	Meshing technique.....	138
7.3	Results.....	141
7.4	Conclusion	149
8	Discussion	151
9	Summary and Outlook	155
	Literature.....	157
A	Appendix.....	167
B	Publications	169
C	Advised student works	171

Nomenclature

Abbreviations

AFP	Automated Fiber Placement
BET	Bias Extension Test
BC	Boundary condition
CT	Computer tomography
CTL	Composite Test Laboratory (LCC facility)
DIN	Deutsches Institut für Normung
DMA	Dynamical Analyzing Machine
DOF	Degrees of freedom
FE / FEM	Finite Element / Finite Element Method
GUI	Graphical user interface
KES-F	Kawabata Evaluation System for fabrics
LCC	Lehrstuhl für Carbon Composites / Institute for Carbon Composites
NCF	Non-crimp fabric
PFT	Picture Frame Test
RUC	Representative unit cell
STD	Standard deviation
UD	Unidirectional

Scalars

Symbol	Unit	Description
B	$\text{N}\cdot\text{mm}^2$	Bending stiffness/rigidity
E	N/mm	Young's modulus (isotropic materials)
F	N	Force
G	N/mm	Shear modulus
He	-	Hersey number
I	mm^4	Second moment of area
N	N	Normal force (for friction)
$T_{c/f}$	$^{\circ}\text{C}$ or $^{\circ}\text{F}$	Temperature
T_{osci}	s or ms	Time period of oscillation
b	mm	Width
c	mm	Bending length
d	mm	Displacement
g	mm/s^2	Normal gravity
l	mm	Length
m	kg	Mass
q	1/s	Damping factor
t	mm	Thickness
v	mm/ms	Velocity
w_a	kg/mm^2	Weight per unit area
x	m	Stroke / displacement
ε	-	Strain
η	$\text{mPa}\cdot\text{s}$	Viscosity
θ	$^{\circ}$	Shear angle
μ	-	Coulomb friction coefficient

σ	N/mm ²	Normal stress
τ	N/mm ²	Shear stress
ν	-	Poisson's ratio
ϕ	°	Frame angle
ψ	°	Tangent angle in a cantilevered beam

Subscripts

0	Initial / reference value
$1 / f$	Fiber direction 1
$2 / m$	Fiber direction 2 or transverse direction
a	Area
cor	Correction
$crit$	Critical
dy	Dynamic
$fric$	Frictional
$hydro$	Hydrodynamic
i	Counter variable / node number
l	Length
ln	Logarithmic
$lock$	Locking
m	Machine
n	Normal direction
$osci$	Oscillation
PF	Picture Frame
red	Reduction

<i>s</i>	Shear
<i>st</i>	Static
<i>t</i>	Tensile/tension
<i>w</i>	Width

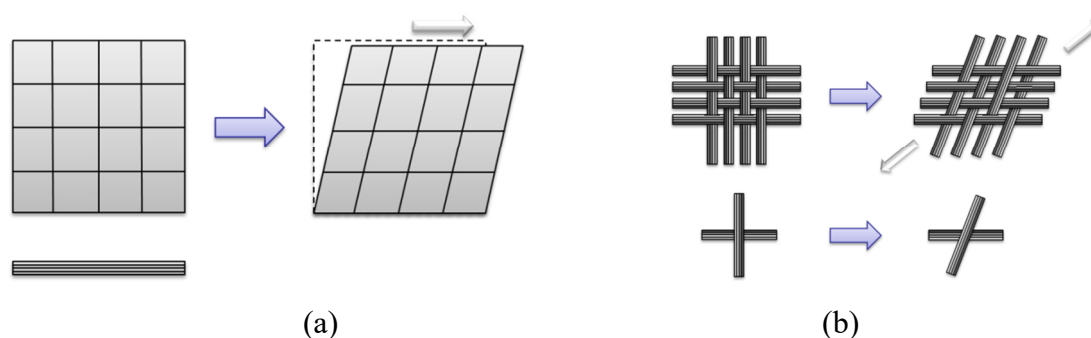


Fig. 2-1 Shear deformation of composite textiles
 (a) macro level; (b) meso level [19]

When a shear deformation is applied on woven fabrics a rotation of warp and weft yarns at their crossings takes place and no shear of the yarn itself [11, 20]. In the first stage of shearing the shear force is governed by dry friction between the tows. For pre-impregnated fabrics lubricated friction takes place [18]. The shear force is directly linked to the number of crossing points in the fabric [8, 21]. A dense woven fabric (e.g. plain weave) evolves a higher shear force than a loose fabric with less crossing points (e.g. satin weave). Further shearing the fabric brings the tows in contact till they compress each other (fiber jamming), leading to a fast increase of the shear force (Fig. 2-2).



Fig. 2-2 Different states in shearing a woven fabric
 Initial state; sheared state; sheared up to locking angle; further shearing leading to fiber jamming (from left to right)

Fig. 2-3 shows exemplarily the non-linear shear behavior of different woven fabrics as a function of shear force F_s versus shear angle θ . The shear angle defines the deviation of the initial angle between the two fiber directions and the current fiber angle. All fabrics show a low shear resistance at the beginning but stiffen rapidly at a certain point. In literature this point is often called “locking angle” and described as the maximum shear angle after which wrinkles occur if further shear is applied on the textile. The author of this work does not support the theory of the locking angle since the initiation of wrinkle formation cannot be described by a single value. Launay [22], Hivet [23] and Lomov [24, 25] performed shear tests on woven fabrics while varying the tension in the fibers. By increasing the tension in the fibers the shear force increases and the formation of wrinkles starts later. This effect is also utilized in automated forming processes by including a blankholder which increases the in-plane tension within the textile.

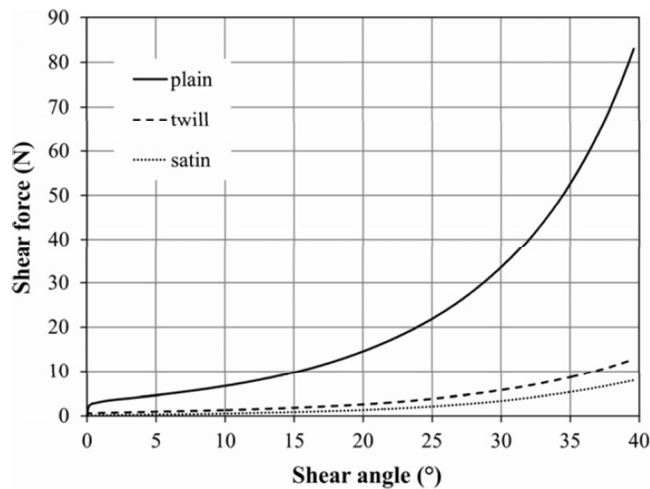


Fig. 2-3 Shear curves of three different woven fabrics determined with the picture frame test [15]

The shear behavior of UD preregs cannot be described by the shear mechanics of woven fabrics. By shearing UD preregs fiber sliding takes place instead of rotating to each other. While the compound in woven fabrics is held together by the warp and weft yarns themselves, the fibers in UD prepeg are only held together by the matrix. The shear is consequently governed by the matrix properties and thus shows a viscous behavior with rate and temperature dependency [18]. This shear mechanism only allows a simple shear in longitudinal direction. Fig. 2-4 describes the deformations which would take place for simple and pure shear of UD preregs. The high stiffness of the fibers does not allow any strain in fiber direction. A compression in matrix direction can be hardly achieved since it rather leads to buckling of the material. Hence, only the simple shear deformation is possible.

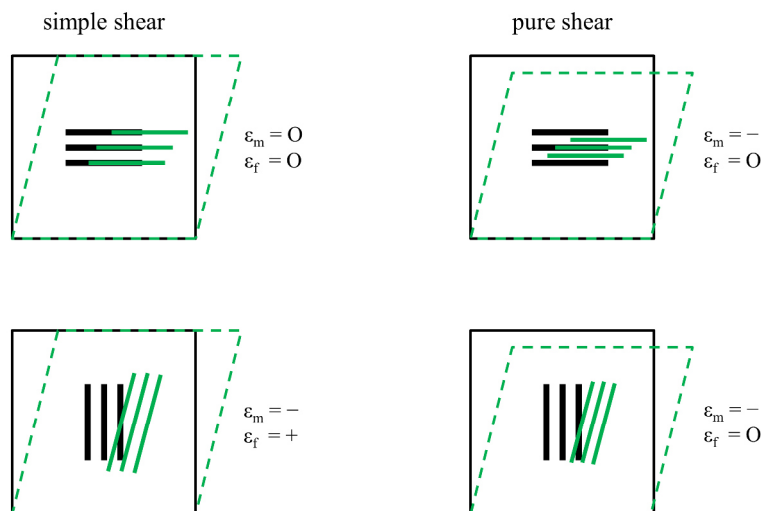


Fig. 2-4 Principle of simple shear and pure shear for a UD prepeg
 ϵ_m = matrix strain; ϵ_f = fiber strain; '+' = tensile strain; 'O' = no strain; '-' = compressive strain

The shear forces and accordingly the shear stiffness of UD prepregs are much higher than for dry textiles because the tackiness of the matrix inhibits the fibers in sliding to each other. Even if no fiber jamming like in woven fabrics shearing occurs they still show a non-linear shear behavior. Haanappel [26] performed shear tests in a rheometer and evidenced a non-linear behavior even at small shear strains.

The shear behavior of AFP materials is comparable to UD prepregs with respect to single tows. But regarding AFP layups placed in a UD manner behave different as UD prepregs. The bonding between adjacent tows is very low and acts as a weak point in the layup. As a consequence, no shear force can be transferred between the tows such that the tows slip to each other rather than shear within a single tow (Fig. 2-5).

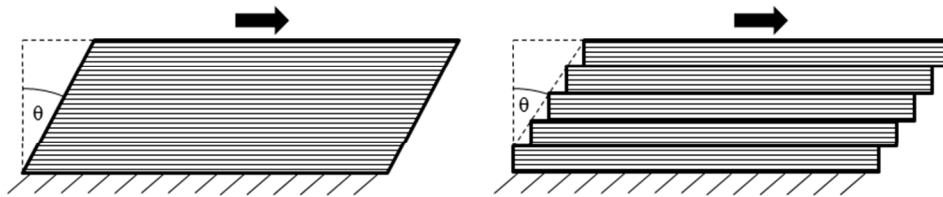


Fig. 2-5 **Shear of UD materials**
UD prepeg (left); AFP material layup (right)

The above mentioned deformation mechanism describes the in-plane shear which is the governing shear for thin materials. Nevertheless, out-of-plane (transversal) shear also occurs during forming. It is a minor deformation and mainly shows up in bending deformation. Therefore this deformation mode will be addressed in the next chapter.

2.1.2 Out-of-plane bending

When forming a textile over a single curvature it mainly undergoes a bending deformation [7, 27]. Bending is the governing out-of-plane deformation mode during forming. In most cases only small forces are needed to bend the material to a large extent. The bending stiffness (also called “bending rigidity” or “flexural rigidity”) is influencing the formation and shape of folds and wrinkles [28, 29]. It is dependent on the yarn properties, the textile structure, the matrix, and the contact behavior [15, 30].

The bending mechanism of textile structures cannot be compared to the bending of homogenous materials. Bilbao [31] and Ghosh [32] describe it as a multiscale hierarchical problem. During bending the fibrous structure of the textile changes due to fibers and tows sliding relative to each other. On micro-scale the single fibers are bending individually. On meso-scale (yarn bending) the bending stiffness cannot be assumed to be the sum of all fiber stiffness. Since they are interacting with each other the yarn behaves different. On macro-scale bending of ply stacks lead additionally to a relative slippage of the plies [7]. Akkerman [12] describes the bending of a laminate somewhere between Kirchhoff bending and transversal shear (Fig. 2-6).



Fig. 2-6 Laminate bending modes
Kirchoff bending (left), with intra-ply shear (center) and a combination with inter-ply shear (right) [12]

In this work only the macroscopic bending will be considered. A mathematical description of this bending behavior is not straight forward. The Euler-Bernoulli beam theory cannot be applied since it only accounts for linear material behavior and small deflections. In case of textile bending usually high deflections and deformations are occurring. Further, the simple beam theory describes the bending stiffness B as the product of the tensile Young's modulus E and the second moment of area I :

$$B = E * I \quad (2-1)$$

For textiles the bending stiffness is independent of the in-plane properties since the textile structure changes during bending [33]. Depending on the kind of textile it also shows an orthotropic behavior, meaning different bending stiffness for warp and weft direction [34]. This effect is seen heavily for UD prepregs. In fiber direction they exhibit a high bending stiffness with the fibers carrying the main load. In perpendicular direction (matrix direction) only the matrix, which is non-cured and soft during forming, carries the load (cf. 4.1.2).

Most mathematical descriptions for the bending of textiles are based on the work of Peirce in 1930 [34]. He describes the bending of a cantilevered textile strip deflected by its own weight (Fig. 2-7).

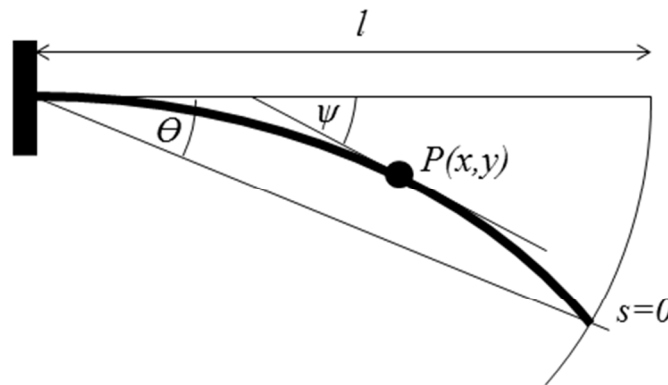


Fig. 2-7 Cantilever test
Definitions according to Peirce [34]

With $s(0:l)$ as the distance of any point $P(x,y)$ along the cantilever and ψ the tangent angle at P , the curvature at P is $d\psi/ds$. The bending moment at P can be described by $-B_w d\psi/ds$. Here, B_w is defined as the bending stiffness (or flexural rigidity) for unit

curvature per unit width. With a change of s by a small amount δs , the change of the bending moment $\delta(-B_w d\psi/ds)$ is equal the change of the moment resulting from the overhanging weight $ws \cos \psi \delta s$. The weight per unit area is denoted by w_a . This leads to the second order differential equation:

$$\frac{d^2\psi}{ds^2} = -\frac{w_a}{B_w} s \cos \psi \tag{2-2}$$

The ratio B_w/w_a represents the property of the material. Textiles which have the same ratio will bend to the same degree. Peirce denominates the ratio by S which has units of length cubed. He denotes its cube root as the bending length c . Please note that even though the bending length c has the unit length it is only a quantitative value not a measurable geometrical length.

$$S = B_w/w_a = c^3 \tag{2-3}$$

The bending length characterizes the bending behavior of the textile. The higher the bending length value the stiffer the textile and vice versa.

Equation (2-2) cannot be solved analytically. Szablewski and Kobza [35] used the Shooting Method to solve the equation numerically. Morton and Hummel [36] performed different tests and applied a Taylor series to derive a satisfying approximation of the equation:

$$S = l^3 \frac{\cos(\frac{1}{2} \theta)}{8 \tan \theta} \tag{2-4}$$

This equation can be further simplified if a bending angle of $\theta = 43^\circ$ is used [35].

$$S = \frac{l^3}{8} \tag{2-5}$$

It has to be noted that eq.(2-4) is an approximation. Other publications [31, 37, 38] are defining the bending angle $\theta = 41,5^\circ$ to derive the simplified eq.(2-5). In this work $\theta = 41,5^\circ$ will be used since the bending test used in this work (cf. 4.2.1) is based on that.

Including eq.(2-5) in eq. (2-3) the bending stiffness B_w per unit width is:

$$B_w = \frac{l^3}{8} * w_a \tag{2-6}$$

With the specimen thickness t the bending modulus E_b is defined as:

$$E_b = \frac{12 * B_w}{t^3} \quad (2-7)$$

Substituting B_w with the bending stiffness B divided by the width b leads to:

$$E_b = \frac{12 * B}{b * t^3} \quad (2-8)$$

Assuming a rectangular cross section of the specimen the term $(12/b * t^3)$ equals the second moment of area I and leading to the familiar equation:

$$B = E_b * I \quad (2-9)$$

By comparing this relationship with eq. (2-1) shows the difference of bending a textile and a homogenous material. As mentioned above the bending stiffness of a textile cannot be derived via the Young's modulus of the in-plane properties.

The derivation of the bending stiffness shown here was done for a certain bending angle of $41,5^\circ$. Using a different bending angle would lead to a change in the bending stiffness. Especially for high deformations the bending behavior has a non-linear characteristic [27]. For example the KES-FB2 bending test of Kawabata [39] measures the bending moment for different bending curvatures revealing the non-linear bending behavior of the material. Fig. 2-8 shows an exemplary output of the KES-FB2 test.

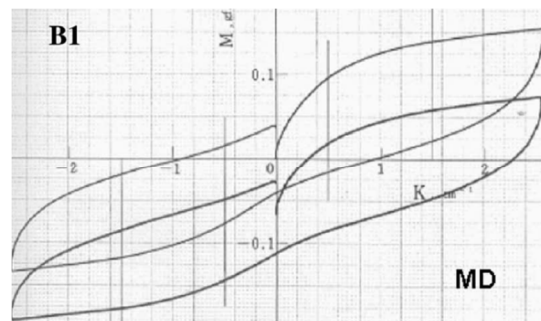


Fig. 2-8 **Result of a KES-FB2**
Plot showing the bending moment vs. the bending curvature [40]

2.1.3 In-plane tension and compression

In comparison to intra-ply shear less attention to the tensile behavior of composite textiles is given in literature. Depending on the kind of material the tensile behavior can have more or less influence on the draping behavior.

A UD material or a NCF provide an almost linear stress-strain response if a tensile load is applied in fiber direction (Fig. 2-9). It exhibits in a high tensile stiffness and Young's modulus, respectively. Even if the strain is negligible small the high stresses influence the draping behavior. With continuous fibers the stresses transmit forces

throughout the whole textile and influence the formation of wrinkles, the shear behavior and fiber slippage.

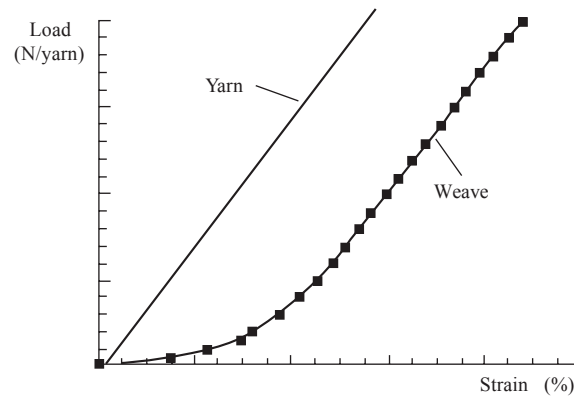


Fig. 2-9 Differences of tensile response of a yarn and a woven fabric
The yarn behavior equals the behavior of a NCF or a UD loaded in fiber direction [41]

The tensile behavior of woven fabrics is different especially in the first stage [42]. With a relatively small load in fiber direction the initially undulated yarns get straightened (Fig. 2-10). Subsequent loading applies direct tensile loading on the yarns which results in the same stress-strain behavior as for UD materials or NCFs (Fig. 2-9). The course of the stress-strain curve is not consistent because it depends on the stress state in the other fiber direction. When applying a tensile load in weft direction the warp direction shows a stiffer behavior especially in the straightening phase [42].

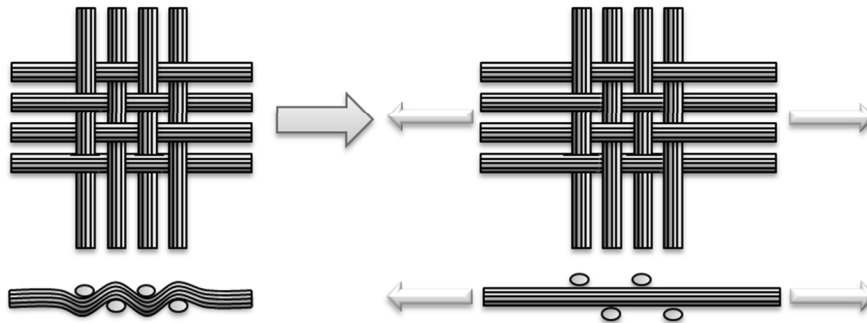


Fig. 2-10 Fiber straightening in a woven fabric under tensile loading [19]

The tensile behavior of UD preregs in fiber direction is similar to the behavior of a NCF. In perpendicular direction the matrix properties governs the tensile behavior. Hence, it is strongly rate and temperature dependent. Solely the matrix holds the fibers together and consequently bears only small loads. Fig. 2-11 shows the characteristic behavior of an UD prepreg loaded in matrix/transverse direction. It evolves an almost linear behavior up to a certain strain after which the material starts to tear apart and the load decreases. In the linear state an elongation of the matrix takes place. In the further course tearing starts at local points leading to a decrease of the cross-sectional area such that smaller loads are needed to further strain the material.

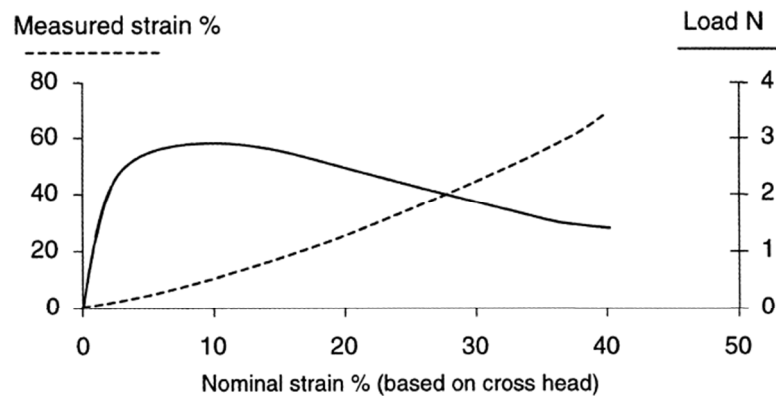


Fig. 2-11 Results of a tensile test of a UD prepreg loaded in matrix direction [43]

The explanations given above are restricted to loading in either fiber or matrix direction. If woven fabrics or NCFs are loaded in off-axis direction (neither in fiber nor in matrix direction) mainly a shear deformation occurs rather than a tensile deformation. This effect can be seen when performing a bias extension test (cf. 4.1.1). In contrast, Potter [43] performed different off-axis tension tests on UD prepreps and proved that even if shear occurred the matrix strain was still the dominating deformation for UD prepreps. Based on his results one can affirm that transverse strain is a more dominant effect in UD prepreg forming than shear. This assumption is confirmed by the test results presented in chapter 1.

The transverse behavior of AFP materials is twofold. A single tow has the same tensile behavior as a UD prepreg. Multiple tows laid-up in an UD ply show lower mechanical properties in transverse direction than a single tow. By placing single tows next to each other adjacent tows partly melt together. But this bond is much weaker than the bond within a tow. Hence, by applying a transverse load on AFP materials they tend to tear off at the tow boundaries (Fig. 2-12). The bearable force and tensile stiffness, respectively, are much smaller as for UD prepreps.

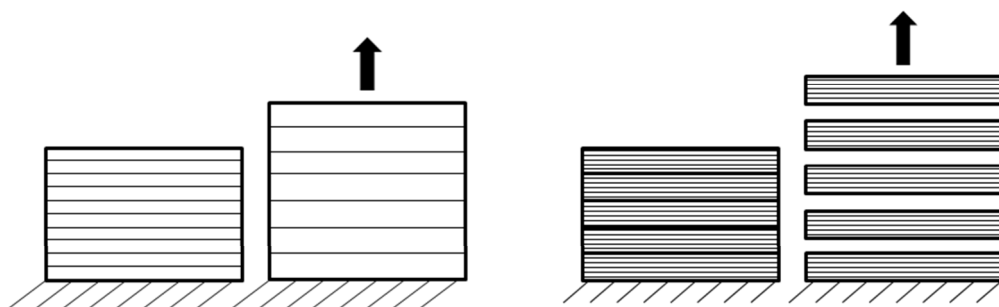


Fig. 2-12 Transverse tension of UD prepreg (left) and AFP material layup (right)

The in-plane compression of textiles during draping is of minor importance. The stiffness of filaments, yarns and matrix in compressive direction is alike their tensile stiffness. However, no high compressive stresses and forces can be heard since the material rather starts to buckle instead of carrying the load (Fig. 2-13). The textiles are very

thin compared to their areal spread which provides only low geometrical stability for in-plane compressive loads. The buckling has multiple reasons: fiber misalignment, off-axis loading or imperfections in the material. While NCF and UD materials might carry a small load, woven fabrics will immediately start to buckle due the undulated yarns.

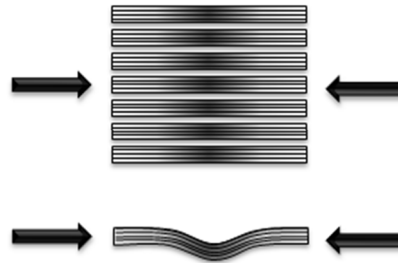


Fig. 2-13 Buckling in compressive loading of UD textiles [19]

2.1.4 Inter-ply movement / frictional behavior

The aforementioned deformation modes can be defined as intra-ply mechanisms, meaning they occur within a single ply. To increase the productivity in composite part manufacturing usually stacks of plies are draped at once instead of draping each ply individually. By draping a ply stack the plies move relative to each other and influence each other (Fig. 2-14). The interaction is mainly driven by the friction between the plies which enables a transfer of loads from ply to ply [18]. Also the friction between the plies and the tooling can have a great impact on the draping behavior. Especially in processes with flexible tooling like membranes or bladders the tool-ply interaction can be the governing effect on the draping result [44].



Fig. 2-14 Rotational and translational motion between plies [19]

The simplest theory to describe the friction is based on the Coulomb friction. The friction coefficient μ is defined as the ratio of the friction force F_{fric} and the normal force N .

$$\mu = \frac{F_{fric}}{N} \quad (2-10)$$

It is a linear assumption and is not influenced by any other environmental condition. The assumption of Coulomb friction is fairly good for ply-ply friction of dry textiles.

Also ply-tool friction shows a Coulomb friction behavior if the tooling is rigid and the plies without any resin. When it comes to describe the frictional behavior for pre-impregnated textiles the friction coefficient is also dependent on temperature T , matrix viscosity η , pulling velocity v and normal pressure. Different authors [45–49] assume a hydrodynamic friction described via the Stribeck curve which relates the friction coefficient to the Hersey number H_e (Fig. 2-15):

$$H_e = \frac{\mu(T)v}{N} \quad (2-11)$$

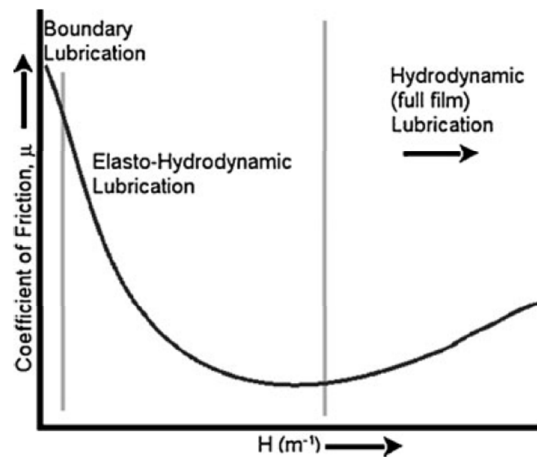


Fig. 2-15 Stribeck curve [45]

The hydrodynamic friction is primarily assumed for thermoplastic materials at forming temperatures [46]. The matrix acts as a lubricant layer between the plies and separates the plies from each other. With a small normal pressure the plies can still easily slide to each other. If a higher normal pressure is applied the matrix layer might be pushed away such that the fibers come in contact to each other. In this state the hydrodynamic friction is not valid anymore.

If the fibers of the plies come in contact to each other, like for dry textiles, the fiber orientation is another influencing factor. For example for dry textiles the friction coefficient of a $0^\circ/0^\circ$ combination is smaller than a $90^\circ/90^\circ$ combination. In the $0^\circ/0^\circ$ setup the fibers can easily slide in longitudinal direction on top of each other. Whilst in the $90^\circ/90^\circ$ combination the fibers are sliding transversely to each other leading to a catching of the fibers. For woven fabrics Gorczyca [50] showed no influence of the fiber direction. But still, Hivet [51] proofed the frictional behavior to be sensitive to the positioning of the plies to each other.

The friction between plies and tooling shows a dependency on temperature, pressure and velocity. According to Gorczyca [50] the tool temperature is one of the most influencing parameter in thermoplastic stamping processes.

The frictional behavior of AFP materials is alike other impregnated textiles. However, its tow-based structure might be destroyed if too high frictional forces are acting perpendicular to the fiber direction.

2.1.5 Out-of-plane compression / compaction

A less considered deformation mode is the out-of-plane compression and compaction of textiles during draping. Depending on the forming process high compressive forces could occur. Even if the compaction of the textile is only influencing the draping result slightly it still has a strong influence on subsequent process steps like infiltration and curing as well as the mechanical performance of the final part.

By applying a load in normal direction on the textile its thickness reduces due to moving and rearrange yarns and subsequent compaction of single yarns [52]. In ply stacks additionally nesting effects are taking place during compaction. Fig. 2-16 indicates the thickness reduction coming along with an increase of the fiber volume fraction. In addition, the voids in prepregs are reduced during compaction [18].



Fig. 2-16 Compression of textile composites [19]

As Fig. 2-17 depicts the initial out-of-plane stiffness of dry NCFs is quite low and small forces compress the textile to 70...80% of their initial thickness. With a further increase of the force the textiles compress to 60...70% of the initial thickness [25]. It should be noted that the initial thickness and the compaction behavior is different for the textiles in a sheared state. Further, a relaxation of compressive stresses takes place when a textile is compressed and held at a certain thickness [53, 54].

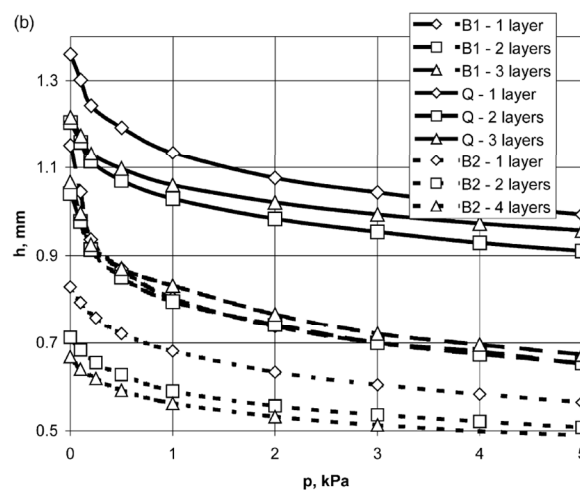


Fig. 2-17 Compression diagrams for biaxial and quadriaxial NCFs [40]

In prepreg materials additionally viscosity effects govern the compaction behavior [18]. Besides the compaction of the textile structure the matrix is compressed and starts to flow within the ply.

The compaction behavior of UD prepreps is quite limited since the manufacturer pre-consolidates the plies in production [18]. Nevertheless for thick ply stacks the thickness change sums up to a degree of compression which cannot be disregarded [54, 55].

For AFP materials the same behavior as UD prepreps can be investigated. Only the initial thickness and initial compaction state might be different since the roller of the placement head further consolidates the AFP material during layup.

2.2 Defects

In textile forming different kinds of defects can occur which need to be avoided. Defects arise when a textile is deformed above its deformation limits. The point when defects arise and the kind of defect are dependent on different factors:

- Material type (fiber architecture, dry, impregnated, etc.)
- Process conditions (temperatures, forces, friction, velocities, etc.)
- Deformability of the textile (cf.2.1)
- Ply placement and alignment
- Matrix rheology
- Layup

The main defects which need to be avoided are the formation of wrinkles and subsequent folds. They start to appear when the in-plane load cannot be carried anymore and small imperfections in the material induce a non-uniform stress distribution such that the material starts to deform out-of-plane (Fig. 2-13). The in-plane load can be either

caused by compressive stresses in fiber direction or at large shear strains when fibers start to jam [28].

Besides wrinkles and folds also other defects emerge in textile forming. They either emerge individually or in combination with other defects. Typical defects are:

- Gaps/voids (lead to porosities or matrix accumulation)
- Yarn/fiber fractures/breakage
- Matrix tearing/rupture (UD prepregs)
- Tow separation (AFP materials)
- Loops/yarn buckles
- In-plane wrinkling/bending (lead to fiber waviness)
- Fiber/yarn/ply pull-out or slippage
- Fiber/yarn/ply misalignment
- Local thinning
- Fuzz balls (mainly for dry textiles)
- Breakage of stitching (NCFs)
- Delamination (in laminate forming)

Fig. 2-18 through Fig. 2-21 show selected defects using the example of UD prepregs and NCFs.



Fig. 2-18 **Wrinkle/folds**

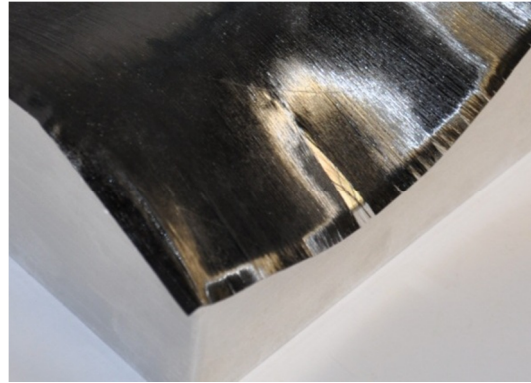


Fig. 2-19 **Matrix rupture**

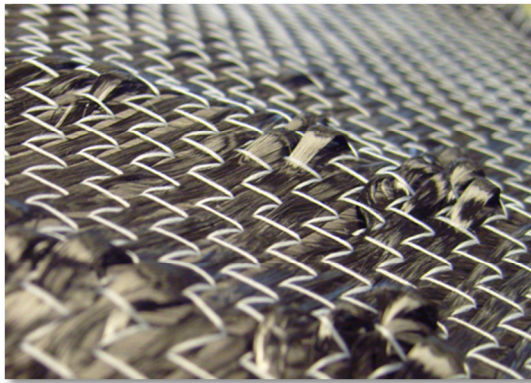


Fig. 2-20 **Loops**



Fig. 2-21 **In-plane bending**

The typical defects in AFP material forming are almost the same as for UD prepregs. Since the material has a poor ability to shear the formation of wrinkles is most likely during forming. As mentioned in 2.1.3 the AFP material mainly undergoes a tensile strain in matrix direction. Consequently either tow separation or gaps within a tow are common defects.

A quantitative definition of all mentioned defects cannot be given here. The definitions of defects are rather a question of tolerance. Depending on the requirements of the final part or the forming process one has to define to what extend a defect is acceptable or not. For example minor gaps might be tolerated in AFP layups if they do not influence the mechanical properties of the final part. On the other hand a loop (out-of-plane bending) in a single AFP tow might influence adjacent plies, develop through the whole laminate and form a major fold in the whole laminate.

The following chapters will again address different defects in terms of modeling within the simulation and forming experiments. They will be discussed and evaluated by their impact on the simulation and experimental results.

3 Draping Simulation

Forming a composite textile has a manifold deformation behavior which cannot be predicted easily for complex structures and materials. Applying trial & error methods to predict the final forming result is often expensive and time-consuming. An alternative approach is to apply numerical methods to simulate the forming process.

In general, the draping simulation can be used in three fields of composite manufacturing: In the part design, in the process development and optimization as well as for simulation of the whole composite process chain.

Using the draping simulation in the part design allows predictions of different draping aspects in an early stage of the part development. Main purpose is to perform a feasibility study to investigate if draping in the desired shape is possible or not. It also allows to predefine the cut geometry of each ply and if darts need to be inserted. Besides, the predicted final fiber alignment can be used for performing structural analysis with accurate laminate properties.

In production the draping simulation can help developing new forming processes or optimizing existing processes. For example if a certain composite part had been designed one needs to find the most suitable process to manufacture the part. Depending on the part geometry, the material to be used and the number of parts often only one type of process fits best for manufacturing. In contrast, if a forming process is already in operation the draping simulation can help to optimize its process parameters like for example forming velocities, forces and temperatures.

Last purpose is to use the draping simulation as a part of the simulation of the whole composite process chain. The objective is to simulate every single manufacturing step (e.g. preforming, resin infiltration, curing, etc.) to account for all process-steered parameters in the final part. Here, the draping simulation acts as one of the first process steps and provides input for subsequent simulations like fiber alignment, thickness distribution, defects, or the preform shape.

In this work the main purpose of applying the draping simulation is to support the development of a new forming process for an already existing composite part. Up to now the part was manufactured by hand layup of thermoset prepreg plies. In the new forming process an AFP machine places the prepreg flatly on a mandrel and builds up the predefined laminate layup. In a subsequent step an inflating bladder forms the laminate into the final shape. The draping simulation will be used to investigate the influences of different material and process parameters and to understand the inner mechanisms taking place during forming.

3.1 Requirements for a draping simulation

For simulating the draping of textiles composites one needs to model the forming mechanisms of composite textiles (Chapter 1) with a suitable material model. As already shown, the textiles undergo high degrees of deformation and show a non-linear behavior for most of the deformation modes. Common material models cannot account for such a material behavior. Regarding for example the plane stress state for homogeneous materials it can be described by Hooke's law:

$$\begin{bmatrix} \sigma_{11} \\ \sigma_{22} \\ \sigma_{12} \end{bmatrix} = \frac{E}{1-\nu^2} \begin{bmatrix} 1 & \nu & 0 \\ \nu & 1 & 0 \\ 0 & 0 & 2(1+\nu) \end{bmatrix} \begin{bmatrix} \varepsilon_{11} \\ \varepsilon_{22} \\ 2\varepsilon_{12} \end{bmatrix} \quad (3-1)$$

It describes the stresses σ_{ij} by means of the Young's modulus E , the Poisson's ratio ν and the strains ε_{ij} . Consequently, the material behavior depends only on the two material parameters E and ν .

The constitutive law of a textile cannot be described with Hooke's law. A generalized form might be written as:

$$\begin{bmatrix} \sigma_{11} \\ \sigma_{22} \\ \sigma_{12} \end{bmatrix} = \begin{bmatrix} E_1 & ? & ? \\ ? & E_2 & ? \\ ? & ? & G_{12} \end{bmatrix} \begin{bmatrix} \varepsilon_{11} \\ \varepsilon_{22} \\ 2\varepsilon_{12} \end{bmatrix} \quad (3-2)$$

Here, the three material parameters E_1 , E_2 and G_{12} plus appropriate Poisson's ratios are needed. The off-axis terms in the stiffness matrix are marked with "?". Depending on the kind of textile these off-axis terms should not always be the same. As mentioned in Chapter 1 the tensile properties in E_1 direction might be dependent on the properties and stress state of E_2 . Also the shear properties $G_{1,2}$ might be influenced by the tensile properties. Some textiles show a totally uncoupled behavior, meaning no interaction of E_1 , E_2 and G_{12} .

Also the high anisotropy is difficult to capture with a common material model. For example AFP materials have a Young's modulus in E_1 direction which is orders of magnitude higher than in perpendicular direction (E_2). This large stiffness ratio leads to numerical instabilities when using ordinary material models.

Further requirement for the material model is the consideration of viscous effects if preimpregnated textiles have to be simulated. The model should allow including a rate- and temperature-dependent material law with non-linear behavior.

Besides the material model the simulation should also allow taking into account influences of the forming process. This means that all relevant tooling parts like e.g. cavities, forerunners, blankholders, etc. can be modeled and which can affect the forming result. Not only the mechanical influence needs to be considered, but also their thermal interaction with the laminate. A heated laminate cools down rapidly if it comes into

contact with the colder tooling. This changes the forming behavior of the laminate locally and can affect the total forming results as well.

Furthermore, the friction during forming needs to be taken into account. Friction occurs between single plies slipping relative to each other and between plies and the tooling. Both frictions require a proper friction model in the simulation. Friction of dry composite textiles might be modeled with simple linear friction models. But preimpregnated textiles might require non-linear and viscous friction models.

The more of these requirements can be captured by the material model and the simulation, the better and more accurate the results get. Not just the draping behavior can then be modeled but also the formation of defects might be simulated. In the following different material models will be introduced which capture more or less the characteristic draping behavior of textiles.

3.2 Numerical approaches

Nowadays a variety of numerical approaches and material models exist which can be used for simulating the draping process. Oftentimes these approaches and models are related to a specific textile type and do not suit well for others. Certain review articles give a good overview on existing numerical approaches [15, 56–58].

The different approaches can be divided in two numerical methods: the kinematic approach and the Finite Element (FE) based approach. The following chapter presents the two methods and the related material models.

3.2.1 Kinematic approach

In 1956, Mack and Taylor [59] first announced the kinematic approach to describe the fitting of woven cloths to surfaces. In literature this approach is also named geometric approach or fishnet algorithm [13, 60, 61]. One can consider this approach as a net or mesh of initially quadratic elements draped over a surface and only undergoing shear deformations leading to deformation of the elements into rhombus shapes. In general, the algorithm is based on the following assumptions:

- Only shear deformation (free rotation of the yarns at their crossings)
- Inextensible fibers
- No bending deformation
- No sliding of single yarns or whole plies
- No thickness

Fig. 3-1 shows the principle of the kinematic draping approach and Fig. 3-2 describes the underlying algorithm. First a starting or seed point P is defined on the surface. Then two directions are defined on which geodesic lines L_1 & L_2 are drawn on the surface. By defining a mesh size or a step length, respectively, the two points $i, j-1$ and $i-$

l,j can be found. The point i,j is then the intersection of two geodesic lines starting at $i,j-1$ and $i-1,j$ with the predefined step length. It can be easily computed by using sphere formulae at the starting points which intersect with the surface at the new point i,j . Afterwards the algorithm continues to find the next points.

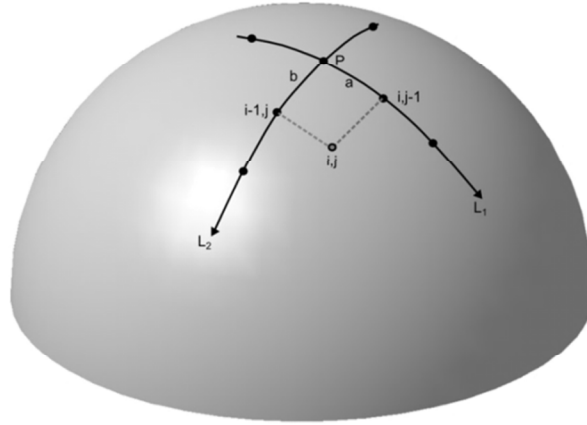


Fig. 3-1 Principle of a kinematic draping simulation [19]

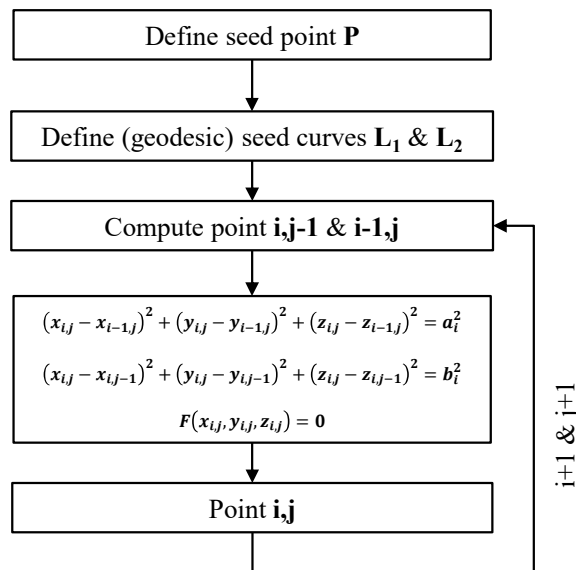


Fig. 3-2 Algorithm of a kinematic draping simulation [19]

The algorithm already indicates that no material properties are taken into account. Meaning, the approach cannot differ for example between draping a woven fabric and draping a UD ply. Also no influence of the draping process parameters is taken into account. The kinematic approach will provide always the same result no matter which material or draping process is simulated.

Some researches modified the algorithm to account for different material characteristics and processes. Van der Weeën [61] introduced an approach with extensible fibers in which the elastic energy of the fibers is minimized during mapping. Long [62] de-

scribed an approach which minimizes the strain energy being able to represent the asymmetrical behavior of NCFs.

The kinematic draping simulation is nowadays widely spread and available in different commercial codes such as Catia CPD, FiberSim or PAM-QuikForm. Some codes offer to define different propagation modes which change the sequence and direction of the mesh calculation, enabling to account for different draping steps.

Main output of a kinematic draping simulation is the fiber alignment and shear angle. Those are mostly presented in contour plots as pictured in Fig. 3-3. With the knowledge of the maximum shear angle (cf. 2.1.1) of a specific textile the simulation might indicate regions where folds can occur. Another output of the kinematic draping simulation is the generation of the flat pattern geometry (Fig. 3-3).

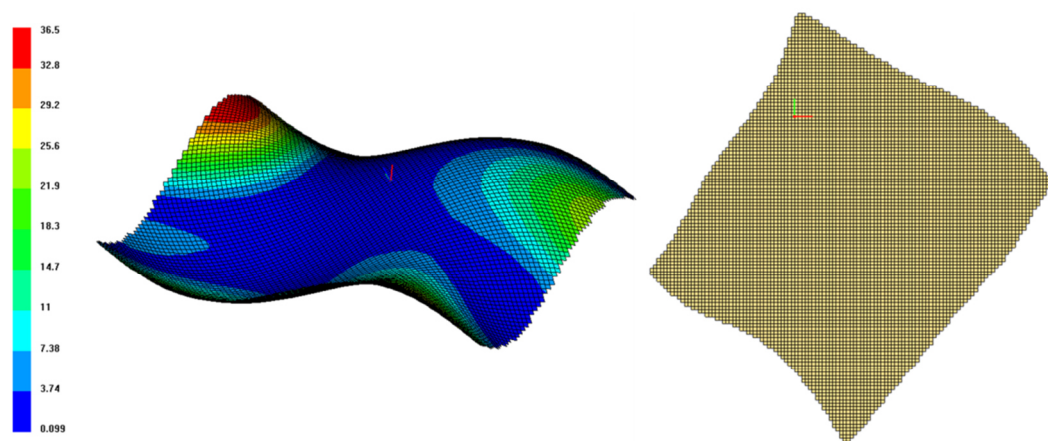


Fig. 3-3 Kinematic draping simulation on Double Sine geometry using PAM-QuikForm
Shear angle plot (left); flat pattern (right)

The main advantages of the kinematic draping approach are its easy usage, the fast computation and that only few inputs are required. It provides fairly good results for hand draping in classical prepreg fabrics on smooth curved surfaces [13]. It is available in many commercial codes and has a good interface to subsequent simulations like e.g. infiltration simulations, curing simulations and structural analysis.

Disadvantages of the approach are the poor quality for complex shapes and textile materials with a strong non-linear behavior. Since no material properties and process influences are taken into account the simulation only provides an estimation of the final draping result. Especially by investigating highly deformed areas the simulation overestimates the shear angles [63]. Further, it does not show whether defects will occur or not.

3.2.2 Finite Element approach

To account for all physics taking place during draping all equations of the textile mechanics need to be considered. Especially load equilibriums, constitutive equations and boundary conditions (BCs) like contacts and friction need to be included [13, 64]. The FEM allows including all these equations and also an implementation of a suitable material model for textile draping. But standard FE formulations are often only valid for small and moderate strains. In textile draping high deformation grades occur which cannot be modeled with standard material models. Large deformation FE simulations of highly anisotropic material often lead to slow convergence or break down with increasing anisotropy and deformation [65]. Hence, specialized material models are required for simulating the complex behavior of composite textiles.

In the following different FE approaches for modeling the draping of textiles are presented. In general they can be subdivided in three groups according to their modeling detail level: macroscopic level, mesoscopic level and microscopic level (Fig. 3-4).

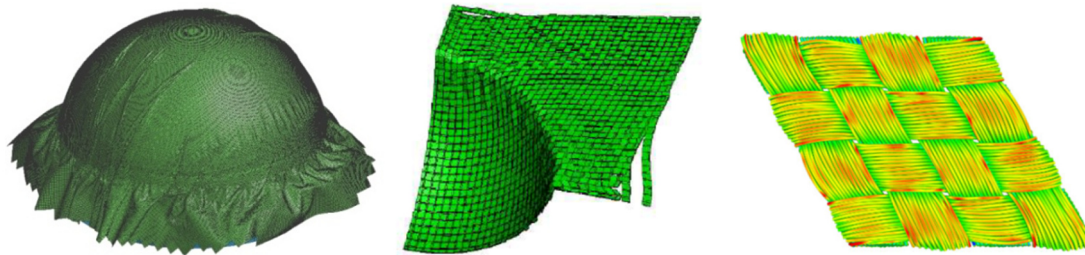


Fig. 3-4 FE draping simulation on different levels
Macroscopic level (left), mesoscopic level (center) and microscopic level (right) [17, 66]

Macroscopic FE approach

The macroscopic FE approach, also called continuous approach, models the textile on ply level. Meaning each ply is modeled separately by a single layer of shell elements. The elements assumed to be continuums by neglecting the fibrous structure of the textile. Hence, only macroscopic deformations like intra-ply shear, ply bending and ply tension/compression are considered. Yarn slippage and inter-yarn movements cannot be accounted for. Since each single ply is modeled inter-ply movements and interactions are also considered.

To assure a proper forming behavior a suitable material model needs to be used. As mentioned in chapter 3.1, an anisotropic material model with non-linear behavior is required. The in-plane properties (E_1 , E_2 and $G_{1,2}$.) need to be independent from each other. Further, it is important to decouple the in-plane properties from the bending behavior [33].

The bending stiffness is important to simulate the formation of wrinkles [28, 29]. Therefore shell elements should be preferred. Membrane elements might also be used but they do not offer any out-of-plane properties.

In literature different material models for the macro scale are presented. Boisse et al. [13] introduced two models based on different formulations. One model based on a hyperelastic formulation where the constitutive model is derived from the potential energy [67]. The other model based on a hypoelastic formulation where a Cauchy stress objective derivative is related to the strain rate by a constitutive tensor [68]. The latter formulation provides an exact solution at large strain.

Dong et al. [69] presented a material law with updating fiber directions. During shearing the fiber directions do not coincide with the local material coordinate systems in a non-updating material law. This results in shear/tension locking effects, meaning fictitious tensile stresses in fiber direction in pure shear loading. Dong's material law prevents those effects by updating the fiber direction during the simulation.

Other authors introduced material models which take into account the viscous behavior of preimpregnated textiles. Harrison [56] modeled a 2x2 twill weave glass/propylene thermoplastic and a 5-harness satin weave carbon/epoxy prepreg accounting for viscosity by energy dissipation. Yu et al. [9] presented non-orthogonal rate independent model which only takes the matrix stiffness into account. Ten Thije [65] proposed a model based on an updated Lagrangian FEM. It shows quadratic convergence for arbitrary degrees of anisotropy and high linear and plastic deformations.

Ten Thije and Akkerman et al. [65, 70, 70, 71] implemented their material model in the own-made FE code AniForm. Boisse, Hamila, Vidal-Sallé et al. [28, 64, 67, 72–74] programmed the FE code PlasFib to implement their material model. Other authors implemented their material models as subroutines in commercially available FE codes like Abaqus [75–78] or LS-Dyna [79]. The advantage is to benefit of already existing element, contact and friction formulations.

Some commercial FE codes offer own material models for performing a draping simulations. The explicit FE solver PAM-FORM (ESI Group) provides a material model with a thermo-visco-elastic matrix and elastic fibers for shell elements [80, 81]. The material model offers a decoupled bending definition and accounts for viscous behavior by use of a Maxwell element. Abaqus offers a material model (*FABRIC) which is commonly used for airbag simulations but can be also used for draping simulations. With *VFABRIC Abaqus offers additionally a subroutine which allows the user to implement own material models for draping.

In comparison to the kinematic draping approach the macroscopic FE approach requires more input data and a higher computational effort. To set up a simulation the whole forming process need to be modeled. This includes the tooling and BCs like forces, velocities and contacts. The kinetic is introduced via the constitutive laws of the material model and the friction definition.

The output quality of the macroscopic FE approach is consequently higher than in the kinematic approach. Besides the shear angle and the fiber alignment the FE approach provides strains, stresses, macroscopic draping defects and the whole draping se-

quence. One has to be careful with the provided stress output since it refers to the element as a continuum and not to its fibrous structure [64].

Mesoscopic FE approach

The mesoscopic FE approach, also called discrete approach, models the textile at yarn level. Each yarn, roving or tow is modeled individually by beam, shell or solid FE elements. Contact definitions and associated friction definitions control the yarn interactions. Besides the macroscopic deformation mechanisms and the draping defects this approach accounts also for inter-yarn movements and defects like gap opening or loops.

In literature different modeling techniques are presented. Pickett and Creech [82, 83] modeled a NCF using solid elements for the tows and bar elements for the stitching. Boubaker [84] model the yarns with spring elements to investigate the behavior of a woven fabric with a mass-spring system. Badel [13, 68] compared two approaches to model a woven fabric: a model with solid elements (47214 DOF) and a model with shell elements (216 DOF) for the yarns. Vidal-Sallé [85] used a model based on solid elements to investigate the out-of-plane compression of woven fabrics. Hamila and Boisse [64, 86] presented a semi-discrete approach combining the macroscopic and mesoscopic approach. They used shell elements which consisted of a discrete number of textile cells based on a mesoscopic model. The strain energy in the interpolated displacement field presents the nodal loads of the element.

The mesoscopic FE approach requires other input parameters as the macroscopic approach. At first, the setup of the model requires the knowledge of the geometry of the textile structure. Further, the material model of the yarns requires the tensile and compression properties in fiber and perpendicular direction. At last, the model requires a proper friction model for the interactions of the yarns.

Besides the output of a macroscopic FE simulation, the output of the mesoscopic approach provides information about deformation of the inner structure. Depending on the used elements the yarn compaction, inter-yarn movement and gap opening are provided.

Microscopic FE approach

The microscopic FE approach is the most detailed method to investigate the forming behavior of textiles. It aims for modeling the filaments and their interaction to each other. The modeling of each single filament would computational be too expensive. Therefore, researchers tend to simplify the simulation by modeling only few filaments in a single yarn. Anyhow, this approach can be only effectively applied to small models like unit cells.

Duhovic [16] used this modeling approach to simulate the knitting process. Durville [17] modeled a woven fabric to investigate the behavior within the yarns. Both researchers used beam elements and an appropriate friction contact for their models.

Even if standard beam elements are used in the microscopic approach it is still difficult to gain the material parameters of a single filament. Especially the friction coefficient of the filaments is hard to characterize.

3.3 Selected simulation approach

For the draping simulations in this work a suitable simulation approach had to be chosen. The choice based on the requirements defined in the underlying research project and the infrastructure at the LCC:

- Support of new forming process development
- Application on part size level
- Modeling of thick, multi-layered AFP material layups
- Investigation of different process parameters and their influence on the draping result
- Commercially available software package (with customer support)
- Material characterization restricted to the testing equipment at the LCC

The explicit FE solver PAM-FORM from ESI Group matched the requirements best and was therefore chosen as simulation tool in this work.

A kinematic simulation would have been too imprecise because it does not consider material characteristics and process parameters [63]. To account for those aspects it requires a FE based simulation approach. The FE approach additionally allows the prediction of possible draping defects.

The choice for a macroscopic simulation mainly based on the requirement to model the forming on part level. A simulation on mesoscopic level would require a too high computational effort.

3.4 Description of PAM-FORM

PAM-FORM is an explicit solver used for draping simulations of composite textiles. Inherited from the PAM-STAMP solver, which is used for sheet metal forming simulations, the material model MAT 140 was additionally implemented.

The PAM-FORM solver comes with the pre- and postprocessor PAM-FORM 2G. However, in this work Visual-Environment 8.5 (ESI Group) was used as pre- and postprocessor since it offers more possibilities in defining BCs. As an example, the definition of an orthotropic friction is not possible in PAM-FORM 2G.

MAT140 is a composite bi-phase shell element consisting of three components (Fig. 3-5).

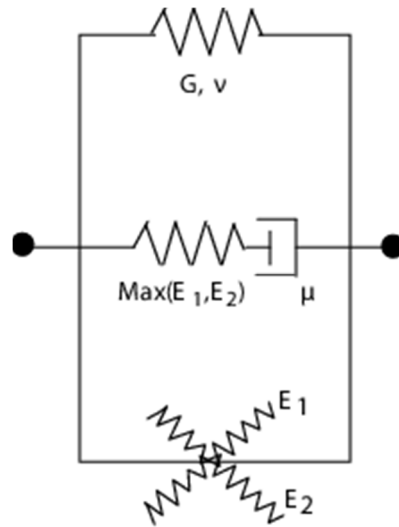


Fig. 3-5 Components of material MAT140

Stabilizing parent sheet (top); thermo-visco-elastic matrix phase (middle); elastic fiber phase (bottom) [80]

The parent sheet controls the shear behavior of the material to overcome the strong numerical instabilities due to the high anisotropic behavior. It is a superimposed visco-elastic shell element based on the shear modulus G and the Poisson's ratio ν . The shear modulus can be either defined via a curve with respect to the shear angle or via a bilinear definition. For the latter an initial shear modulus G and a “shear modulus after locking” G_{lock} , which starts after a defined locking shear angle α_{lock} , has to be defined [80].

To account for the viscous influence of the matrix a Maxwell component is included. For the viscosity definition there are four possibilities: no viscosity, constant viscosity, power law and cross equation.

The third component defines the material properties along the fiber directions. The angle α defines the orthotropy from the fiber direction. The Young's moduli $E_{1,2}$ can be defined either as a constant value or a non-linear curve. The bending behavior is defined by a bending factor F_b or a constant bending value and the out-of plane shear factor F_s [80].

It is recommended to align the FE mesh along the fiber direction to ensure the fibers being parallel to the element edges. If not, numerical locking effects can occur which lead to a stiffening during shear deformations [73, 87–89].

In the present work the solver version 2012 was used. This version offers the possibility to decouple the fiber components from the parent sheet. In earlier versions the parent sheet induced parasitic tensile and bending stiffness which need to be opposed by

adjusting the parameters. For woven fabrics these tensile stresses are negligible small, but for UD materials they have a significant impact on the result.

MAT140 offers two material laws for composites: fabric (RFLAG=1) and unidirectional (RFLAG=0). This option controls the shear mechanism and the update of the fiber direction during deformation (Fig. 3-6). The fabric definition implies pure shear and alter the angle between fiber direction 1 and fiber direction 2. The unidirectional definition implies a simple shear and fiber direction 2 (matrix direction) stays perpendicular to fiber direction 1 during the whole simulation.

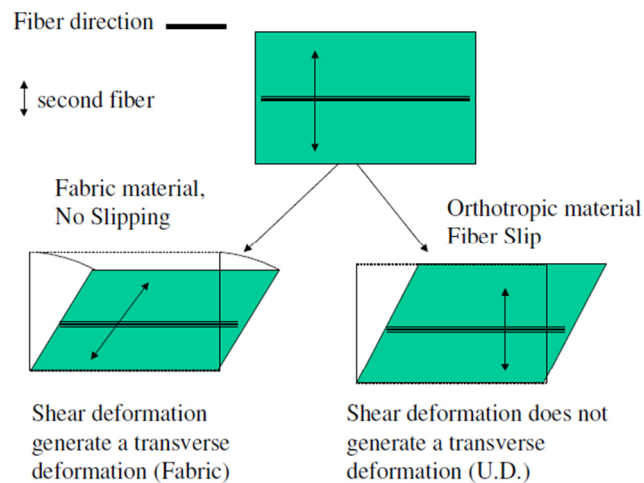


Fig. 3-6 Shear modes in MAT140 [80]

MAT140 should be used with linear 4-node shell elements. Higher order shell elements like quadratic 8-node elements are not compatible with MAT140. The only possibility to increase the quality of the shell element is to define the integration method. The Belytschko-Tsay formulation as a uniform underintegration with one integration point is standard. The Hughes-Tezduyr formulation offers a full integration with four integration points in order to avoid hourglassing effects. Third possibility is the Belytschko-Wong-Chiang formulation as a uniform underintegration with anti-warping term to avoid zero energy modes. The solver offers further integration methods but those are not compatible with MAT140. In this work the Belytschko-Tsay uniform underintegration formulation is used since it is the numerical cheapest and most stable. Studies have been made with the other formulations and showed no significant differences in the results.

A further important parameter is the definition of the shell thickness that influences the shear, tensile and bending behavior. Even though simple shell elements are used, PAM-FORM offers to show thickness changes during forming. It is a post-processing option which shows calculates the thickness change according to the degree of shear based on the theory of volume conservation. It is also possible to have a user-defined function for the thickness change.

The viscous option (Maxwell element) in MAT140 is used to account for the time- and velocity-dependent behavior of impregnated composite textile. Although this work investigates AFP materials the viscous option was not used. The forming process, to which this work aims to simulate, is manually controlled, which might lead to different forming velocities from test to test. As a consequence, the simulations in this work assumed a constant temperature and velocity throughout all tests and neglects viscous effects.

4 Material characterization

The following chapter introduces material characterization test methods required for draping simulations of composite textiles. According to the aforementioned textile deformation modes and the required material parameters for the simulation model, this chapter presents different possible test methods. Out of these, a set of suitable test methods is chosen to perform a full characterization of the AFP material. The results of each characterization test will be given by the end of each subchapter.

The investigated material is a unidirectional slit-tape from Toray Composites (Tab. 4-1). It is either provided as unidirectional 4-layer laminate manufactured by a Coriolis AFP machine or as a single tow stored on a spool.

Tab. 4-1 Data sheet of the AFP material

Designation	T800/3900-2
Supplier	Toray Composites (America) Inc.
Fiber	T800 (high-strain carbon fibers)
Matrix	3900-2 (high-toughness epoxy matrix)
Form	Unidirectional
Areal weight	195 g/m ²
Tow width (AFP layup)	0.25 inch = 6.35 mm

Up to now no standardized test method is available for non-cured composite textiles. The here given test methods are either own-made test methods generally used in research or test methods deduced from standards which are related to other materials but are able to be employed for composite textiles. Further, only the test methods which characterize the macroscopic deformation behavior will be presented and discussed. Some test methods allow high temperature testing but the majority of those tests are initially intended for testing at room temperature. Solutions to apply these tests likewise at higher temperatures will be also given here.

All tests were carried out at the Composite Testing Lab (CTL) of the LCC. Hence, the choice of the finally used test method was made with respect to the existing equipment of the CTL. Test methods which required a force measurement were done with a 250 kN tensile testing machine from Hegewald&Peschke with an additional 10 kN load cell from Interface. The tensile testing machine is equipped with a thermal chamber to

encapsulate the test fixtures and allow material characterization tests up to 350° C (662° F). For the other test methods, which are performed outside the tensile testing machine, a heat gun was used to heat up the specimens. The test temperature for all tests was 65.5° C (150° F) according to forming processes of the AFP material in the use case.

The characterization tests were performed within three different material setups to find the most suitable specimen type for each test method. As an example, Fig. 4-1 shows these material setups within a PFT. One material setup was the single tow testing. Single AFP tows were taken direct from the roll and used in the test rigs. Another material setup was the single layer setup for which single tows laid up by hand or the AFP machine direct next to each other in order to build up a single ply. The last material setup had been a unidirectional 4-layer ply which was laid up by the AFP machine.

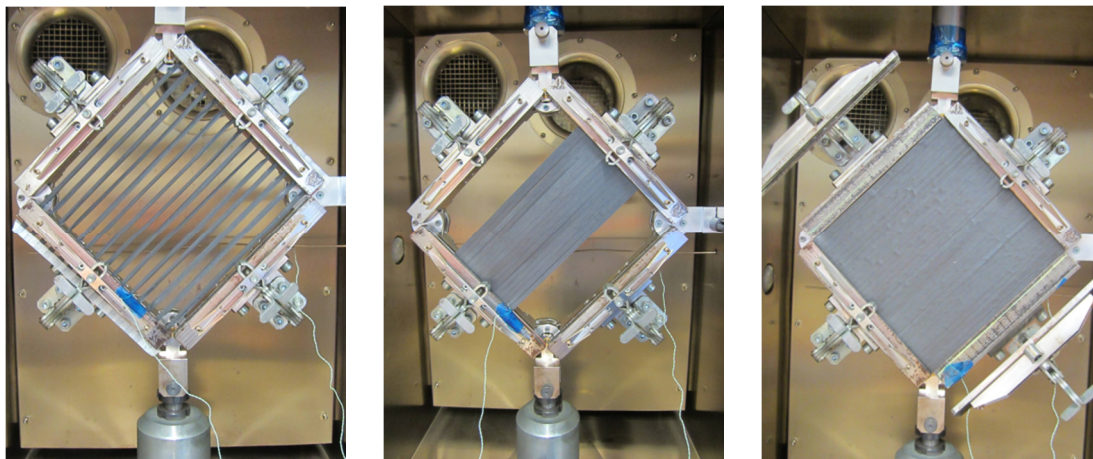


Fig. 4-1 Three different material setups clamped in the PFT
Single tows (left), single layer (center) and 4-layers (right)

The final test results are provided in a form such that it can be used for implementation into the simulation. Depending on the requirements of the material model the results are either given as single values or non-linear curves.

4.1 Shear characterization

As mentioned in 2.1.1, shearing of textiles is seen as the most important deformation mechanism taking place during draping. As a consequence, many researchers focused their work on finding a suitable method for characterizing the shear behavior of textiles. A variety of test methods exist which will be presented here and at the end the most promising method is chosen to characterize the AFP material.

4.1.1 Tests methods

Picture Frame Test

In literature most researchers used the Picture Frame Test (PFT) for characterizing different kind of composite textiles. The PFT clamps the specimen in a quadratic frame with rotating hinges. It is attached in diagonal direction in a tensile testing machine and subsequently deformed in a trellis mode (Fig. 4-2). The specimen undergoes a shear deformation and by the recorded machine force and head displacement the shear force as a function of the shear angle can be derived. The PFT suits best for woven fabrics and biaxial NCF materials. For NCF materials one has to mind the alignment of the stitching since it may influence the shear behavior drastically [18].

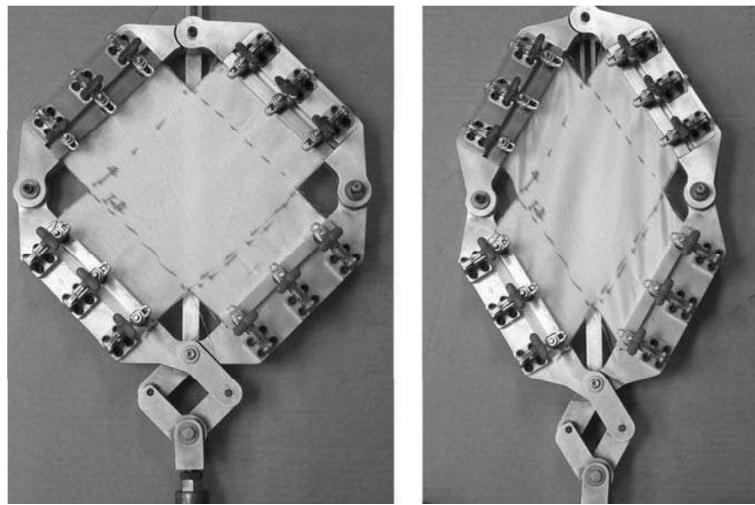


Fig. 4-2 PFT shear states
Initial state (left); sheared state (right) [7]

The arising shear force F_s is dependent on the shear angle θ and can be computed by the recorded machine force F_m using [7, 90]:

$$F_s = \frac{F_m}{2 * \cos(\pi/4 - \theta/2)} \quad (4-1)$$

The shear angle is defined by the displacement of the upper hinge d_{PF} and the frame length l_{PF} of the PFT:

$$\theta = \frac{\pi}{2} - 2 \cos^{-1} \left(\frac{\sqrt{2} * l_{PF} + d_{PF}}{2 * l_{PF}} \right) \quad (4-2)$$

Assuming a constant volume of the specimen the thickness t of the specimen with respect to the shear angle is denoted as:

$$t = \frac{t_0}{\sin(\pi/2 - \theta)} \quad (4-3)$$

Here, t_0 defines the initial thickness of the specimen. The shear stress τ is now defined by the shear force divided by the cross section area with the width b :

$$\tau = \frac{F_s}{b * t} \quad (4-4)$$

Within PAM-FORM the shear modulus G now denotes:

$$G = \frac{\tau}{\tan \theta} \quad (4-5)$$

A PFT provides shear deformations almost homogenously distributed over the whole specimen. Lomov [24, 25] and Birnkammer [91] used the optical measurement system ARAMIS to investigate the shear angle distribution. Both showed that the average shear angle is fairly close (max. $\sim \Delta 2^\circ$) to the angle measured by the head displacement.

The PFT needs to be performed accurately since it is sensitive to misalignment of the fibers. By placing the specimen in the PFT the fibers need to be aligned parallel to the frame hinges (Fig. 4-3). Misalignments lead to tensile stresses in the fibers and affect the measured force [6, 91]. Studies showed that even well controlled PFT experiments can exhibit a scatter of up to 20 % in shear force for the same test setup [7, 8, 23].

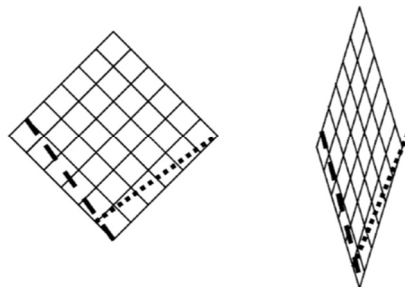


Fig. 4-3 Fiber elongation (dashed line) and compression (dotted line) in the PFT due to fiber misalignment [92]

Another sensitive aspect is the clamping of the specimen. To ensure a pure shear mode the fibers need to rotate freely at the clamping edges. Usually this is not the case because the fibers point out perpendicular of the clamps throughout the whole test. This leads to an S-shape deformation of the fibers which applies strain and therefore tensile stresses in the specimen. Fig. 4-4 shows this effect in an exaggerated manner. If this effect gets too large the shear angle within the specimen is lower than the one derived from the recorded head displacement. To counteract this effect Hübner [93] used pins instead of clamps to attach the specimen. In this case the fibers are able to rotate freely

about the pins and no tension is applied on the specimen. This method works well with dry fabrics since they can be easily pierced on the pins. Attaching thermoplastic sheets would require drilling holes in the specimen for each pin.

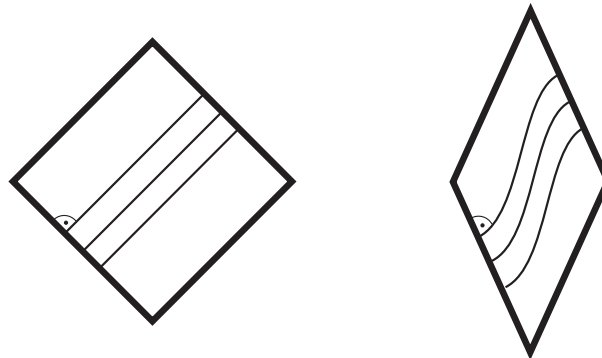


Fig. 4-4 S-shaped fiber course in the PFT
If fibers are not able to rotate freely at the clamping edges [91]

The clamping of thermoplastic sheets can be also problematic. If the clamps do not have the same temperature as the specimen the clamps cool down the specimen in their vicinity. The material will then show a stiffer behavior locally and affect the measured result [90].

As mentioned in 2.1.1, the shear also depends on the tension state of the fibers. Hence, the pretension of the specimen need to be taken into account during testing [22–24]. Launay et al. [22] developed a PFT which allows defining a pretension in the fibers and investigate the different shear characteristics. They showed an increase of the shear force for higher pretensions in the fibers.

For the present work the PFT had been chosen as the test method to perform the shear characterization. The PFT is most flexible with respect to different material types. For this work a new design for the PFT has been developed. Common PFTs require a cross-shaped specimen (see Fig. 4-2) to avoid crashing of the specimen in the corners during testing. The preparation for such specimens is time-consuming because they need to be neatly cut and the cross lying fibers in the cross legs need to be removed [91]. In contrast, the new PFT design avoids time-consuming specimen preparation by allowing clamping a quadratic shaped specimen. The specimen is clamped in such a way that it does not collide with the hinges or the frame at any time during testing (Fig. 4-5).

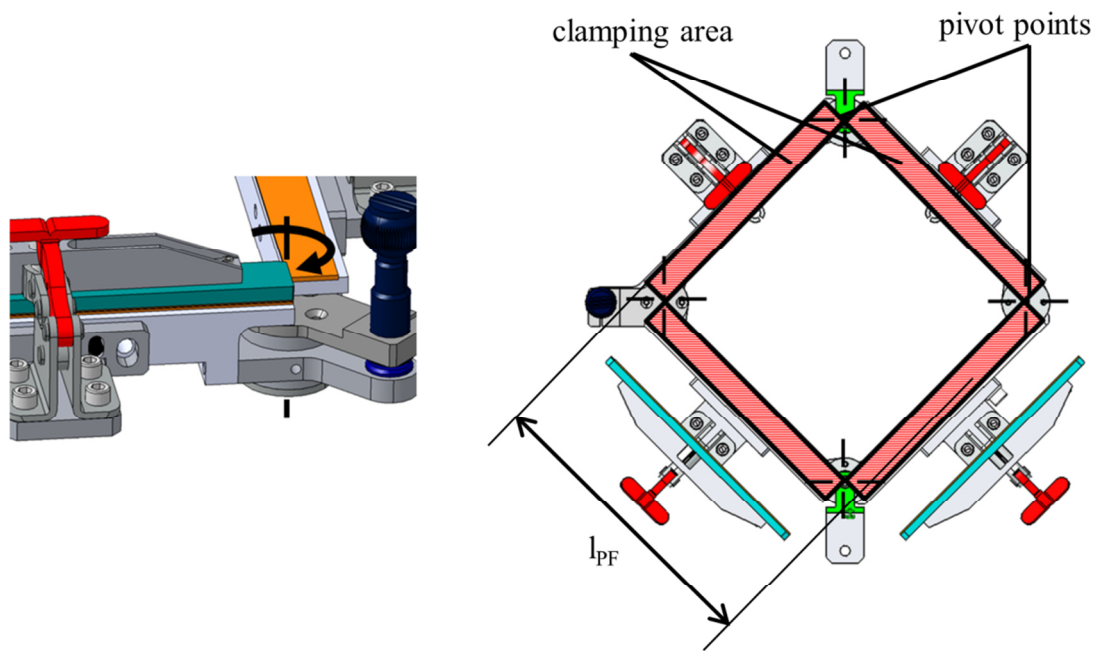


Fig. 4-5 CAD sketch of the new PFT design
Showing the clamping plane above the hinges (left) and the overall clamping area (right)

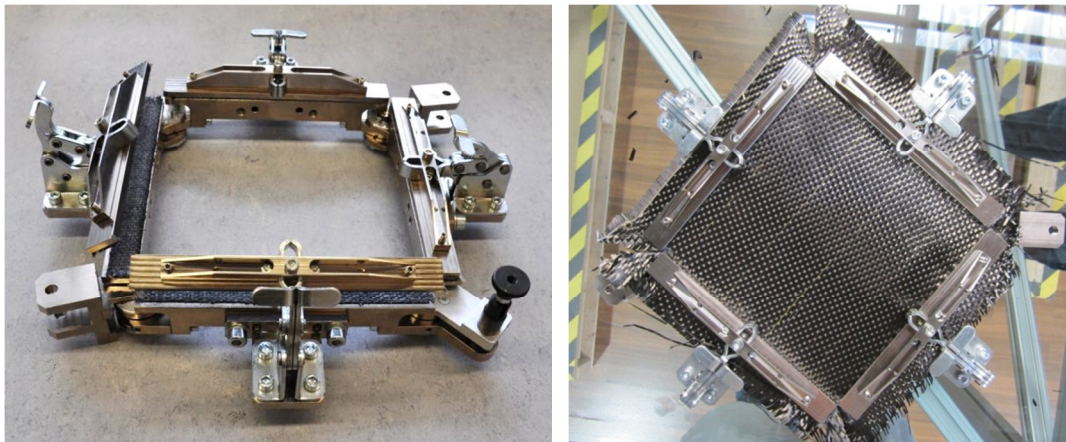


Fig. 4-6 New PFT
Empty (left) and with clamped woven fabric (right)

Fig. 4-6 shows the final PFT design which additionally includes toggle levers for a faster clamping and a cone bolt for fixing the frame in 90°-position. The right picture shows the frame loaded with a woven fabric. The PFT does not need an accurate contour cutting. One only needs to assure a correct alignment of the specimen (fibers parallel to the edges) and four additional cuts at the edges up to the pivot point of the hinges. The tested area then has a quadratic shape with an edge length l_{PF} of 200 mm.

Bias Extension Test

Besides the PFT the Bias Extension Test (BET) is often used for shear characterization. In comparison to the PFT the BET is easier to perform. A tensile testing machine

clamps a rectangular specimen and applies a tensile force. The fibers of the specimen have to be aligned in 45° to the pulling direction and through elongation a shear deformation occurs in the specimen. Fig. 4-7 shows the specimen which is divided in three different shear regions: a fully sheared region (A), a region with half shear (B) and a non-sheared region (C).

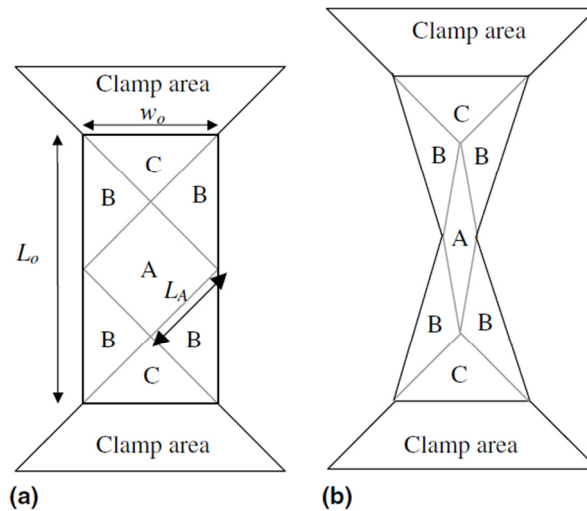


Fig. 4-7 Idealized BET showing 3 different shear regions [90]

Due to the non-homogeneous shear distribution the examination of the recorded machine data is not straightforward. If ideal deformations kinematics are assumed the calculation of the shear angle and shear force can be done with the method described by Harrison [90]. But in reality fiber slippage occurs in the specimen, especially at high forming degrees (Fig. 4-8) [9, 82, 83, 90, 92]. In this case an optical measurement of the shear angles is mandatory [18, 18, 92].

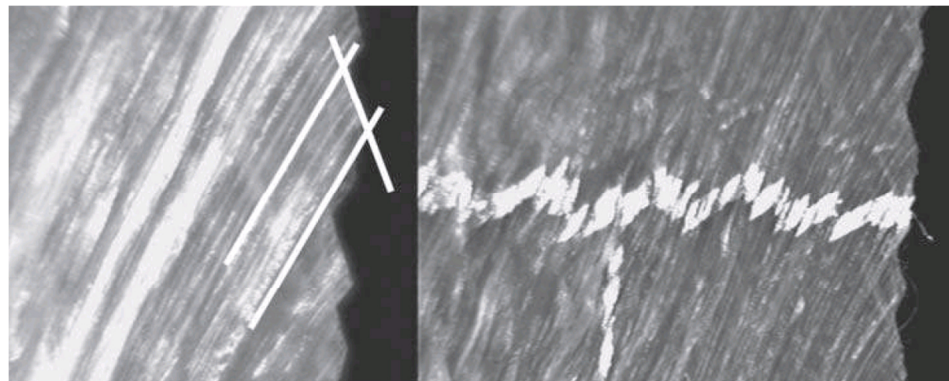


Fig. 4-8 Fiber slippage on the free edge of the specimen in BET [94]

The BET can be only applied to bi-directional textiles. To test UD prepregs, Potter [94] used cross-plyed UD prepreg laminates, which ensured a mutual stabilization of the plies. He showed that wrinkles start to form almost right at the beginning of the test due to misalignment of the fibers. Even though the specimen is subjected to a global tensile stress, the misalignment of the fibers leads to local compressive stresses.

A direct comparison between BET and PFT cannot easily be done because both tests impose different loading conditions [15, 22, 23, 94–96]. In the PFT the all fibers are clamped at both ends and may be pretensed. In the BET some fibers are clamped on one side while some fibers are free on both sides, which cannot bear any tensile loading. Harrison [90] proposed to use the BET only at low shear angles where no fiber slippage occurs and if higher shear angles want to be tested one has to perform PFTs.

KES-FB1

One alternative method for shear characterization is the Kawabata Evaluation System for fabrics (KES-F) [39, 40]. It characterizes different deformation modes of textiles (bending, compression, tensile, etc.) and also consists of a shear characterization test method (KES-FB1). Fig. 4-9 shows the test fixture which is also used for the tensile tests (1). In this fixture the textile is loaded with a dead weight (3) to pretense the fibers which are then fixed by the lower clamp. The opposite clamp then shifts to the side (2) to apply shear on the specimen. This test provides useful results up to 8° shear angle. At higher shear strains it has to be supplemented by the PFT [40].

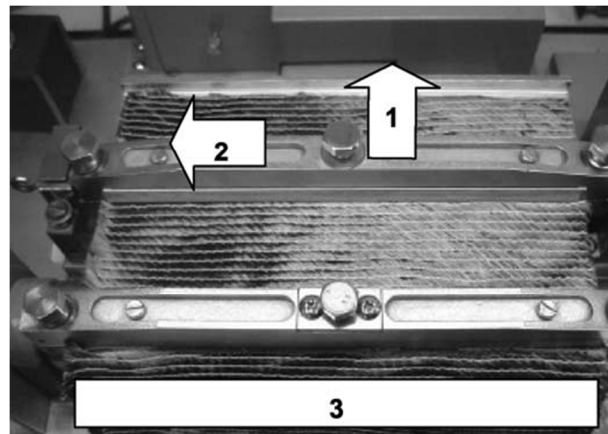


Fig. 4-9 KES-FB1 measurement for tensile and shear deformation [40]

Twisted bar

Shear characterization methods for impregnated textiles are quite limited. Haanappel and Akkerman [12, 26, 97] reviewed different existing test methods which showed a wide range of values for seemingly similar material properties. Instead, they proposed a method of using a rheometer which clamps a rectangular bar of a thermoplastic textile and applies a torsional load in longitudinal direction. This method showed promising results within the linear shear region of the material. Nevertheless, the method need to be further developed to enable also the testing in the non-linear region.

Virtual testing

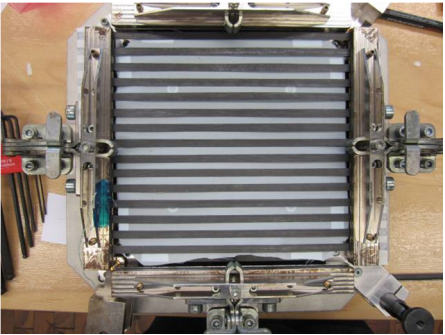
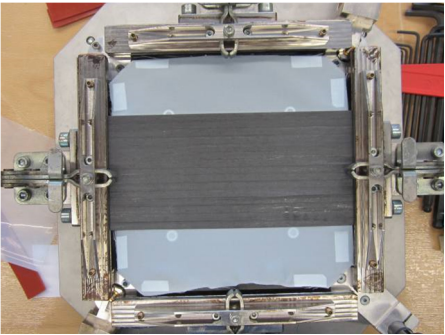
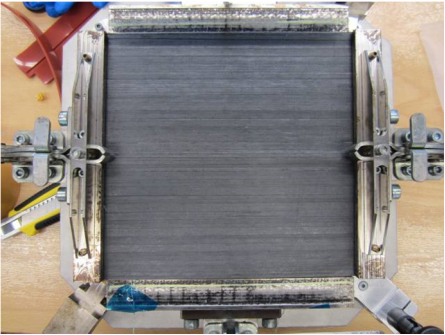
Another possibility is to perform a virtual testing of the material. Badel [98] used a representative unit cell (RUC) and tested it virtually. Drawback of this method is to get

the mechanical properties of the material at meso- or microscopic levels which again need to be tested experimentally.

4.1.2 Test results

In comparison to dry woven textiles the shear characterization of UD prepreg material with the PFT is not straight forward. UD prepregs evolve a stiffer shear behavior which makes it difficult to apply homogenous and defined shear in the specimen. To find the most promising test procedure the three aforementioned material setups of the AFP material had been investigated (Tab. 4-2).

Tab. 4-2 Overview of PFT setups

Test setup	Description	
Single tows	15 single tows clamped in the PFT. One tow width distance between tows to avoid tow interactions.	
Single layer	15 tows ($\cong 95.25 \text{ mm} = 3.75''$) laid up as UD ply and clamped in the PFT.	
4-layers	4 layers (0/0/0/0) laid up by an AFP machine. Width of specimen was $198 \text{ mm} = 7.8''$.	

Intention of the single-tow setup was to apply shear within a single tow. 15 tows had been tested in parallel to provide a measureable force level. Gaps between the tows had been left to avoid interactions of adjacent tows. The single layer setup represents the

behavior of a single ply as laid-up by an AFP machine. The 4-layers laminate was used to have a more stable specimen and to investigate the shear behavior in a laminate.

The experiments showed it was not possible to apply a shear deformation on the tows for the single-tow setup. The tows underwent a twisting in longitudinal direction rather than a homogenous shear deformation. This effect resulted on the one hand because of the high shear stiffness of the material but and on the other hand on the clamping conditions in the PFT. Fig. 4-10 shows the twisted tows and a sketch of the clamping constraint in the PFT. The tows are fixed in their position during the whole test. They initially point out perpendicular from the clamps and keep this orientation till the end of the test. Theoretically the tows should rotate freely at the clamp edges to undergo a pure shear deformation. But due to the fixed clamping the tows have to undergo an in-plane bending to account for the missing rotational degree of freedom. This in-plane bending leads to a compression of the tow at the inner edge and a tension at the outer side. With the high Young's modulus of the fibers high stresses occur which lead to buckling especially in the compressive region (inner edge). The buckling then forces the tows to twist. This effect can be also seen in AFP process when tows are placed/steered in too small radii [4].

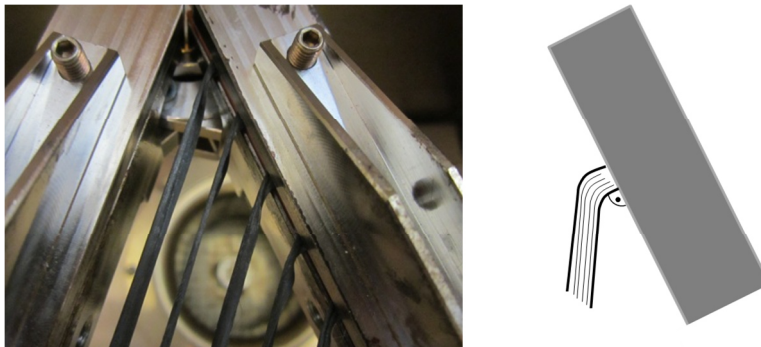


Fig. 4-10 Clamping influence on AFP tows in a PFT

Twisted single AFP tows in a sheared PFT (left); sketch of the clamping constraint of a tow in the PFT (right).

The measured forces in the single-tow tests were almost zero and had not been able to be captured by the 10kN load cell. Therefore the results are not presented here and are not used for simulations in this work.

In the single layer test setup the tows behaved almost in the same manner as in the single-tow setup. During testing the tows started to separate from each other and subsequently started twisting like single tows (Fig. 4-11). In spite of neatly manufacturing the specimens, not all tows were melted together. But even the bond between the tows was too weak to transfer forces from one tow to another. Right after starting the test the tows separated from each other and the whole specimen behaved like single tows.

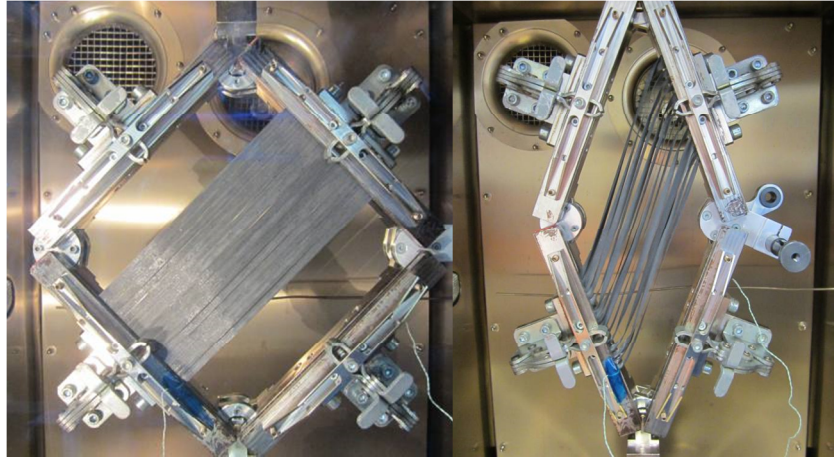


Fig. 4-11 PFT of a single layer AFP material

In this setup the measured force was again close to zero and not measurable with the load cell. Likewise the results are not presented here and will not be used for the simulations in this work.

The most promising results were provided with the 4-layers laminate. The specimen consisted of four single layers staggered on top of each other to avoid any butt splice over the whole laminate thickness. This increased the cohesion between the single tows and allowed to transfer in-plane forces among the tows. Even though it was the most stable test setup, applying shear on the specimen was only possible up to approximately 2° - 4° shear angle. Further shear deformations lead to wrinkling of the laminate and to a tear apart in the last shear states (Fig. 4-12).

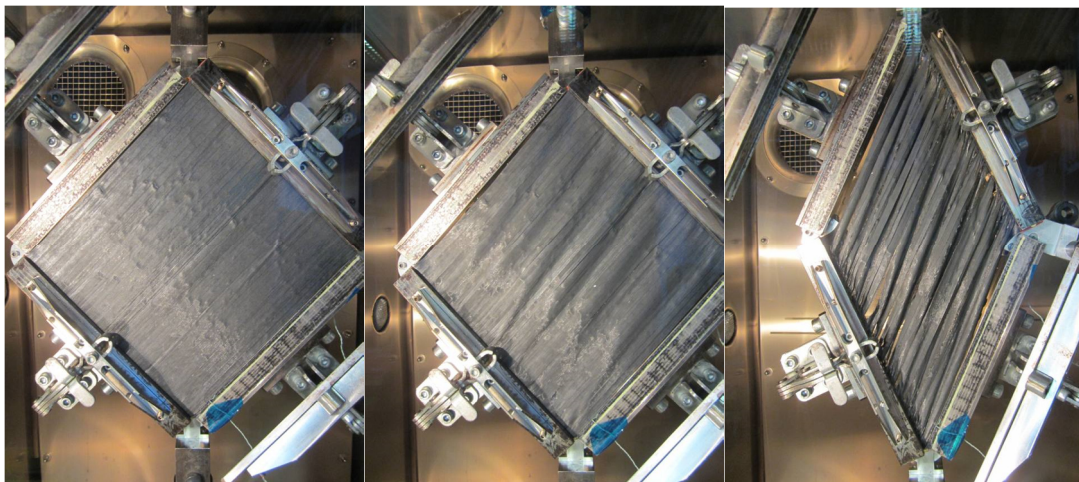


Fig. 4-12 PFT of the 4-layers laminate

Initial state (left); intermediate state $\sim 2^\circ$ shear angle (center); final state $\sim 40^\circ$ shear angle (right)

The formation of wrinkles appeared to be a major problem in determining the correct shear behavior of the AFP material. A pure shear deformation was present only before wrinkling started. Beyond this point the specimen also underwent bending and tensile deformations. The measured force cannot be assumed as pure shear force, since it is

superimposed by bending and tensile stresses. Fig. 4-13 shows an exemplary curve of the recorded machine force versus the head displacement. It shows an increasing force until ~15 mm displacement and a decrease of the force until the end of the test. Until ~10 mm displacement ($\cong 4.1^\circ$ shear angle) the specimen was deformed without any wrinkles as inspected with the naked eye. At higher forming degrees the measured force drops because of wrinkles and tearing apart of the specimen.

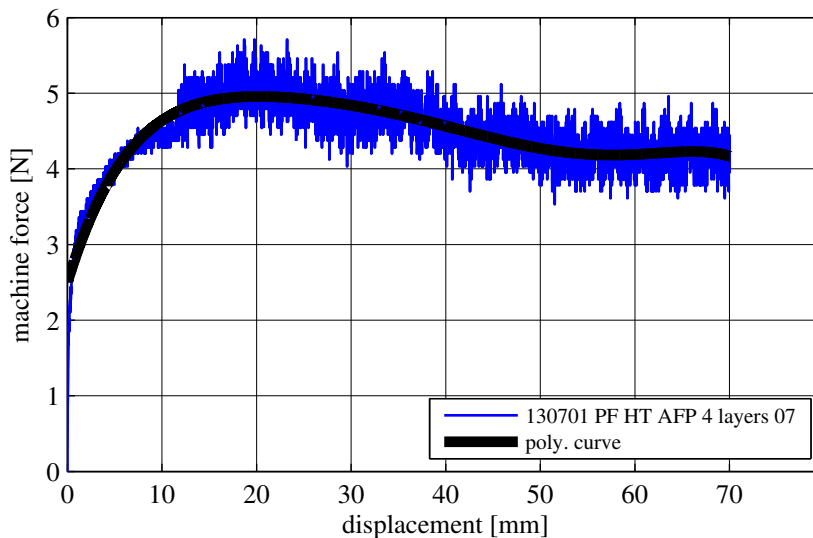


Fig. 4-13 Raw data of PFT with additional smoothing spline

To understand the formation of wrinkles and the mechanics taking place in the PFT, further studies have been made. It showed up that the wrinkles arose because of three reasons.

One reason already showed up in the other test setups: Inhibition of the in-plane bending at the clamps. To counteract this effect some PFTs have been carried out by using soft silicone strips on the clamps trying to allow a certain rotation of the tows at the clamping edge. Additionally, the clamping force was decreased. But both efforts did not improve the test results.

A second reason is the low bond between adjacent tows. To apply a homogenous shear over the whole specimen the shear stress need to be transferred from tow to tow. The staggering of the single plies helped to stabilize the laminate only up to a certain degree. At higher shear strains the tows again started to separate and tore the laminate apart.

The third reason for formation of wrinkles resulted from membrane buckling effects. The specimen can be assumed as a membrane since it is very thin and has large areal spread. Consequently the bending stiffness is negligibly small compared to the in-plane stiffness. The maximum stresses occurring in a UD prepreg can be qualitatively ordered as followed:

$$\sigma_{bending} \ll \sigma_{matrix} \ll \sigma_{shear} \ll \sigma_{fiber} \quad (4-6)$$

The magnitude of the maximum bending stress $\sigma_{bending}$ is the lower than the magnitude of the maximum stress σ_{matrix} which can be applied in-plane on the matrix. Higher stress magnitudes occur in shear deformations of the ply and in traction or compression of the fibers. The PFT applies a pure shear deformation on the specimen (instead of simple shear) which leads to a compression in matrix direction (Fig. 2-4). Due to small imperfections in the material, the in-plane stress is not perfectly balanced through the thickness. At a certain shear state a further increase of the in-plane stress leads to a redirection of the stress field and the material starts to buckle which shows up as wrinkles. In fact, this effect also happens by shearing dry woven fabrics. As mentioned in 2.1.1, woven fabrics can undergo a shear deformation until fiber jamming starts (“locking angle”). A further shear increases the in-plane stresses, which cannot be kept in-plane and the material starts to wrinkle.

The effect of membrane buckling can be also shown by regarding the geometry and alignment of the wrinkles, respectively. The alignment of a wrinkle is mainly governed by the acting stress field and the stiffness properties in the material. The shear stress acting on a PFT results in a global tension and compression field. If for example an isotropic material in a PFT is sheared the wrinkles align along the tension field since the compression field forces the material to buckle (Fig. 4-14). In this case the wrinkle alignment is only governed by the stress field. But if an orthotropic material like a UD prepreg is sheared the alignment of the wrinkles redirects along the fiber direction.

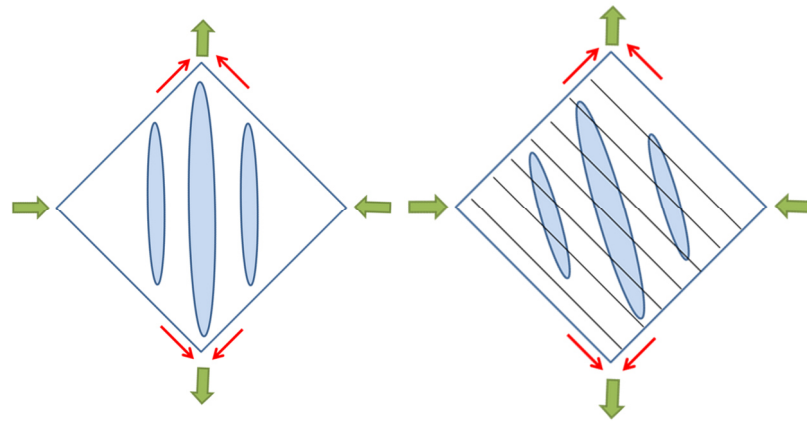


Fig. 4-14 Influence of compression and tensile forces in a PFT

The blue areas are indicating the wrinkles for an isotropic material (left) and an orthotropic material (right)

The redirecting of the wrinkles in a textile is governed by the imbalance of the in-plane properties: High stiffness in fiber direction and low stiffness in matrix direction. To form a wrinkle the material needs to undergo an elongation perpendicular to the wrinkle. This is not possible if the fibers are clamped at both sides. Hence, the in-plane stresses in the PFT still lead to buckling but the direction changes with respect to the

lower in-plane stiffness. Fig. 4-15 shows this effect for two UD preregs in the PFT with different fiber directions. The left picture shows a specimen with some fibers clamped at both sides which lead to a fold in fiber direction. The right picture shows a specimen with no fiber clamped at both sides and the fold aligns according to the global stress field.

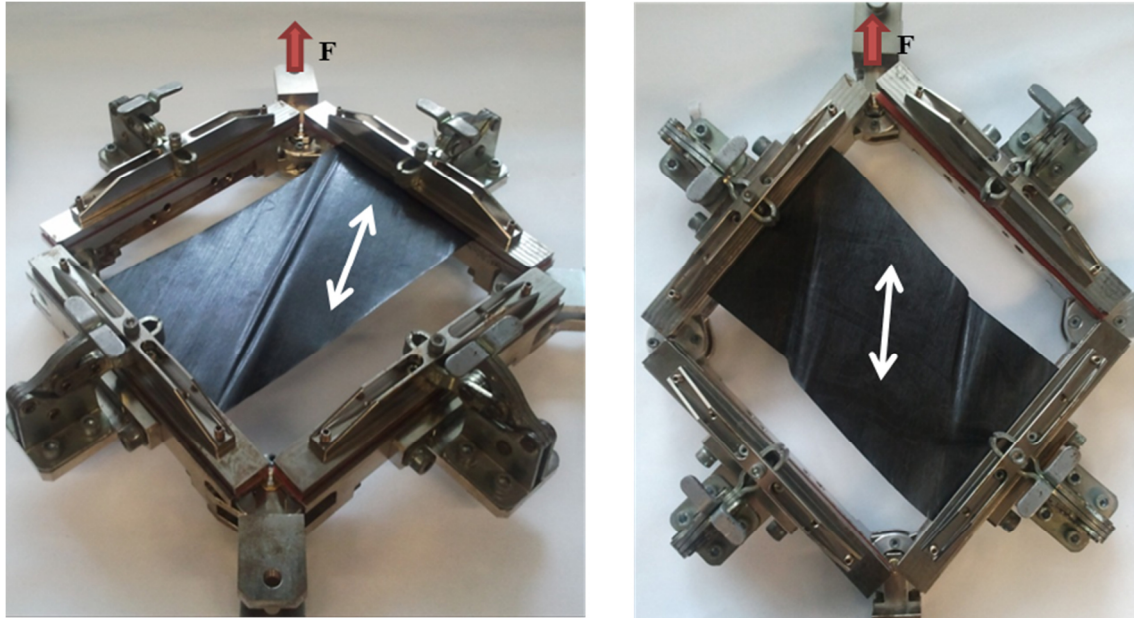


Fig. 4-15 Wrinkle formation in a PFT for a UD prepreg
Specimen aligned in different directions (the white arrows indicate the fiber direction)

Even though none of the different material setups sheared without wrinkles, the data of the 4-layer setup was used and further processed for this work.

Six tests have been carried out with the 4-layer setup using the above shown PFT. The specimen temperature was tried to keep constant throughout all tests ($65.5^{\circ}\text{C} \pm 2.9^{\circ}\text{C} \triangleq 150^{\circ}\text{F} \pm 5.1^{\circ}\text{F}$). The sizes of the specimens were 240 mm (fiber direction) x 198 mm x 0.956 mm and they were fixed with two clamps in fiber direction (Fig. 4-12). Fig. 4-16 shows the force displacement curves of all tests. All recorded force curves showed a strong noise due to the use of the 10 kN load cell at low force values (Fig. 4-13). For the postprocessing 6th-order polynomials were used to fit the final curves.

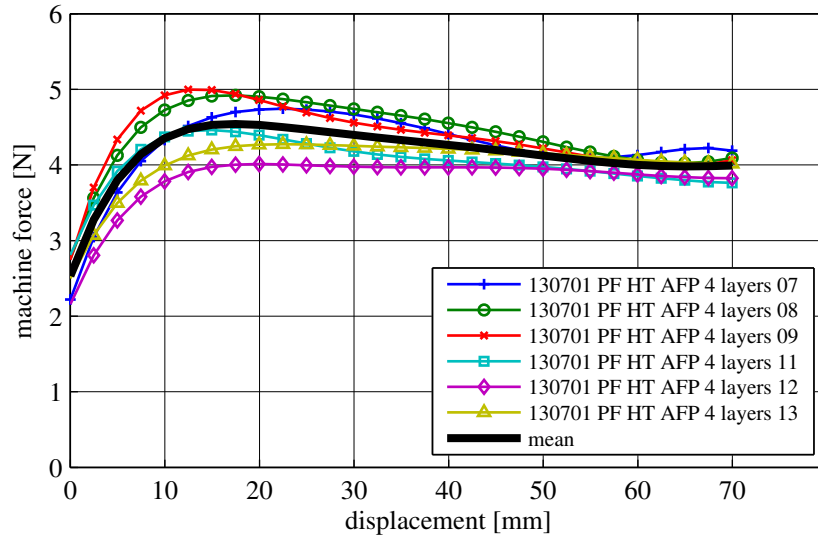


Fig. 4-16 Machine force vs. displacement of PFT with 4-layer material setup

Within the range of 5 mm to 70 mm the polynomial fitting was sufficient. But the force behavior at the beginning before wrinkling started required a higher accuracy. Hence, for the first 5 mm displacement ($\sim 2^\circ$ shear angle) a separate 6th-order polynomial was fitted and interposed in the overall force-displacement curve. Fig. 4-17 shows the fitted polynomials for the first 5 mm of displacement.

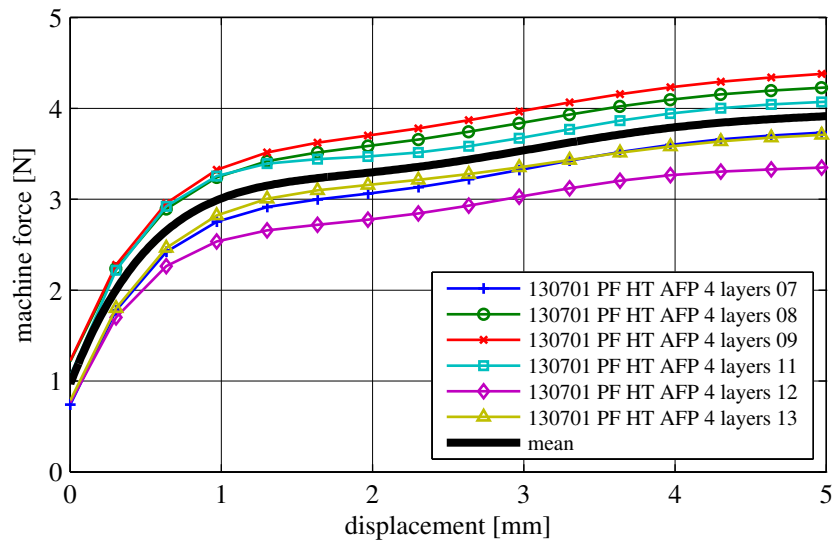


Fig. 4-17 Starting shear behavior of the AFP material in the PFT

The final force-displacement curve was generated by the mean of all polynomials from 0 mm to 5 mm and from 5 mm to 70 mm. As final curve one can use the following general polynomial function:

$$F_m(d) = \sum_{i=0}^6 a_i x^i \tag{4-7}$$

with the following coefficients:

	for $d \leq 5 \text{ mm}$	for $d > 5 \text{ mm}$
$a_0 =$	0.968	2.532
$a_1 =$	4.348	0.356
$a_2 =$	-3.444	-0.024
$a_3 =$	1.409	8.023e-4
$a_4 =$	-0.299	-1.443e-5
$a_5 =$	3.150e-2	1.327e-7
$a_6 =$	-1.301e-3	-5.000e-10

A conversion of the machine force into shear force and head displacement into shear angle is relinquished. Past the point when wrinkling started, the measured force cannot be interpreted as pure shear force. Bending and tensile force are additionally acting in this stage. Likewise, the displacement is not totally applying shear deformation. As a consequence, a shear force versus shear angle curve which is often shown in literature will not be given here. Only the machine force versus displacement data will be used for deriving the material card in the subsequent simulations.

4.2 Bending Test

The following chapter introduces different test methods for characterizing the bending behavior of composite textiles. Test methods that will be introduced have their origins in apparel industry and are suitable for testing composite textiles. Commonly used bending tests like the 3-Point- or 4-Point-Bending Tests are not adequate for non-cured composite textiles. Due to their low bending stiffness the specimen would tend to bend already under their own weight in these tests.

4.2.1 Test methods

Cantilever test

The Cantilever test for characterizing the bending stiffness of a textile is based on the Peirce's theory [34] (cf. 2.1.2) and used in different standards [37], [38],[99]. Fig. 4-18 shows the setup of the Cantilever Bending test and the test equipment used for this work.

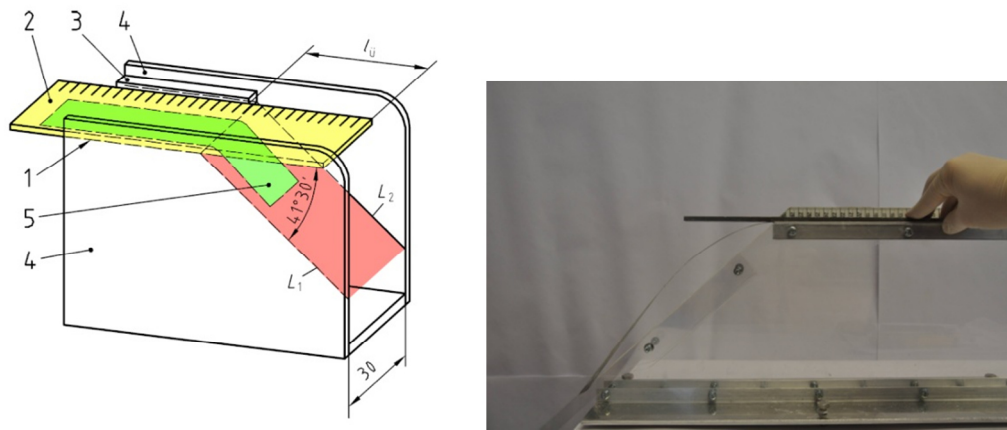


Fig. 4-18 Setup and principle of the Cantilever bending test

Test setup according to the standard DIN 53362:2003-10 [37] (left); the Cantilever bending test used in this work [91, 100] (right).

The Cantilever test requires a rectangular specimen strip (5). Prior to testing, the length and weight of the specimen strip have to be measured. At the beginning of the test the specimen strip (5) is placed on the horizontal plane (1) with the front end flush to the front edge of the horizontal plane. A slider with a scale included is placed on top of the specimen. By moving the slider over the edge of the horizontal plane it takes along the specimen. While moving the specimen, it begins to bend under its own weight. The moving of the specimen need to be stopped as soon as the front end of the specimen touches the inclined plane of 41.5° . From the slider scale one can readout the overhanging length l of the specimen.

To calculate the bending stiffness first the weight per unit length F_l need to be calculated.

$$F_l = g * \frac{m}{l_0} \quad (4-8)$$

The normal gravity is denoted by g , the mass of the whole specimen by m and the length of the whole specimen by l_0 . The bending stiffness B is then:

$$B = F_l * \frac{l^3}{8} \quad (4-9)$$

KES-FB2

In the Cantilever test an indirect measurement of the bending stiffness is done by measuring the overhanging length. Kawabata's test series KES-F provides the bending test KES-FB2 which measures the bending stiffness directly [27, 39, 40]. During testing the specimen is clamped on both sides. One clamp is fixed while the other one is rotating in positive and negative direction about the fixed clamped (Fig. 4-19). As output the bending moment versus the bending curvature is given. Fig. 2-8 shows a typi-

cal output of the KES-FB2 indicating also the non-linear and hysteresis behavior of a textile.

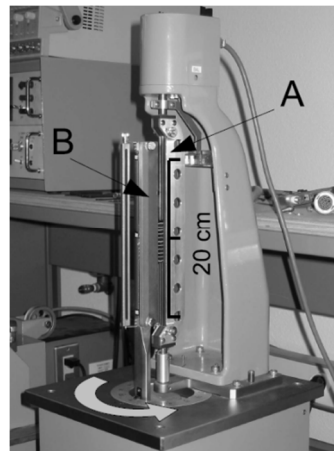


Fig. 4-19 Kawabata bending test - KES-FB2 [27]

Schlenker Test

Another method for measuring the bending stiffness is the test according to Schlenker describe in the standard DIN 53864 [101]. As in the Cantilever test the specimen is clamped on one side and bends under its own weight. Furthermore an additional force is applied at the free end (Fig. 4-20) to realize different bending angles and to measure the bending stiffness also in non-linear regions. The results of the test are certain bending stiffness related to certain bending angles.

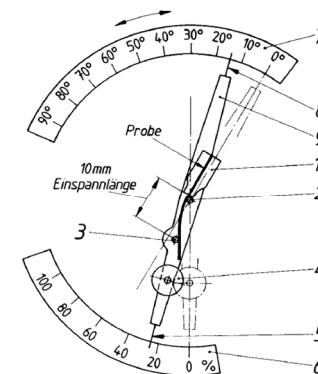


Fig. 4-20 Principle of the bending test fixture according to Schlenker [101]

Flexometer

Bilbao et al.[27, 31] introduced an improved bending test according to Pierce but with an optical measurement. This flexometer determines the bending properties of a specimen under its own weight and possibly with additional mass. In addition an optical bending modulus is derived by the optical measurement.

DMA

All test methods mentioned above are mainly designed for testing at room temperature. Ongoing research at the LCC is dealing with new test methods using a Dynamical Mechanical Analysis (DMA) machine. In the DMA different loading scenarios can be applied on a specimen for temperatures between -150°C till $+600^{\circ}\text{C}$. First results are still pending and hence will be not covered in this work.

4.2.2 Test results

For the characterization of the bending behavior the Cantilever test has been chosen. The Cantilever test provides a single value for the bending stiffness which is taken at a bending angle of 41.5° . As mentioned earlier a textile evolves a non-linear behavior when bending at high degrees (cf. 2.1.2). Nevertheless the Cantilever test will be used since the material model of PAM-FORM only accounts for a constant value of the bending modulus B .

The bending stiffness of the AFP material was determined in fiber direction and in matrix direction. To test at forming temperature a heat gun was used to heat up the test rig and the specimen. Additionally, the specimens were treated with talcum powder to reduce the tackiness for avoiding the specimen to stick on the test rig.

The bending stiffness in fiber direction was measured by using a single AFP tow. 14 tests were carried out and a mean bending stiffness of 11.06 Nmm^2 was determined. The standard deviation about all tests was 1.45 Nmm^2 . Fig. 4-21 shows the results of the 0° -bending tests.

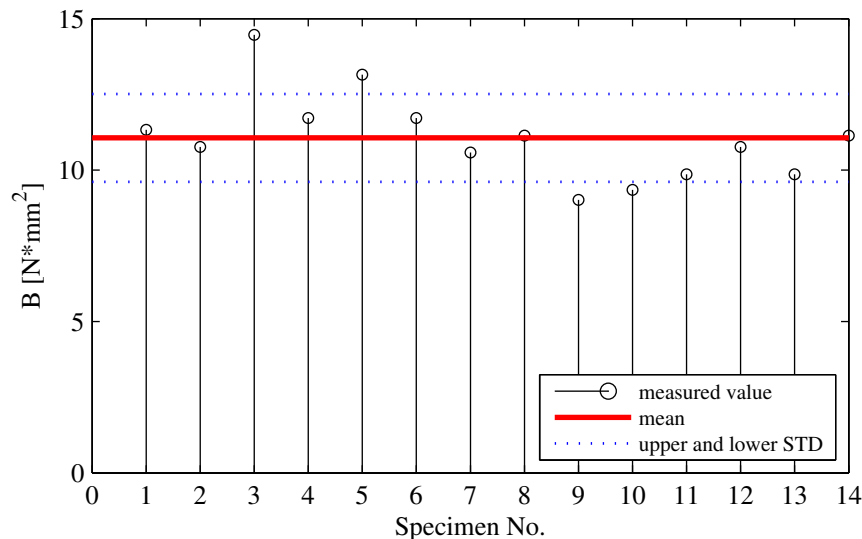


Fig. 4-21 Bending Test results for 0° -direction of a single AFP tow

The characterization of the AFP material in 90° direction was done by joining single tows by small overlapping (Fig. 4-22).



Fig. 4-22 90°-specimen used for the bending test

Fig. 4-23 shows the results of the bending stiffness for the AFP material in 90° direction. The mean bending stiffness was $4.95 \times 10^{-3} \text{ Nmm}^2$ and the standard deviation $2.85 \times 10^{-3} \text{ Nmm}^2$. Testing of the 90° specimen at elevated temperatures was difficult to perform with the Cantilever test. The airflow of the heat gun might have influenced the testing which lead to the relative high standard deviation.

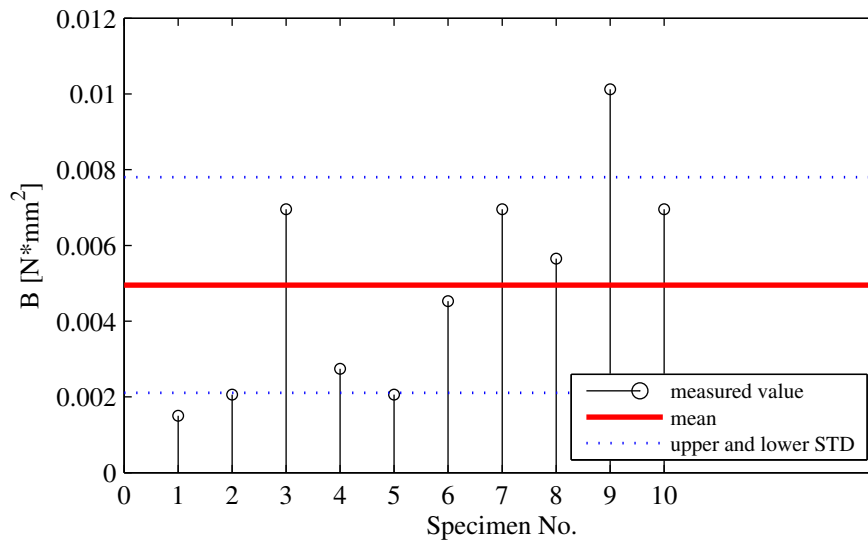


Fig. 4-23 Bending test results for 90°-direction

4.3 Friction Test

Even though preimpregnated textiles exhibit a non-linear friction behavior with respect to temperature, velocity, pressure, and contact area, only the linear Coulomb friction will be used in the simulation model. In this chapter different test methods will be presented, which are commonly used for friction testing of composite textiles. Some test methods are based on ASTM and DIN norms, but none of them is explicitly for use with composite textiles.

4.3.1 Test methods

Inclined plane

Dong [102] described a test method according to the standards ASTM G115-93 and ASTM D4521-9. It involves the measurement of the friction coefficient between an inclined plane and a block placed on top of it (Fig. 4-24). By constantly increasing the plane's angle the block eventually starts to move. The angle is recorded and the static friction coefficient μ_{st} can be calculated. This measurement method allows testing the friction coefficient of different material combinations by attaching them on the block and the inclined plane.

$$\mu_{st} = \tan(\alpha) \quad (4-10)$$

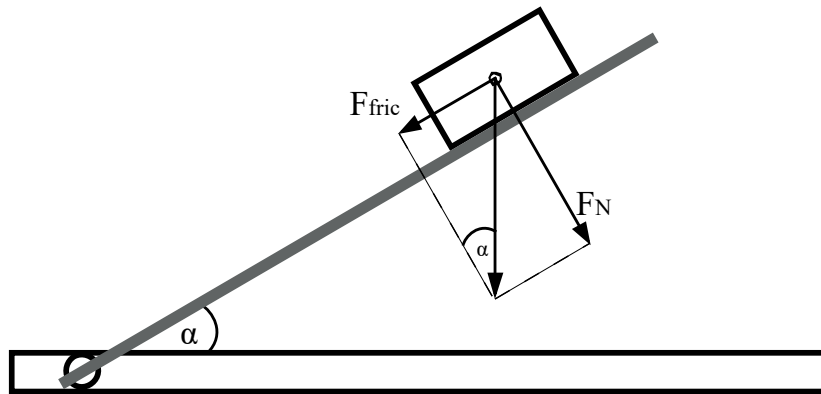


Fig. 4-24 Principle of the Inclined Plane friction test

The dynamic friction coefficient μ_{dy} is defined as the ratio between friction force F_{fric} and the normal force F_n which lead to a constant velocity [103]. For this purpose the inclined plane needs to be lowered until the block has a constant velocity.

$$\mu_{dy} = \tan(\alpha_d) \quad (4-11)$$

Horizontal plane

The standards ASTM D 1894-01 [104] and DIN EN 14882 [103] describe the friction test on the horizontal plane. A carrier is pulled by a tensile testing machine via a string over a horizontal plane (Fig. 4-25). With the recorded machine force F_{fric} and the weight of the carrier F_N the friction coefficients μ_{dy} can be calculated:

$$\mu_{dy} = \frac{F_{fric}}{F_N} \quad (4-12)$$

The static friction coefficient μ_{st} is calculated from the first force peak. For the dynamic friction coefficient the whole record is divided into four equal parts and the mean

force value of the two middle parts is used to calculate the dynamic friction coefficient.

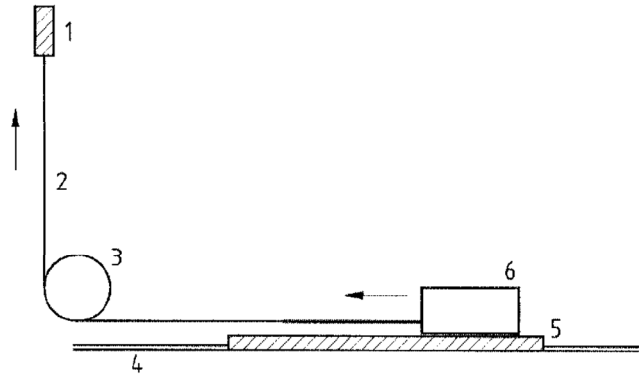


Fig. 4-25 Friction test on the horizontal plane

(1) load cell, (2) string, (3) low-friction pulley, (4) flat plane, (5) specimen and (6) carrier [103]

KES-FB4

Kawabata's test series KES-F includes the friction measurement KES-FB4 Surface Tester. A sensor tip with a defined load is slid over the textile surface to determine the friction force (Fig. 4-26).

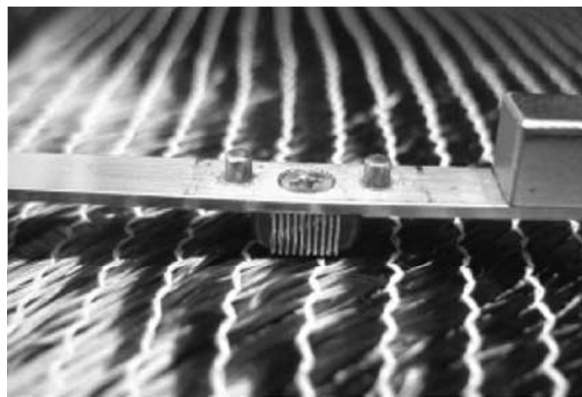


Fig. 4-26 Friction test KES-FB4 [40]

Pull-Through and Pull-Out

For testing impregnated textiles the determination of the friction coefficient is done at defined temperatures. Predesigned test principles are the Pull-Through and the Pull-Out test (Fig. 4-27). Both tests consist of two plates pushing against each other while the textile in-between is pulled in perpendicular direction. The only difference is the decreasing contact area in the Pull-Out test compared to the constant area in the Pull-Through test. Both tests can be implemented in a tensile testing machine or as stand-alone device (Fig. 4-28). Main advantage of these tests is to vary the normal pressure,

the temperature, the pulling speed as well as the contact area [45, 46, 105, 106]. The friction coefficient μ_{dy} is calculated by:

$$\mu_{dy} = \frac{F_{fric}}{2F_x} \quad (4-13)$$

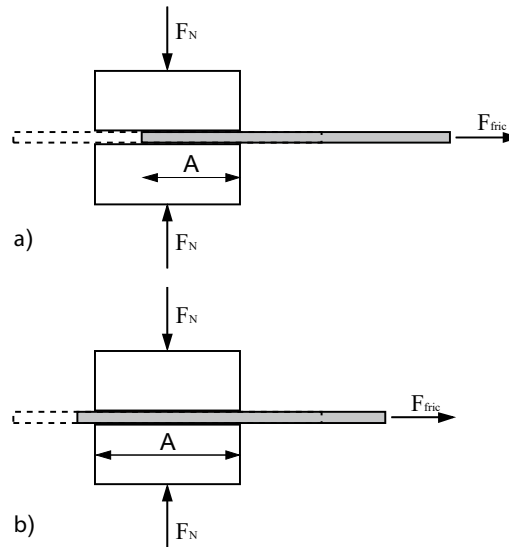


Fig. 4-27 Principle of the Pull-out test (a) and the Pull-through test (b)

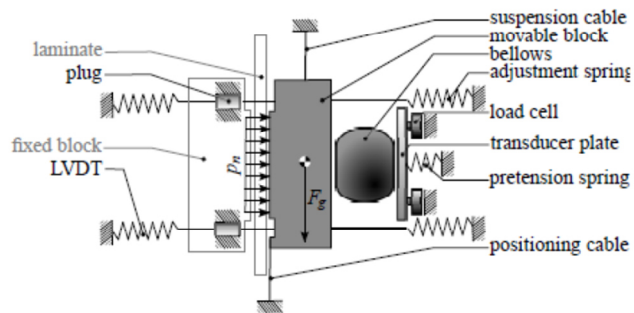


Fig. 4-28 Pull-Through tests

Test rig of LCC (left); stand-alone device from Akkerman et al. (right) [46]

4.3.2 Test Results

Two friction tests have been developed within this work: The friction test on the horizontal plane (Fig. 4-29) and the Pull-Through test (Fig. 4-28). The Pull-Through test was designed and manufactured but had not been validated within the framework of this thesis. Hence, for characterizing the friction coefficients, only the test on the horizontal plane was used.

The friction tests were performed with different material combinations required for the subsequent simulations. To assure the testing at forming temperature a heat gun and an infrared lamp was used and the specimen temperature was controlled by an optical pyrometer. In preliminary tests strong stick-slip effects occurred, which had been reduced by applying a maximum pulling speed of 400 mm/min, using a stiff steel wire and reducing the total carrier displacement to 200 mm. The carrier weights 1200 g without specimen and has a surface area of 150 mm x 100 mm resulting in a pressure of 7.848×10^{-4} N/mm².

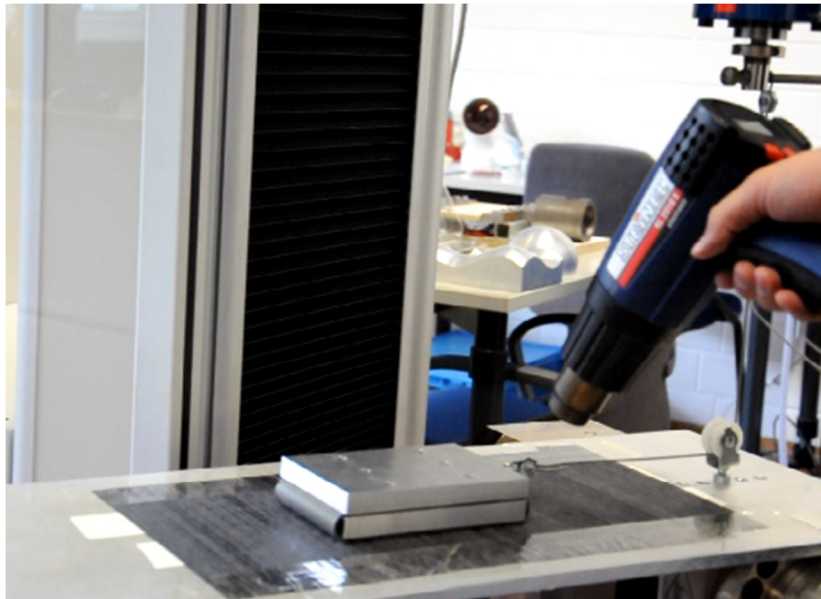


Fig. 4-29 Friction testing of AFP material using the horizontal plane

Solely the dynamic friction coefficients were measured. The time-dependent behavior did not allow determining the static friction coefficient. To perform the test the carrier was placed 10 s before running the test on top of the horizontal plane. This agglutinated the materials and lead to static friction coefficients ranges of $\mu_{st} = 1.5- 6.5$ (first measured force peak). Likewise other latency periods were investigated but all tests showed high variations in the first force peaks. Nonetheless, the subsequent simulations cannot account for time-dependent friction coefficients such that only the dynamic friction coefficients had been measured.

Tab. 4-3 provides the friction coefficients of all tested material combinations. The ply-ply friction was determined for different fiber alignments. Two kinds of bladder material were tested (required for the use case simulation). Further the friction of a release ply on different materials was determined. Aluminum, as the tooling material, was tested in combination with the bladders and with the release ply.

Tab. 4-3 Overview of the measured friction coefficients required for the simulation

test name	plane	carriage	friction coefficient
<i>AFP_FT_a</i>	alu	bladder (thick)	0.32
<i>AFP_FT_b</i>	alu	bladder (thin)	0.34
<i>AFP_FT_c</i>	0°	bladder (thick)	1.63
<i>AFP_FT_d</i>	90°	bladder (thick)	1.33
<i>AFP_FT_e</i>	0°	0°	1.37
<i>AFP_FT_f</i>	0°	90°	0.88
<i>AFP_FT_g</i>	alu	release ply	0.22
<i>AFP_FT_h</i>	0°	bladder (thin)	1.68
<i>AFP_FT_i</i>	90°	bladder (thin)	1.31
AFP_FT_1	90°	90°	1.14

4.4 Tensile Test

Characterization of the tensile behavior of composite textiles is rarely described in literature. The required tensile properties for the material models in draping simulation are mostly taken either from the data sheets of the manufacturer or are roughly assumed by taking stiffness values which are magnitudes higher than the other in-plane properties. The strain in fiber direction during draping is usually negligible small and does not need to be tested. But for UD prepregs and AFP materials the strain in matrix direction cannot be neglected and need to be characterized.

4.4.1 Test methods

Uniaxial tensile test

The simplest method for characterizing the tensile behavior is the uniaxial tension test. The specimen is clamped at both ends and pulled apart by a tensile testing machine, which records the force and displacement (Fig. 4-30). Optional, the displacement can also be tracked by optical measurement systems like Digital Image Correlation. The tension test does not require special clamps and can be carried out in a thermal chamber.



Fig. 4-30 LCC tension test with 4-layers laminate
Initial state (left); final state after rupture (right)

Biaxial tensile test

The biaxial tension test allows to characterize the tensile behavior in two directions individually or the dependency from each other. Especially for woven fabrics the interaction of warp and weft fibers is strongly interdependent. The test is build up by two perpendicular clamp pairs which are individually controlled (Fig. 4-31).

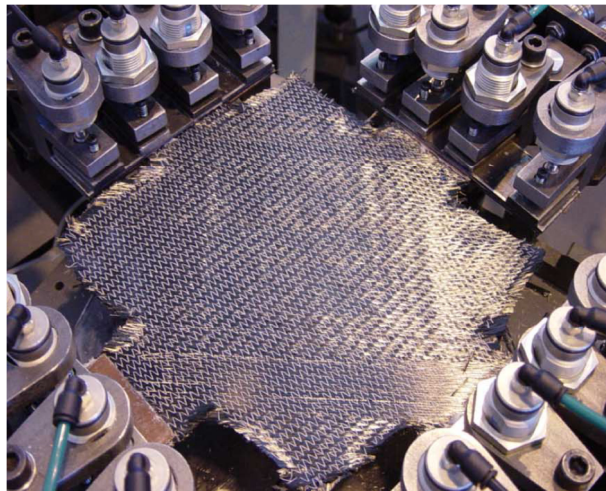


Fig. 4-31 Biaxial tension test [25]

KES-FB1

As mentioned in 4.1.1 the shear test KES-FB1 of Kawabata's test series also allows applying tension on the textile (Fig. 4-9). Lomov [40] used the test for characterizing NCFs, but discovered inhomogeneous clamping along the textile.

DMA

Another possible test method might be by using a DMA (cf. 4.2.1). It allows precise testing at low loads, which makes it predestined for characterizing UD prepregs in matrix direction. At that time the LCC starts to work on a suitable method to realize the testing in the DMA. Final results are still pending and will not be presented here.

4.4.2 Test results

The uniaxial tension test of Fig. 4-30 was used in this work. The two clamps had a width of 200 mm and clamped specimens of also 200 mm width. Two material setups have been investigated: Single tow and 4-layers laminate.

The single tow setup showed up to be difficult to handle. Each clamp required at least a clamping length of 2 mm, which only leaves a free length of 2.35 mm for a single tow. In some tests single filaments showed up, which had not been correctly aligned within the tow. Those filaments bridged from clamp to clamp and affected the testing result. In contrast, the 4-layers laminate allowed specimens with a free length of 3 mm, which were sufficient for testing.

To avoid any influence of the air vent within the thermal chamber, an additional metal plate was placed behind the clamps to shield the specimen (Fig. 4-30). All tests were performed at 65.5° C and with a pulling velocity of 50 mm/min. The tensile testing machine recorded the force and the displacement. Fig. 4-32 shows exemplary the raw data of one test. Since very low forces occurred the load cell passed back a noisy signal. For the subsequent data processing a 6th-order polynomial was fitted onto the data.

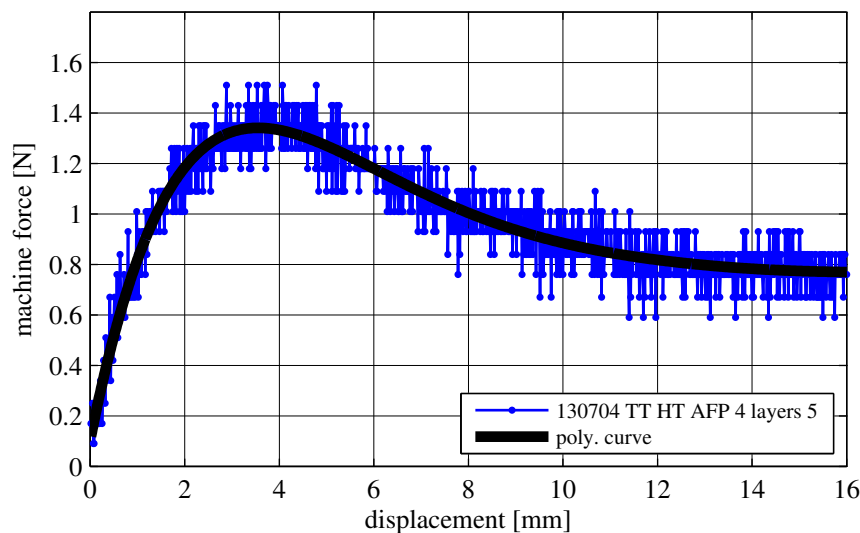


Fig. 4-32 Raw data of the tensile test for a 4-layers laminate

Eight tests were carried out with a displacement of 10.5 mm leading to a logarithmic strain of $\epsilon_{ln}=0.3$. The material showed a very sensitive behavior (Fig. 4-33). The inconsistencies in the results might come from small misalignments of the specimens. Nevertheless all results were taken into account to derive a mean stress-strain curve used for the simulation.

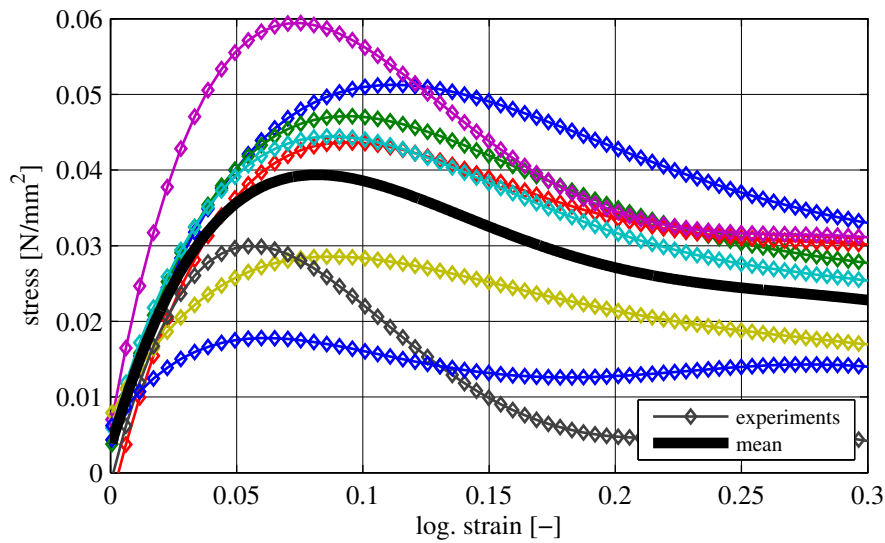


Fig. 4-33 Stress vs. logarithmic strain of the tensile test with 4-layers laminate

The calculation of the tensile stress was based on volume conservation of the specimen. Meaning, the used thickness t is dependent on the actual specimen length l :

$$t = \frac{t_0 * l_0}{l} \quad (4-14)$$

With the length l dependent on the head displacement d :

$$l = l_0 + d \quad (4-15)$$

Assuming a constant width b of the specimen during the tension test, the tensile stress σ_T is now written with the measured force F as:

$$\sigma_T = \frac{F}{b * t} \quad (4-16)$$

It has to be mentioned that the tensile stress is only valid until rupture starts. Thereafter, the rupture leads to a decrease of the cross section area which should be taken into account for the stress computation (Fig. 4-30).

The logarithmic strain ε_{ln} denotes as:

$$\varepsilon_{ln} = \ln \frac{l_0 + d}{l_0} \quad (4-17)$$

The final stress-strain curve of the tensile test can be written as a polynomial according to formula (4-7) with the following coefficients:

$a_0 =$	25.299
$a_1 =$	71.238
$a_2 =$	-112.254
$a_3 =$	56.265
$a_4 =$	-12.509
$a_5 =$	1.146
$a_6 =$	3.251e-3

4.5 Thickness measurement

The simulation model requires the material thickness to pass back the correct mechanical behavior. Here, the thickness values for a single tow and the 4-layers laminate are presented.

The thickness was determined by using a micrometer gauge. To avoid any compression of the specimen by the micrometer pins two additional razor blades were placed between micrometer pins and the specimen (Fig. 4-34). The measurements were taken from different specimens and at different positions. Tab. 4-4 provides the measured thicknesses for both material setups.



Fig. 4-34 Thickness measurement using a micrometer
The razor blades are used to avoid a compression of the specimen

Tab. 4-4 Thicknesses of the used material and the standard deviation (STD)

material	no. of measurement	mean thickness [mm]	STD [mm]
<i>single tow</i>	8	0.23	0.031
<i>4-layers</i>	10	0.87	0.035

4.6 Conclusion

In this chapter different material characterization methods were introduced which are required to determine the material parameters needed for PAM-FORM forming simulations. For each parameter different material characterization tests were presented, of which one was chosen to be used in this work.

For determining the shear stiffness properties of the AFP material, the PFT was chosen. A PFT rig was developed which ensured low frictional forces and the possibility to characterize materials even at higher temperatures. Three different setups of the AFP material were tested with PFT. The 4-layers laminate was chosen as it provided the most robust behavior. The AFP material itself revealed low shear properties with a maximum shear angle of only 4° before the specimen started wrinkling and tearing apart. Mainly the boundary conditions in the PFT led to this low shear angles. To reach higher shear states the clamps of the PFT should allow a free rotation of the specimen. Without free rotation the fibers tense and evolve parasitic forces during shearing in the PFT. Another reason was the free movement of the specimen in normal direction. The shear stresses which developed during shearing were beard by the specimen only until a certain degree. A further stress increase led to a redirection of the forces and to buckling and consequently wrinkling of the specimen. Hence, if the AFP material needs to be characterized at higher shear states, the specimen should be fixed to keep in-plane.

The bending properties of the AFP material were determined with the Cantilever test. Difficulties showed up by characterizing the specimens at elevated temperature. Especially the bending tests in 90° direction showed high deviations in the test results, because the short bending length could hardly be measured. In contrast, the 0° tests revealed robust results. All in all, the Cantilever test provided useful results for the AFP material at 65°C . However, if other materials should be tested or higher temperatures are required, the Cantilever test might reach its limits.

The friction coefficients for different material pairs were determined with the test on the horizontal plane. The test provided sufficient results for the dynamic friction coefficients. But the determination of the static friction coefficients was not possible. The static friction coefficient was strongly dependent on the time between the placing of the carrier on the horizontal plane and the start of the test. Nevertheless, this time de-

pendency cannot be accounted for in PAM-FORM and thus was not accounted for in this work.

The tensile behavior of the AFP material in matrix direction was determined with the uniaxial tensile test. The tests were carried out with the 4-layers AFP material. Most of the tested specimen showed similar behavior, but also some outliers occurred. Not all specimens looked alike and appeared to have every tow exactly next to each other. Some specimen had minor gaps between the tows which acted as small initial ruptures and decreased the tensile stiffness. Nonetheless, these specimens had been still included in the measurements, to taken into account manufacturing tolerances.

Last material test was the thickness measurement of a single tow and the 4-layers laminate. A micrometer gauge was used with additional razor blades in-between to avoid any compression of the specimen due to measurement forces. The measurement showed quantitatively good results and no further modification of the test method was required.

It had been possible to determine all the required material parameters for MAT140. Even though most of the tests originated from material characterization tests of dry textiles, the testing of the AFP material was still possible. However, the forming behavior of the AFP material is strongly dependent on the viscous behavior of the matrix. Taking the viscous behavior into account would require alternative test methods.

5 Material characterization simulation

The previous chapter presented different material characterization tests, their outcome and undesired effects which came along during testing. For instance the PFT intends to apply pure shear deformation on the specimen but wrinkles and parasitic tensile forces show up in parallel. A reliable interpretation to what extent the measured force resulted from shear deformations and not from tensile forces cannot be given directly. This chapter now presents a reverse approach which applies the FE simulation in order to model the material characterization tests. By simulating the experiments most of the uprising side effects can be also simulated. Within the simulation it is then possible to differentiate to what extent the measured force arises from the desired deformation and which portion originates from parasitic effects.

Additionally, this reverse approach helps to understand the mechanisms and the underlying constitutive equation of MAT140. The *ESI Group* does not provide the user the exact description of the material model which hinders to use the material model properly. Previous simulations revealed discrepancies between the simulation results and the expected results due to misunderstanding of the material model. For a realistic simulation result it requires modifications of the measured material parameters to ensure the simulation working properly. By simulating the material characterization tests one can now determine the material parameters which lead to a realistic forming behavior of MAT140.

Another advantage of simulating the material characterization tests is a better understanding of the interdependency within the different material parameters. In particular, MAT140 consists of three components (chapter 3.4), which should be independent from each other (chapter 3.1). But in older solver versions (\leq v2009) simulations showed an interdependency of the material parameters. For example an altering of the shear properties led simultaneously to a change of the bending properties. With the help of the reverse approach these parameter interdependencies can be investigated and assessed.

This chapter will present and detail the simulations of the friction test, the tensile test, the bending test, and the PFT. The order in which the simulations will be presented here, also demonstrate the most recommended way to setup the complete material card MAT140.

5.1 Friction test simulation

The modeling of the friction behavior showed up to be the most robust material parameter in the simulation. The friction definitions are independent from MAT140 and are standard options in PAM-CRASH /-FORM simulations. Nevertheless, the reverse approach was still applied here to check its accuracy and how to define best the friction within the simulation. The simulations in the following subchapter are mainly based on the work of Santner [107].

Model setup

A submodel of the friction test was set up to avoid extensive modeling efforts and a high computational time. In the model the horizontal plane had a size of 50mm x 14 mm with 5 x 5mm² elements and the carrier had a size of 10mm x 10mm with 1x 1 mm² elements (Fig. 5-1). It is recommended to use different mesh sizes for both contact partners and to avoid element edges lying directly on top of each other. Santner [107] showed that the penetration check of the contact lead to a drop of the friction force if a slave node is moving from one master element to the next. Because of that, the elements of the horizontal plane had been chosen to be larger than the carrier elements for avoiding too many element transitions of each node.

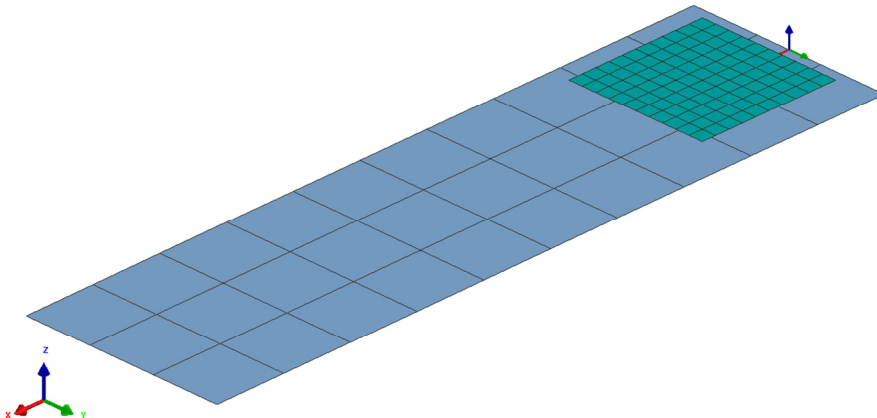


Fig. 5-1 Simulation model of the friction test at initial position

A symmetric node-to-segment contact (CNTAC=33) was used for the model. Due to its symmetry the selection of the master and slave contact partners can be arbitrarily chosen. For further reducing the dynamic effects during element transition of the carrier nodes it is recommended to include an additional contact damping (XDMP1=0.5).

An orthotropic friction model (IFROPT=10) was used to account for the direction dependency of the AFP material. The friction coefficients were oriented according to the fiber and matrix directions within the elements. PAM-FORM offers a velocity-dependent friction model, which can be used to account for the static and dynamic friction coefficients. But this option was not utilized for two reasons. On the one hand the friction tests provided only the dynamic friction coefficient. On the other hand, in

PAM-FORM the orthotropic friction model cannot be combined with the velocity-dependent friction model.

The carrier weight was applied by a pressure face definition (PREFA) on all elements. To avoid dynamic effects the pressure was increased from zero continuously to full pressure within 90 ms. The sliding/traction of the carrier started at 100 ms.

The movement of the carrier was defined via a velocity BC about all carrier nodes. The applied velocity was 0.16 mm/ms and the total sliding distance 38.4 mm, resulting in a total simulation time of 340 ms.

Simulation results

To validate the friction simulations different friction coefficients were used. The friction force was measured via the contact force output in sliding direction. With eq. (4-12) the friction coefficients of the simulations were determined and compared with the initially defined one. Fig. 5-2 shows a comparison of the friction simulation output with a predefined friction coefficient of $\mu = 0.88$. Small oscillations in the measured force showed up due to the element transitions of the carrier nodes. Nonetheless, the mean friction coefficient of this simulation revealed an error of 0.7 %.

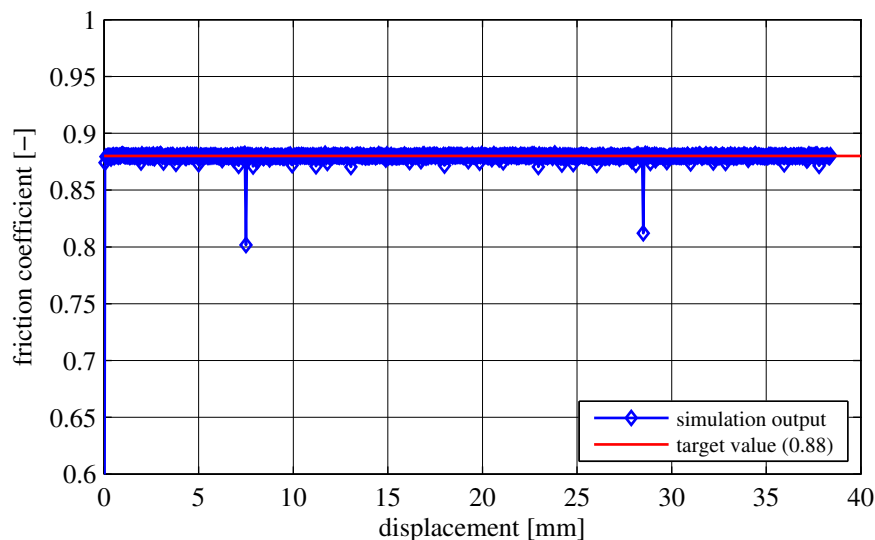


Fig. 5-2 Friction coefficient versus displacement of the friction simulation with $\mu = 0.88$

All other friction coefficients which were determined from the experiments showed likewise small errors in the simulation and will not be presented here. The study proofed the robustness of the contact and friction definition within PAM-FORM. Hence, the measured friction coefficients will be used in the subsequent simulations without any modifications.

5.2 Tensile test simulation

The simulations of the tensile test were done only for the tensile behavior in matrix direction. The Young's modulus in fiber direction was chosen $E_2 \geq 10$ GPa throughout all simulations. This value is high enough not to show any fiber strain in the simulation and low enough to keep the computation time acceptable (the time step calculation in an explicit FE code depends, amongst other parameters, also on the Young's moduli). The simulated tensile tests were based on the experiments with the 4-layers material setup presented in subchapter 4.4.2. The following model setup and interpretation of the results based on the preceded studies of Santner [107].

Model setup

The simulation model had the same size as the specimen in the experiment and was discretized with 5mm shell elements (Fig. 5-3). For the tensile simulation it is recommended to choose an element size such that in tensile direction at least one row of elements exist which is not constraint by any displacement BC.

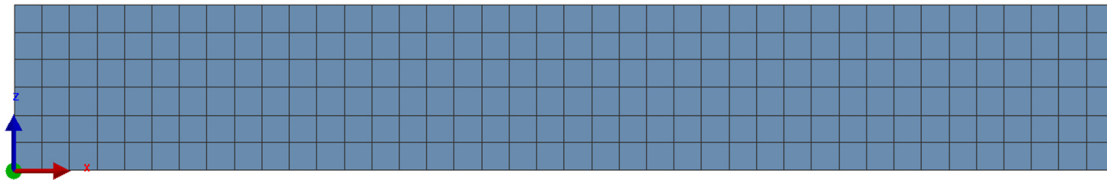


Fig. 5-3 Simulation model of the tensile test
Size of 200 mm width and 30 mm height consisting of 5 mm elements

The bottom edge was fully fixed and a displacement BC with a constant velocity was defined at the upper edge. The velocity BC had a pulling velocity of $v = 0.21$ mm/ms and a total displacement of 10.5 mm. Higher velocities should be avoided as the simulation then tends to show dynamic effects.

MAT140 requires as input either a constant value of the Young's modulus or a stress-strain curve. In this study the curve definition was chosen in order to account for the non-linear behavior of the material. Furthermore, it is important to uncouple the material model ($lunc = 1$), otherwise parasitic tensile stresses from the parent sheet of MAT140 will influence the tensile behavior (cf. subchapter3.4).

Simulation results

In the initial tensile simulation, the stress-strain data from the experiment were directly implemented. By looking at the strain distribution the first simulation result corresponded fairly to the experiment. As in the experiment the strain was homogenously distributed in the specimen at the beginning. At the point when rupture started, high strains occurred at a certain location (Fig. 5-4) and the specimen tore apart at this point. The simulation showed a likewise behavior. Fig. 5-5 shows the strain distribu-

tion at three different loading states. Until a displacement of ~ 5 mm all elements showed a homogenous strain. At a higher strain states only a single row of elements underwent a high strain which indicated the rupture of the material. The simulation model did not include an element elimination option to model the rupture. But the strain can be used as an indicator to identify locations where rupture takes place in forming simulations.



Fig. 5-4 Tensile test of 4-layers AFP material when rupture started

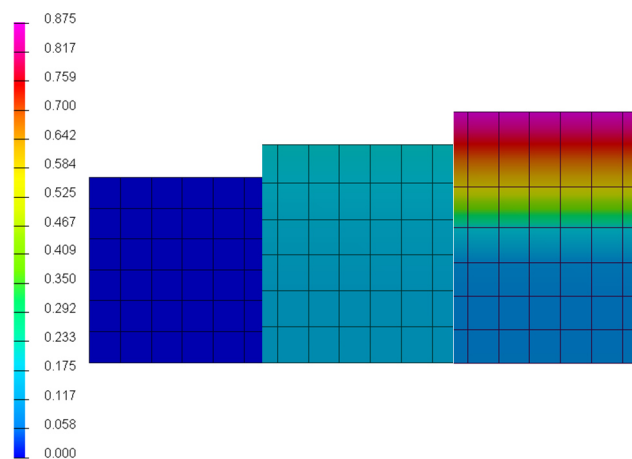


Fig. 5-5 Simulation of the tensile test

The contour plot shows the log. strain in matrix direction: initial state (left), 5 mm head displacement (center) and 10.5 mm head displacement (right)

However, checking the tensile forces within the simulation revealed a too stiff behavior of the first simulation. As Fig. 5-6 shows, the initial simulation had a higher maximum stress than in the experiment and additionally showed a drop of the tensile force at $\epsilon_m \approx 0.17$.

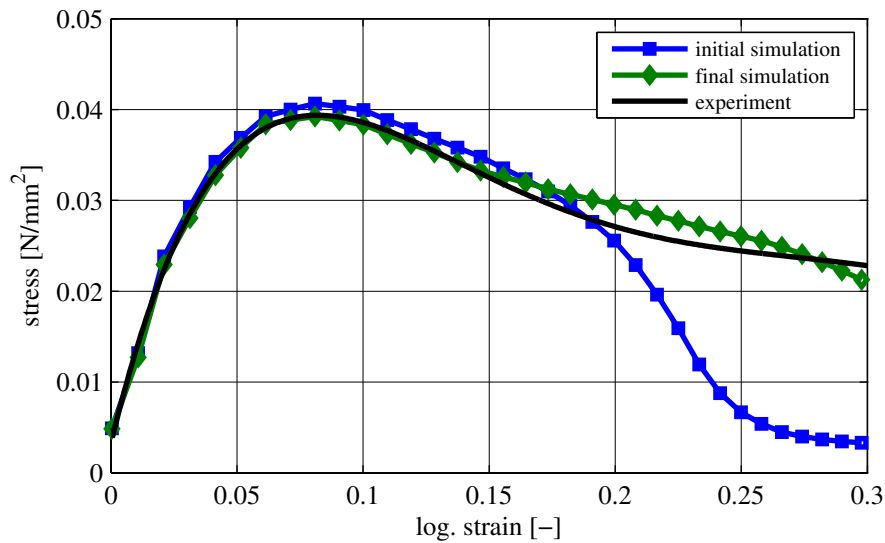


Fig. 5-6 Comparison of the tensile simulation with the experiment
Output for the measured stress-strain curve (initial simulation) and the modified stress-strain curve (final simulation)

The stress-strain curve was stepwise altered to fit the behavior onto the experimental curve. The percentage difference between simulation and experimental value at different strain points was superimposed to correct the input curve. This had been done till the desired value in the output was reached. But the fitting was limited only until a strain of approx. 0.15. It was not possible to perfectly control the tensile behavior in this post-rupture state. Regarding the input curves of Fig. 5-7, reveals that only minor changes had been applied at higher strain states. The large differences in the output (Fig. 5-6) indicate its sensitivity to small changes. Even though the final result did not fit the experimental curve totally, it still offers an acceptable behavior and was used for further simulations.

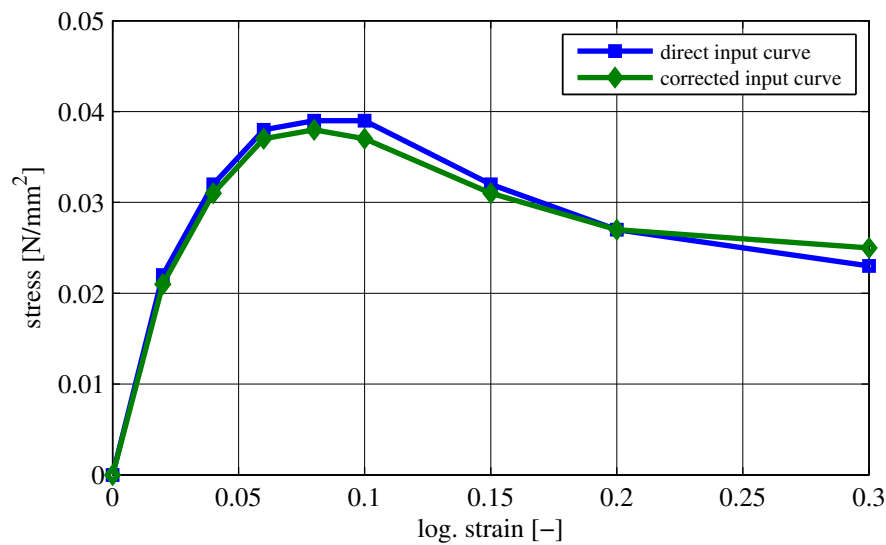


Fig. 5-7 Stress-strain input curve for implementation into MAT140
The plot shows the initial curve derived direct from the tensile test and the corrected (final) input curve

5.3 Bending test simulation

In particular, the bending test as a quasi-static test is not straight forward to model with an explicit FE code. In the experiment the specimen is loaded by its own weight and bends until it reaches a static force equilibrium. But explicit FE simulations are often governed by inertia effects. These evolve a swinging of the specimen during simulation which needs to be counteracted by applying additional damping functions.

This subchapter introduces a simulation model according to the measurements of the bending test and explains its setup and BCs. The simulation model is mainly based on previous simulation studies of Santner [107]. He investigated the influences of different parameters on the simulation result. The most reliable model setup was applied in this work.

Model setup

First simulation attempt was to build up a model which had the same sequence as in the experiment. This model included the specimen, the horizontal plane and the inclined plane. As in the experiment the specimen moved across the edge of the horizontal plane and was bended by a gravitational load (Fig. 5-8). But the contact definition between the specimen and the horizontal plane led to severe swinging of the specimen [107]. While the shells of the specimen moved across the edge of the horizontal plane, the total contact force changed gradually and evolved this dynamic effect. After the specimen reached certain overhanging length the oscillations led to a sudden collapsing and wrinkling of the whole specimen. This effect evolved from numerical instabili-

ties and it was not possible to counteract it by use of any additional BCs or numerical stabilizing options.

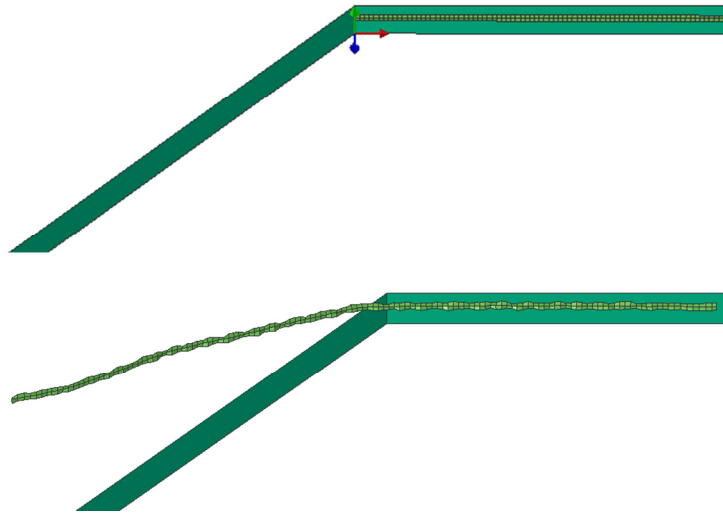


Fig. 5-8 Simulation of the bending test with a sliding specimen
Initial position of the specimen (top); collapsing of the specimen due to numerical instabilities [107]

A second simulation model, which was finally used, solely involved the overhanging specimen with the measured length from the experiment and the inclined plane (Fig. 5-9 and Fig. 5-10). The shells of the specimen were fully constrained at one end and a gravity load was applied to bend the specimen. Even though this simulation model showed a swinging of the specimen, it had been possible to minimize the dynamics by applying the load continuously and further defining a nodal damping [107]. The simulation time was set to 5000 ms in the 0°-simulation and to 2000 ms in the 90°-simulation to ensure a slow increase of the force and consequently a slow bending of the specimen. Furthermore, it has to be noted that no contact between the specimen and the inclined plane was defined. The inclined plane only assisted to indicate how far or close the specimens front edge was from the required 41.5° bending angle.

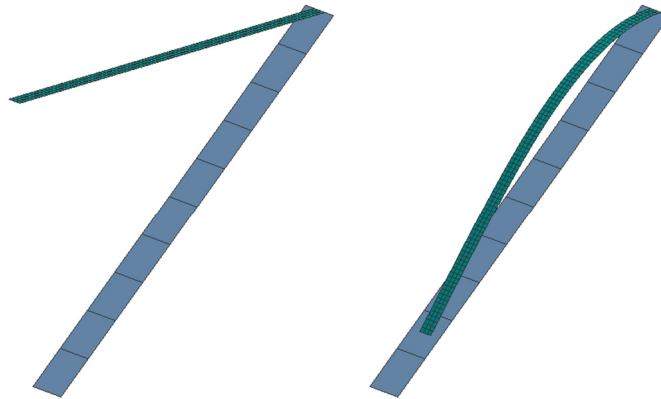


Fig. 5-9 Simulation model of the bending test in 0°-direction
Initial (left); final state (right)

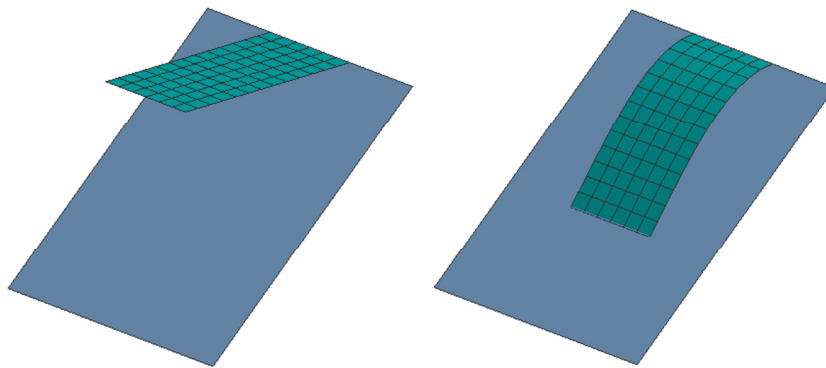


Fig. 5-10 Simulation model of the bending test in 90°-direction
Initial (left); final state (right)

The nodal damping option (*DAMP*) was used to stabilize the simulation model. This option adds a mass proportional damping to every node according to:

$$f_i = -m_i * q * v_i \quad (5-1)$$

Where f_i is the internal nodal damping force, m_i the nodal mass, q the damping factor and v_i the nodal velocity vector. As input, PAM-FORM only requires the damping factor. The critical damping factor q_{crit} can be computed via the oscillation time period T_{osci} (Fig. 5-11) of the non-damped system:

$$q_{crit} = 4\pi / T_{osci} \quad (5-2)$$

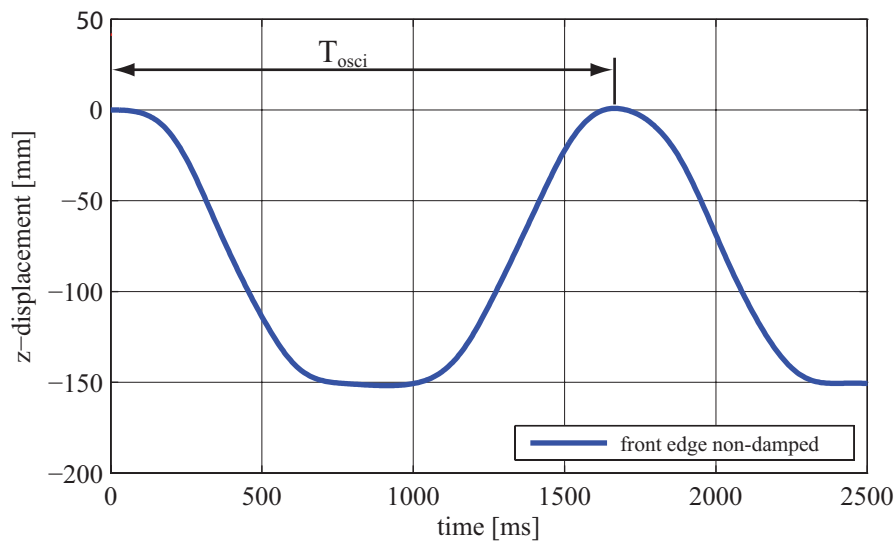


Fig. 5-11 Definition of the oscillation time period in the non-damped bending model

To avoid undesired effects by over damping the system only 80% of the critical damping was applied. Santner [107] performed simulations with non-damped systems and derived the mass-proportional nodal damping factor for 0° -direction simulation ($ADAMP = 6.056e-3$) and for 90° -direction simulation ($ADAMP = 2.9e-2$).

Another mandatory step in the bending simulation was the definition of nodal constraints at the edges nodes of specimen. The nodes needed to be constraint in y-direction as well as the rotational DOFs of x- and z-direction (Fig. 5-12). Without these constraints the specimen also collapses due to instability during the simulation (Fig. 5-13).

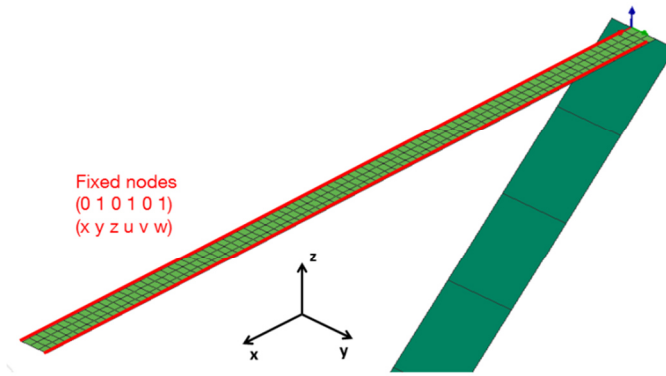


Fig. 5-12 Mandatory nodal constraints in the bending simulation [107]

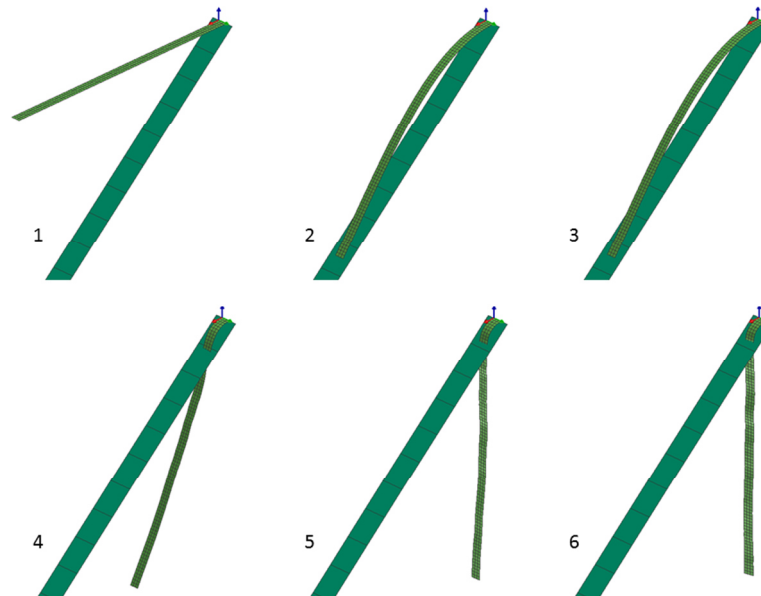


Fig. 5-13 Collapsing of the specimen in the bending simulation without predefined nodal constraints

Plots are shown the states every 750 ms [107]

As mentioned in subchapter 3.4, PAM-FORM requires either a bending factor which depends on the Young's modulus or a direct input of the bending modulus to define the bending properties of the material. The simulations of this work used the direct input of the bending stiffness to be independent from another material parameter.

Simulation results

First, the bending moduli in 0° -direction (1.718 GPa) and 90° -direction ($7.69e-4$ GPa) were implemented in the simulation. The displacements in x- and z-direction of the front end node were recorded to derive the bending angle. The model of the 0° -direction showed a bending angle of 41.62° and the model for the 90° -direction a bending angle of 39.87° . In 0° -direction the simulation model almost reached the target bending angle of 41.5° . The 90° simulation model showed a too stiff behavior.

Throughout iterative altering the bending moduli the correct bending modulus in the simulation was derived. The bending modulus of the 90°-simulation was multiplied by a correction factor of 0.935 leading to a modulus of 7.19e-4 GPa and a bending angle of 41.5°. In the 0°-simulation the bending modulus was multiplied by a correction factor of 1.005 which led to modulus of 1.727GPa and a bending angle of 41.49°.

Fig. 5-14 and Fig. 5-15 show the bending angle at the front end node for the 0°- and 90°-simulations. In the beginning the 0°-simulation showed an overshoot of the bending angle but reached a static balance at 2 s. The 90°-simulation converged asymptotically and reached the static balance at 1s.

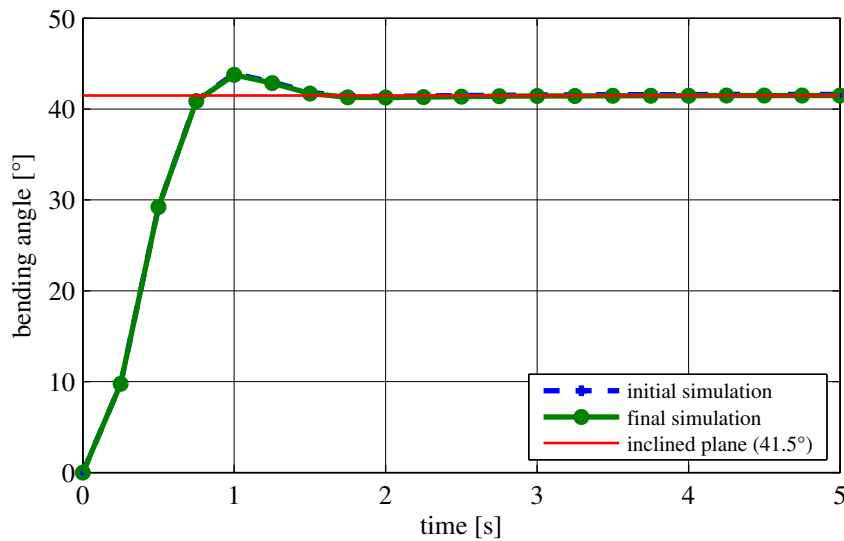


Fig. 5-14 Bending angle of the front end node in the 0°-bending test simulation

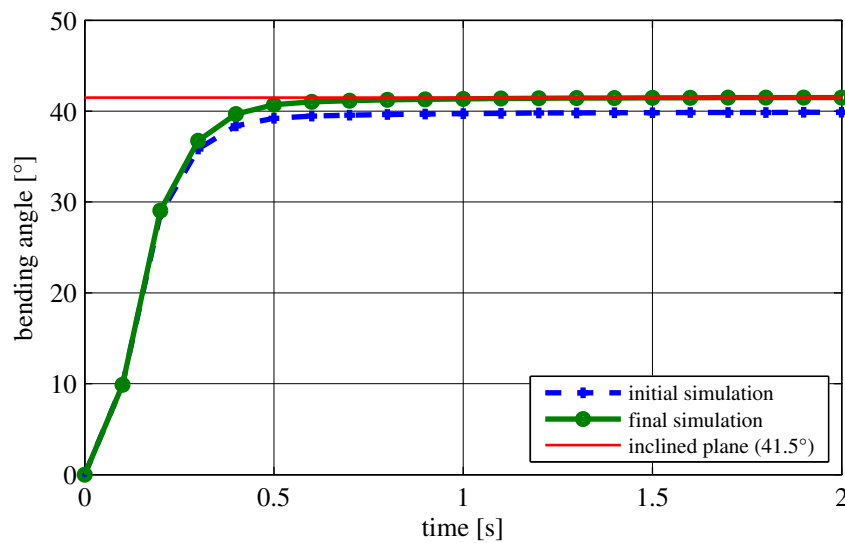


Fig. 5-15 Bending angle of the front end node in the 90°-bending test simulation

5.4 Picture Frame Test simulation

Subchapter 4.1 showed the difficulty of applying a pure shear deformation on the specimens with the PFT. The developing wrinkles induced bending and tensile deformation and consequently parasitic forces were measured by the load cell. It was not possible to extract the pure shear forces and the pure shear angles from the measurement. However, by knowing the bending and tensile behavior of the material, the shear behavior can be derived via the reverse simulation approach. In the following subchapter a suitable simulation model is presented to investigate the mechanics within a PFT and to derive the shear modulus curve of the AFP material. The simulation model based on the work of Santner [107], who performed different studies to investigate sensitive simulation parameters and their influence on the final result.

For the sake of convenience the shear behavior will be derived by using the measured machine force versus machine displacement curve. The generally used shear force versus shear angle curve will not be used here. Hence, the PFT will be simulated and the force and displacement at its top end will be recorded and compared with the experimental curve.

Model setup

The PFT rig was modeled with beam elements which were connected to each other by nodal constraint definitions (NODCO) to allow a rotation at the hinges. At the top and the bottom two additional beam elements were attached. These beams are required since PAM-FORM does not allow applying any other BCs if already nodal constraints are defined at a node. The lower node of the bottom beam was fully constraint to fix the frame. The upper beam was applied to a velocity BC with 0.08 mm/ms and an overall displacement of 80mm. Furthermore, the upper beam was used in the post-

processing to pass back the traction force (= machine force). In the material card of all beams an additional damping was included to reduce the dynamics within the PFT and to filter the measured force curve. Fig. 5-16 shows the PFT model with the specimen included.

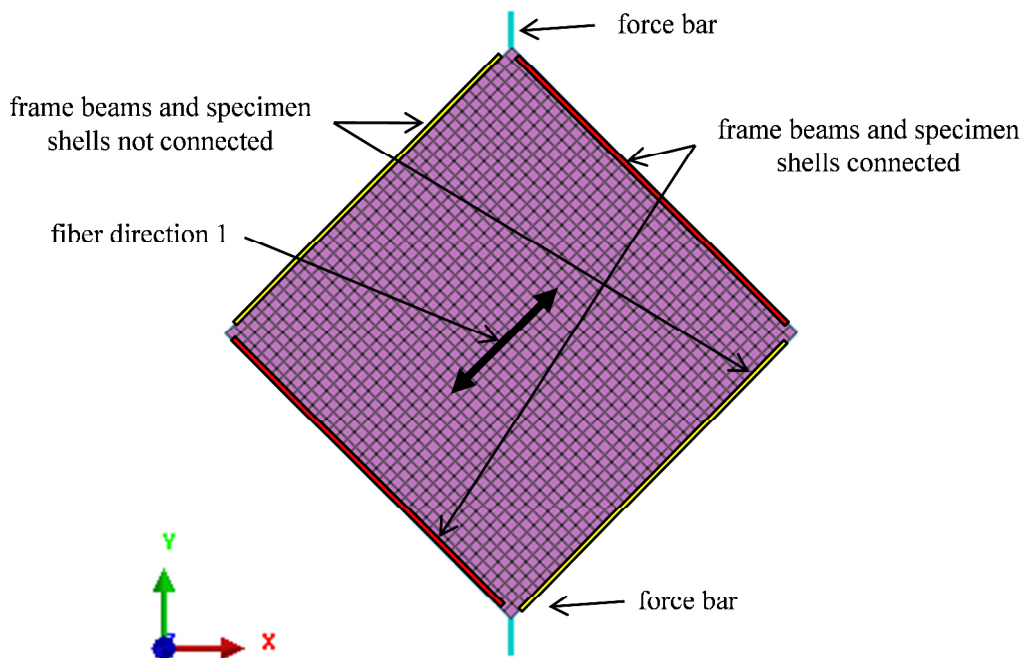


Fig. 5-16 Model setup of the PFT simulation

The specimen was modeled by a single shell layer and accounts for the whole 4-layers material setup. The 4-layers material setup had been chosen as it provided the most useful results in the tests (cf. subchapter 4.1.2). In the material card a viscosity of $\mu=0.001$ MPas was defined to additionally damp the PFT during the simulation. This value showed up to be large enough to ensure a noticeable damping and to be low enough not to influence the measured force [107]. The shells of the specimen were connected to the frame beams in longitudinal direction. In matrix direction the shell nodes were not connected to the frame. Any contact between specimen and frame was desisted.

In the PFT simulation it was important to use the uncoupled material model. Otherwise the fiber component of MAT140 would induce undesired shear forces (cf. 3.4).

The mesh size was chosen small enough to account for the wrinkles which also showed up in the experiment. In the present model the elements had size of 5 mm.

Initial input in the material card for the shear modulus was the experimental values. The shear modulus versus shear angle curve, as required in MAT140, was derived via the formulae given in 4.1.1. This curve is also shown in Fig. 5-20.

Simulation results

The simulation was able to model qualitatively the wrinkling of the specimen as in the experiment. Fig. 5-19 shows the comparison of the simulation with the experimental result which both had the wrinkles in the same direction. The tearing of the specimen was not possible to model, as PAM-FORM does not allow any element separation.

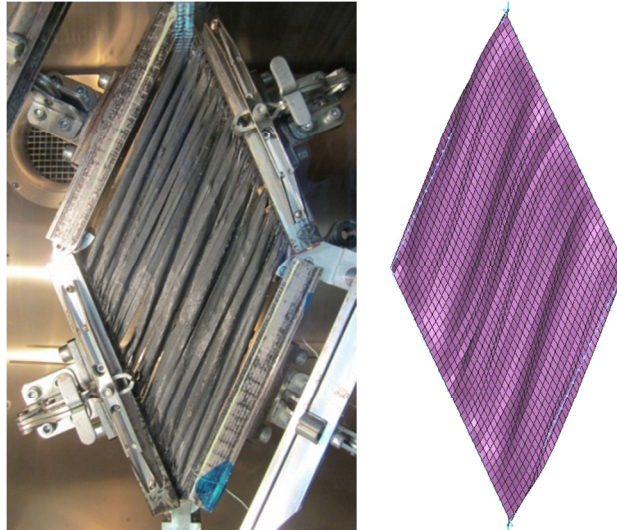


Fig. 5-17 Comparison of PFT experiment (4-layers material setup) and the simulation (both at 40° shear angle)

Nonetheless, the tearing can be predicted in the simulation by looking at the matrix strain and shear angle output. Fig. 5-18 shows both values plotted at a shear angle of 40°. The matrix strain reaches values of up to 15 % strain. By revising the results from the tensile test, the material showed a maximum strain of 10 % before tearing started (cf. 4.4.2). Hence, the high strain in the simulation is one indicator for tearing of the specimen. Another indicator is the high shear angles which can be also interpreted as tearing of the material. Within the experiment the tows slip relative to each other after they had torn apart (Fig. 2-5). Even though this slippage cannot be modeled by the macroscopic approach, it is still indicated by the high shear angles in the simulation.

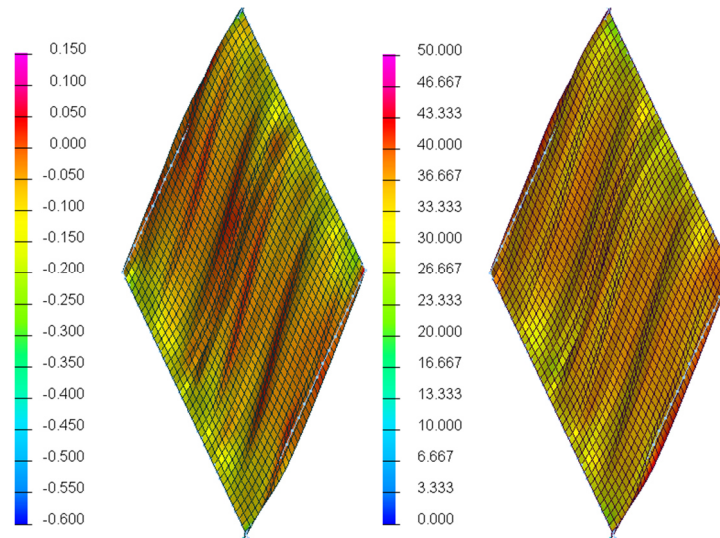


Fig. 5-18 PFT simulation results at 40° frame shear angle
Plot of matrix strain (left); plot of shear angle (right)

Although the simulation showed good results with respect to wrinkle formation and the indication of ruptures, the measured force response was too high. By comparing the machine force, the simulation followed qualitatively the experimental curve until ~ 20 mm displacement ($\cong 8.4^\circ$ shear angle). Afterwards the force started to rise exponentially (Fig. 5-19).

With a corrected shear modulus curve, it was possible to match the experimental curve until a displacement of ~ 50 mm ($\cong 22.6^\circ$ shear angle). A further following of the experimental curve was not possible because MAT140 starts to lock at shear angles higher than $\sim 25^\circ$. Counteracting this exponential rising of the force cannot be done even by defining zero shear stiffness at that phase.

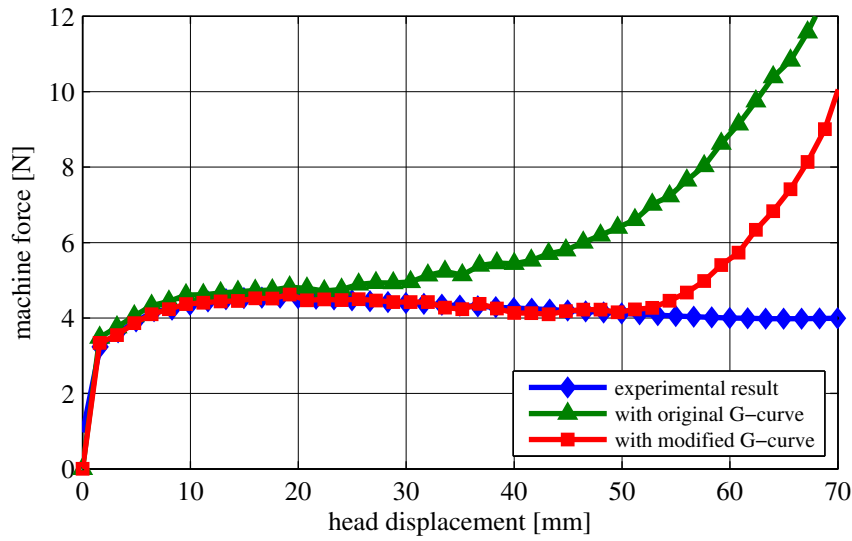


Fig. 5-19 Comparison of the PFT simulations with the experiment

The initial and corrected shear stiffness curves are plotted in Fig. 5-20. The curves are plotted as $G*\cos(\Phi)$ versus $\cos(\Phi)$ like required in MAT140. Instead of the shear angle γ the frame angle Φ is used here which is defined as:

$$\phi = \frac{\pi}{2} - \gamma \tag{5-3}$$

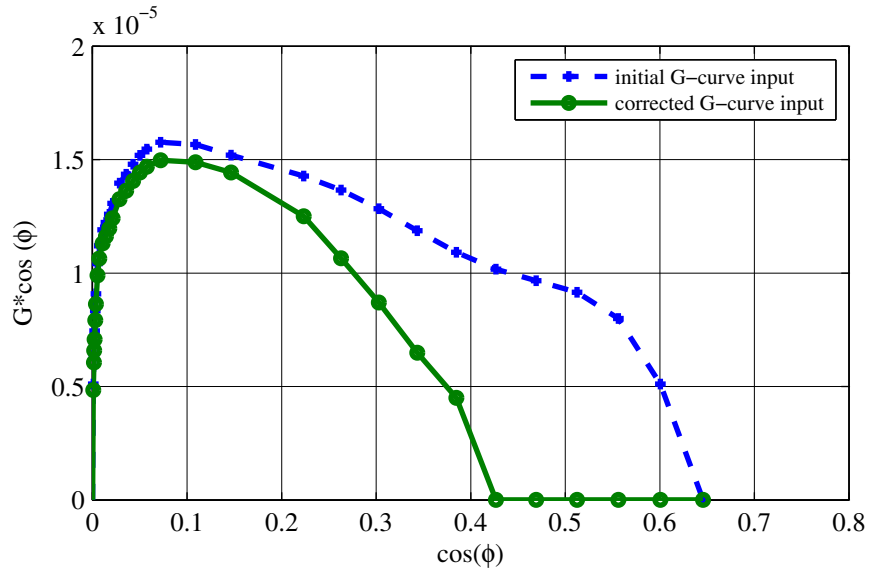


Fig. 5-20 Initial and corrected shear stiffness curves for the material model MAT140

The final shear stiffness curve $G(\gamma)$ was derived by adding a correction function on the original formula (4-5):

$$G(\gamma) = \frac{\tau(\gamma)}{\tan \gamma} * f_{red} + \sum_{i=1}^3 - \left[\left| \frac{\gamma}{\alpha_{cor_i}} - 1 \right| + \left(\frac{\gamma}{\alpha_{cor_i}} - 1 \right) \right] * \left(\frac{\tau(\gamma) * f_{red} * x_{cor_i}}{\tan \gamma} \right) \quad (5-4)$$

The correction function includes the reduction factor f_{red} to lower the total force and three correction factors x_{cor_i} acting at three shear angles α_{cor_i} . For the above mentioned shear curves these factors are:

$f_{red} =$	0.95
$\alpha_{cor_1} =$	0.162 rad (9.3°)
$x_{cor_1} =$	0.1
$\alpha_{cor_2} =$	0.227 rad (13.0°)
$x_{cor_1} =$	0.15
$\alpha_{cor_3} =$	0.307 rad (17.6°)
$x_{cor_1} =$	0.1

With the corrected shear behavior the simulation still had the same wrinkling and strain behavior as shown in Fig. 5-18.

5.5 Final material card

In this subchapter all material parameters from the foregoing material characterization simulations which are required for the material card MAT140 are summarized. Fig. 5-21 shows the resulted final material card for the AFP material which will be used in the subsequent draping simulations of this work.

```

$---5---10---5---20---5---30---5---40---5---50---5---60---5---70---5---80
$#          IDMAT   MATYP          RHO   ISINT   ISHG   ISTRAT   IFROZ
MATER /          2     140          1.193E-6   0       0
$# BLANK
$#          QVM   THDID   IDMPD
$#          1.       0
$#          TITLE
NAME AFP
$#          BLANK   BLANK   HGM   HGW   HGQ   As
$#          E1          Fb1   Fs1   ALPHA1   B1
$#          20.          STIF_CONST   1E-5   90.1.72688
$#          E2   LC2   Fb2   Fs2RFLAG   Alpha2   B2
$#          CURVE   1STIF_CONST   1E-5   1   0.0.0007193
$#          G   LCS   NUEp   ALPHlock   G_lock   Fbm   Fsm   SRFIL
$#          CURVE   2   0.3
$#          Eta
$#          Ro   B   n   thk_elim   thk_mult   thk_cut
$#          a0   b0   w0   phi   Iunc   ZHI   f
$#          1   0.5   0.
$#          LC1
$#          0

```

Fig. 5-21 Material card MAT140 with parameters for the AFP material

The definitions of the Young's modulus curve in E2-direction and the shear modulus curve are listed in Tab. A-1 and Tab. A-2. Since the friction values of the measurements can be directly implemented in the simulation model without any modifications (cf. 5.1), the definitions of the friction coefficients are not given here.

5.6 Conclusion

This chapter demonstrated the importance of applying a reverse approach on the material characterization tests. With modeling and simulation of the different material tests the behavior of the material model MAT140 was better understood and led to an enhanced usage of it. In this work all material characterization tests which had been carried out previously were likewise simulated.

The friction test simulations revealed a very robust contact modeling within PAMFORM. The friction coefficients which were initially defined in the contact model were also measured in the simulation results. Any modifications of the measured friction coefficients were therefore not required.

The simulations of the tensile test in matrix direction showed a good correlation with respect to the strain distribution in the specimen. Local areas in the simulation with strains above 10% indicated well the origination of ruptures. However, the comparison of the measured tensile forces revealed a too stiff behavior of the material model. Only by adjusting the Young's modulus curve allowed to ensure a correct behavior in tensile direction. The tensile behavior was controlled in this way until a logarithmic strain of about 0.15. At higher strain states the material started to lock and consequently led to tension stiffening. Nevertheless, for modeling the AFP material this limitation is still acceptable, since the material has a maximum logarithmic strain of 0.1 after which

rupture starts. The material model is therefore able to simulate the tensile behavior of AFP material until rupture.

The bending test was difficult to model in the simulation. The long overhanging length of the specimen lead to oscillations at the tip and needed to be counteracted by applying the gravity load continuously and defining additionally a damping in the specimen. Nonetheless, the bending behavior was well modeled in the simulation. In the simulation of the 90°-test the bending behavior needed to be modified by a factor of 0.935 and in the 0°-test by a factor of 1.005. A clear trend of a too stiff or too soft bending behavior was not found. This highlights again the importance of performing the reverse approach on the bending tests. Hence, for future bending tests the simulation is a mandatory step to derive the bending stiffness for the material model.

The PFT simulation was able to reflect the wrinkling behavior of the specimen like in the experiment. The rupture of the specimen at high shear strains was indicated in the simulation by a summation of locally high matrix strains and high shear angles. But the comparison of the traction force (machine force) revealed a too stiff behavior of the material model. It was possible to adjust the shear behavior of the material model to properly fit it to the experiment until a shear angle of 22°. At higher shear angles the material model started to lock and could not be controlled anymore. The measured force then rose exponentially at this point.

To evaluate the derived material parameters the next chapter will apply a validation on the final material model. Especially the interdependency of the different parameters will be checked in forming simulations on generic geometries.

6 Validation

The validation of the material model is a mandatory step in draping simulations before applying it to real applications. None of the currently available material models is able to account for every deformation mechanism and defect taking place during forming. With the validation the material model is checked in this regard and also shows its limitations. Furthermore, the validation proofs the correctness of the material parameters which had been determined in the simulations of the material characterization tests.

In the following chapter a complete validation procedure of MAT140 for AFP materials will be presented. It involves an appropriate forming experiment, the according simulation and method for comparing both.

In the beginning, the forming experiments which had been performed in this work will be presented. A stamp forming process had been developed which allows the forming of the AFP material on two different generic geometries. The forming process was developed in a way to enable the forming of the material at elevated temperatures.

Subsequently, the simulation of this forming process will be introduced. It includes the modeling, the meshing and the definition of the BCs. The material parameters of chapter 1 will be used here.

In the third part, the method will be presented which was used to compare quantitatively the simulation results with the experimental results. It involves a measurement method by using an optical sensor, which measures the fiber orientation at different locations of the preform. Furthermore, a MATLAB routine is presented which imports the simulation results and the sensor data to compare them with each other. This method allowed a quantitative validation of the simulation.

Finally, the whole validation process will be applied on a hemispherical tool and the Double Sine tool. Forming experiments will be carried out, its simulations and their comparison with each other. The simulations will be quantitatively validated in terms of the fiber direction and qualitatively by wrinkling behavior and the draw-in.

6.1 Experiments

For validating the simulation model a suitable forming experiment is required. It has to include an appropriate geometry to be draped on and a forming process which ensures a repeatable output. Both had been chosen with respect to the forming behavior of the AFP material and the PAM-FORM material model. Another prerequisite was to be able to carry out all forming experiments on a laboratory scale.

6.1.1 Geometries

The geometry on which the forming validation is done requires a 3D shape. Only if a ply is formed over a double curved surface most of the deformation modes of the AFP material occur. In this work two geometries had been used for validation. First geometry was a hemisphere with a radius of 63.5 mm. Its shape forces the material to undergo large deformations and even leads to draping defects. These defects are desired in order to check whether the simulation model is able to model these defects or not. The second geometry was the so called Double Sine tool. It consisted of two intersecting sinusoidal waves with a wave length of 2π and a $1/2$ amplitude. This geometry applied lower deformation grades on the material than the hemisphere tooling. It allowed an almost defect-free forming of the AFP material in a 3D shape. Fig. 6-1 shows both geometries which had been used in this work.

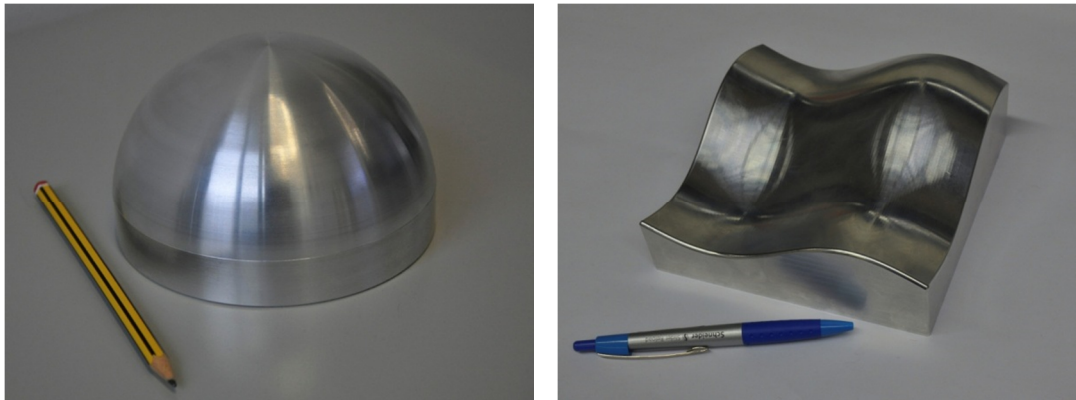


Fig. 6-1 Validation geometries
Hemisphere tool (left); Double Sine tool (right)

6.1.2 Forming process

For validating the simulation results the forming process required to be robust and repeatable. In this work the stamping process (match mold forming) was used as it fitted the requirements best. The stamping process consisted of a movable upper tool (punch) and a fixed lower tool (die). Between the tools a single ply or a ply stack was positioned (Fig. 6-2). By closing the tooling the plies were formed into the desired 3D shape. Additionally a blankholder was attached to the upper tool which moved independently from the tooling. Prior to the upper tooling the blankholder was lowered on the plies and applied a certain in-plane tension on the plies. This reduced the formation of wrinkles and led to a better draping result.

The stamping device was installed in tensile testing machine. It allowed an exact controlling of the forming velocity and the tool displacement. In addition, the whole tooling was encased in a thermal chamber to ensure the forming at 65.5°C . At this temperature the material characterization tests and flange forming experiments (chapter 1) had been carried out.

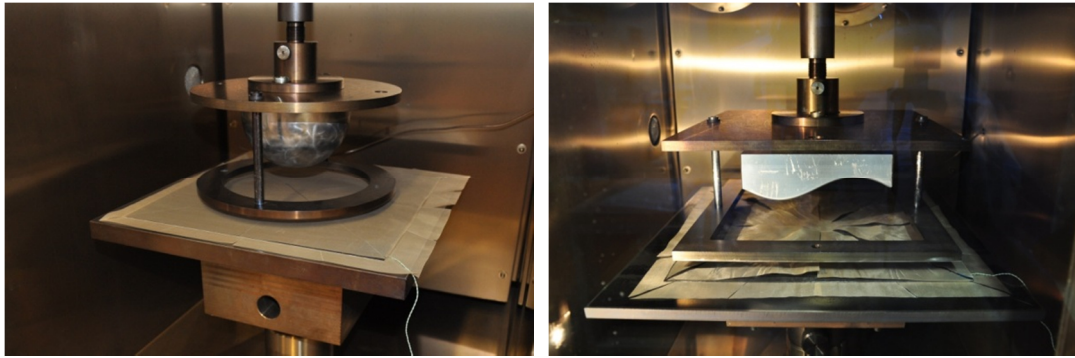


Fig. 6-2 Stamping process
Hemisphere tooling (left); Double Sine tooling (right)

For each forming experiment the plies were wrapped between two sheets of Teflon foil. They ensured low frictional forces and consequently an easier sliding on the tooling. To avoid any negative influence of the foils on the draping behavior of the AFP plies, radial cuts were inserted in the foils for an easier forming.

6.2 Simulation

The simulation of the validation experiments required to model all relevant parts of the tooling. Besides the upper and lower tool also the blankholder was included. All tools and the blankholder were modeled with shell elements and defined as rigid bodies. The lower tool was fixed in its position while the upper tool and the blankholder moved according to a predefined displacement BC. Contact definitions with the according friction coefficients were defined for every touching pairs. The plies were modeled with 4-node shell elements with one layer of shells for each single ply. The material parameters from chapter 1 were used.

A crucial point in the model setup was the meshing of the plies. As mentioned in subchapter 3.4 the mesh needs to be aligned in fiber direction otherwise shear/tension locking effects can evolve. If the mesh is not aligned spurious tension occurs if pure shear deformation is applied [69, 73, 87, 88, 108]. Especially at high deformation grades the standard FE interpolation schemes are not compatible with the physics of the textile and lead to a too stiff material behavior. Therefore an aligned mesh in forming simulations is generally recommended.

6.3 Comparison method

The comparison of the simulation results and the experimental results were done with a MATLAB routine programmed by Schug [109]. It allows importing the simulation results and the data measured in the experiments. Both were plotted on each other and the differences of the fiber directions are calculated (Fig. 6-3).

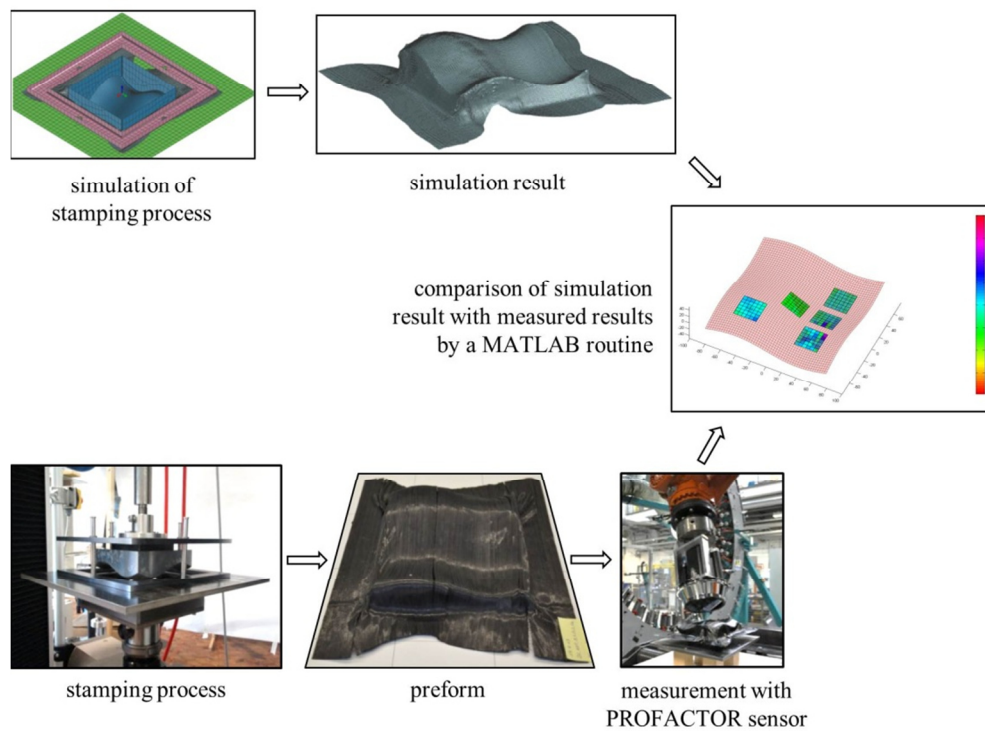


Fig. 6-3 Principle of the validation process using a MATLAB routine

Here, measurement method and the MATLAB routine will be introduced. For measuring the fiber direction in the preforms an optical sensor was used. The MATLAB routine and the underlying algorithm are briefly explained. For a detail description one has to consult the diploma thesis of Schug [109].

6.3.1 Measurement method

To provide a quantitative comparison of the simulation with the experiment, the fiber direction of the top ply in the preform was measured. The measurement was done by using an optical fiber angle sensor from PROFACTOR GmbH (Fig. 6-4) [110, 111]. This sensor allows measuring the fiber direction with an accuracy of $\pm 1^\circ$. The sensor is built up of a 5 megapixel camera and light ring with 96 LEDs which illuminates the examined ply in different angles. Within one cycle the sensor takes 8 different illuminated images all are having different reflecting lights. Assuming the fibers to have a perfect cylindrical shape their orientation is calculated by analyzing the reflection behavior in the 8 images (Fig. 6-4). This method provides the information of the fiber direction for every pixel. In this work a configuration of 1600 pixel x 1600 pixel was used which provided a resolution of 0.035 mm per pixel for a field of view of 56 mm x 56 mm.

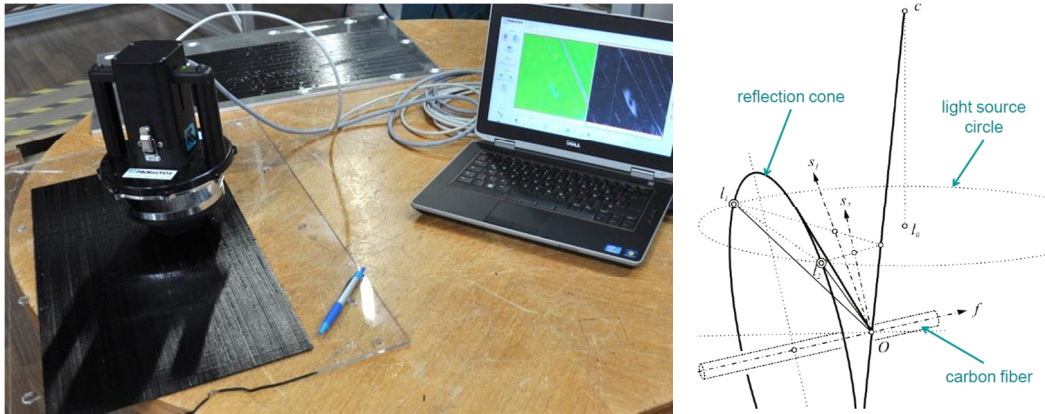


Fig. 6-4 Measurement using the PROFACTOR fiber angle sensor
Live measurement of an AFP ply (left); light reflections of a cylindrical fiber (right).

The PROFACTOR sensor is controlled by the software FScan. It allows live measurements with the sensor and directly provides the measured fiber alignment. Furthermore, the software processes the data and additionally shows the out-of-plane angle of the fibers as well as the diffuse and the specular fraction of each pixel. The provided output can be exported in a MATLAB file for further processing by the user.

The sensor can be handled manually and placed on the desired measurement location. But in this work the sensor was handled by a robot and driven to different positions on the preforms (Fig. 6-5). This ensured a repeatable positioning of the sensor at predefined locations. For measurement a program was generated that moved the robot sequentially to defined positions on the hemisphere and the Double Sine tools.

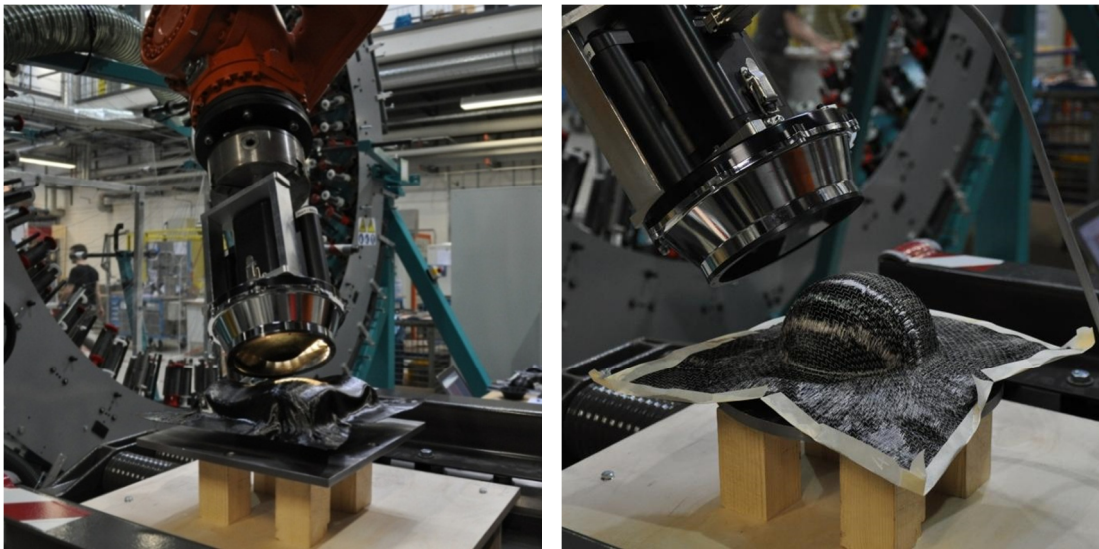


Fig. 6-5 Fiber direction measurements with the PROFACTOR sensor positioned by a robot
UD prepreg measurement on the Double Sine tool (left); biaxial NCF measurement on the hemisphere tool (right)

6.3.2 MATLAB routine

The MATLAB routine imports ASCII files from the simulation and the MATLAB files from the sensor measurements. The ASCII files need to include the node coordinates, the related shell elements as well as the x-, y- and z-fractions of the unit vector in fiber direction 1 of the top ply. The MATLAB files are needed for every measured location and should at least contain the in-plane fiber directions. The user can import the files via a graphical user interface (GUI) in the MATLAB routine (Fig. 6-6).

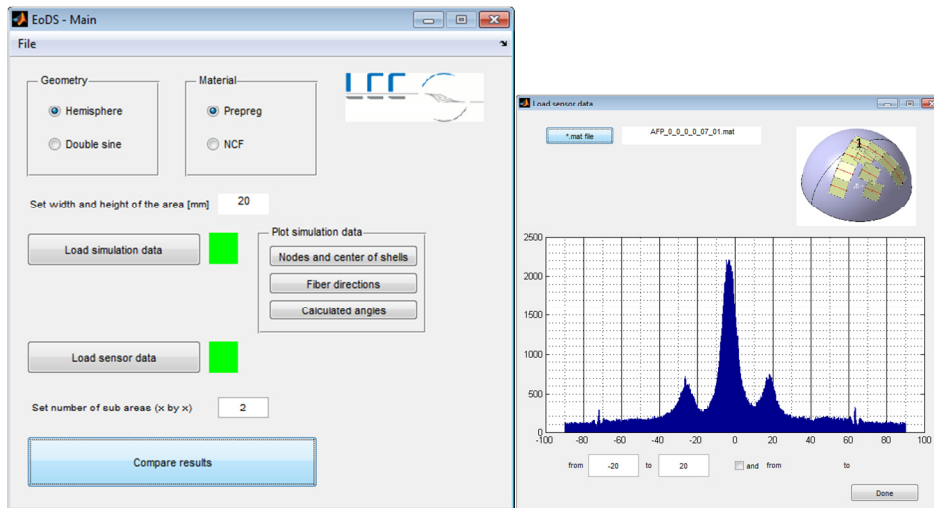


Fig. 6-6 GUI of the MATLAB routine
Main window (left); data selection window (right)

To import the single MATLAB files a separate window is provided. It shows a histogram plot of the fiber alignment of the whole measured area. The user needs to define a threshold in which the desired fiber alignment lies. This has to be done because the measurement can include some scanned fibers which belong to an underlying ply.

The ASCII files from the simulation are loaded without any modification in the MATLAB routine. To check the correctness of the loaded files the routine offers to plot the node coordinates the shear angles and the fiber direction vectors of every element. Fig. 6-7 shows these three 3D-plots from the imported simulation data.

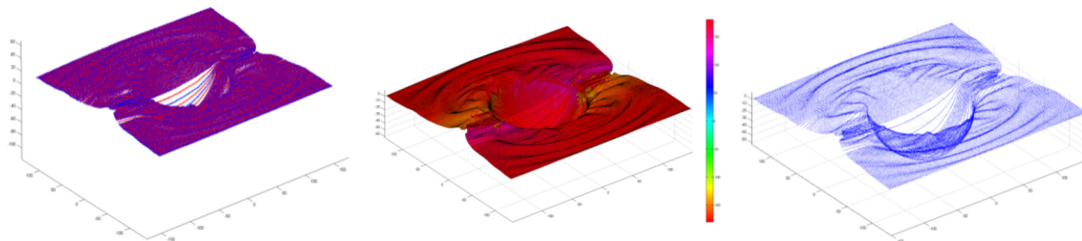


Fig. 6-7 Imported simulation data in the MATLAB routine
Plot of nodes (left), plot of shear angles (center); plot of vectors in fiber direction (right)

When all data are imported the routine first computes the midpoint of each shell element. Every midpoint is then assigned with the fiber direction from the unit vector. Afterwards a search algorithm scans all midpoints for those which lie in the scanned areas of the PROFACTOR measurements. Finally, the routine computes the deviation between the fiber directions of the simulation with the fiber directions of the measurement at every matching position. This computation is either done for the average fiber direction in the whole scanned area or it can be divided into subareas for a more detailed examination.

The MATLAB routine includes the analysis of the hemisphere tool and the Double Sine tool as describe in subchapter 6.1.1. It investigates 10 different locations for the hemisphere and 5 different locations for the Double Sine (Fig. 6-8). All computed deviations are provided in a 3D plot and colored according to their value of deviation.

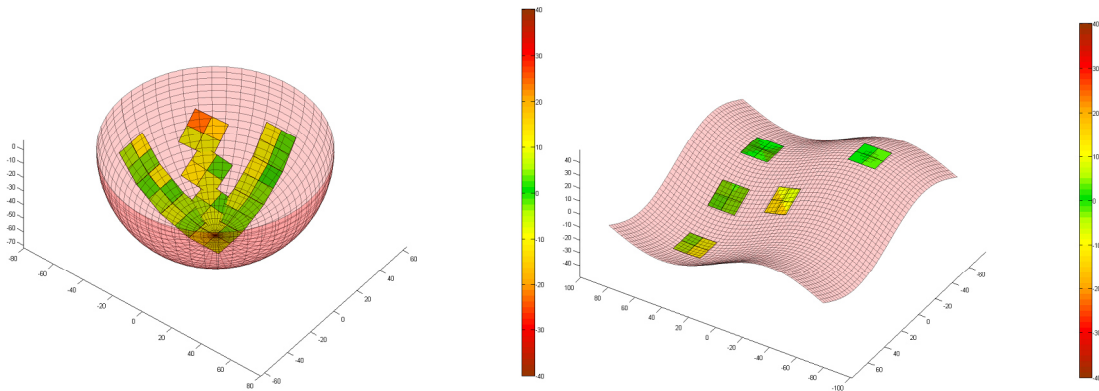


Fig. 6-8 Comparison of the simulation result and the fiber alignment from the experiment Hemisphere (left); Double Sine (right); both with four subareas for every measurement

Besides the 3D plot the routine prints the precise values of the fiber alignment. Fig. 6-9 shows an example print out for the hemisphere. The print out provides the angular deviation with respect to the projected global y-axis of the tools.

```

*****
***** RESULTS *****
*****

Mean of the whole measuring area

          Sensor      Simulation
Measuring area 1 :  -3.2435      0.0029
Measuring area 2 :  -2.7040     -0.3799
Measuring area 3 :  -3.7796     -0.6130
Measuring area 4 :  -3.9631     -0.5564
Measuring area 5 :  -2.6268      0.2786
Measuring area 6 :  -2.5763      0.5517
Measuring area 7 :  -1.4006     -0.5861
Measuring area 8 :  -2.5058      1.0672
Measuring area 9 :  -1.0331      4.4301
Measuring area 10:   0.1261     14.1699

*****
>>

```

Fig. 6-9 Exemplary print out from the MATLAB routine for the hemisphere

6.4 Validation with the hemisphere

This subchapter presents the forming experiments on the hemisphere, its simulation and their comparison. First, the forming experiment is presented by describing the process parameters and conditions as well as the produced preforms. Last, the comparison between simulation and experiment is made by visual inspection and by use of the PROFACTOR measurements and the MATLAB routine.

6.4.1 Experiment

The stamp forming of the hemisphere was done with the 4-layer material layup (0/0/0/0) manufactured by the AFP machine. Other material layups like e.g. the 0/90 layup were not stable enough and felt apart during forming. The laminate dimension was 300 mm x 300 mm and was centric positioned on the female mold (Fig. 6-10). The specimen temperature was tracked by a thermocouple which was attached in a corner of the specimen. After heating up the specimen to 65° C / 150° F the tools closed with a velocity of 200 mm/min. First the blankholder got into contact with the specimen and subsequently the male mold formed the laminate.

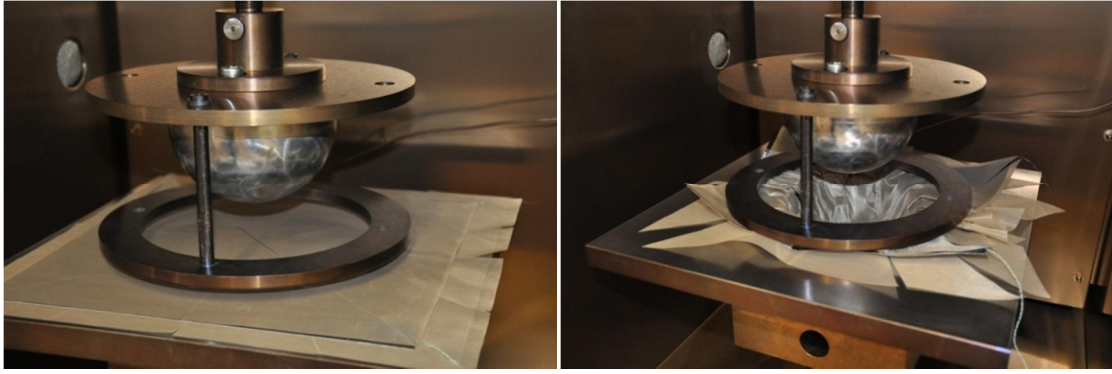


Fig. 6-10 Forming experiment of the hemisphere

The AFP material lies in between two layers of Teflon foil to reduce the friction on the tooling

Fig. 6-11 show three preforms from the hemisphere forming experiments. All preforms showed strong wrinkling at the sides in fiber direction. In addition, at some locations along the edges the material started to tear apart. This rupture indicates the stresses in matrix direction which acted during forming. Further tensile stress occurred on top of the hemisphere where it partially led to separation of adjacent tows. The tensile stress in fiber direction led to a draw-in of the material at the sides in fiber direction. All preforms showed qualitatively the same forming behavior but differed at locations where high deformations occurred.



Fig. 6-11 Top view of three preforms from the hemisphere forming experiments

6.4.2 Simulation

The simulation included the laminate with single shell layers for each ply, the male and female mold as well as the blank holder (Fig. 6-12). The forming sequence was defined according to the experiment by first moving the blankholder until it touches the laminate and afterwards moving the male mold to form the laminate. The blank-

holder moved by an applied gravity load according to its real weight and the male mold moved by a defined displacement BC.

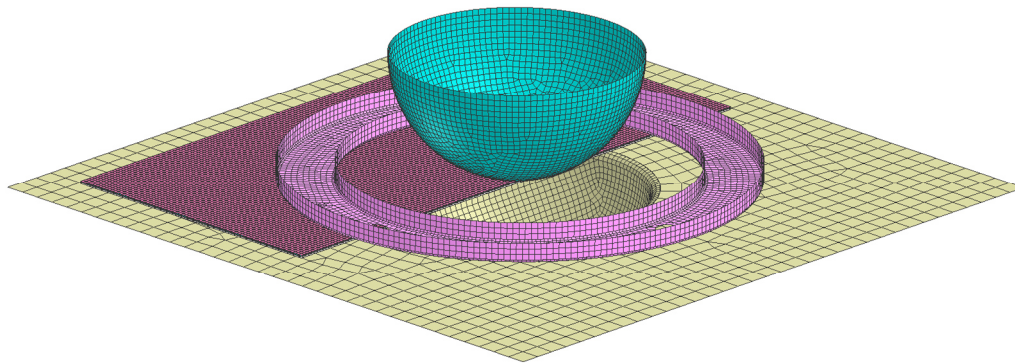


Fig. 6-12 Setup of hemisphere forming simulation
With a cut-section view of the laminate for a better visibility

The laminate mesh consisted of 2 mm x 2 mm shell elements and was aligned in fiber direction. A sliding contact (CNTAC 33) defined the coupling between the single shell layers. As described in subchapter 5.1 shell nodes which lay direct on top of each other can lead to undesired force peaks. To reduce the occurrence of force peaks the shell layers had been initially disarranged in the simulation model (Fig. 6-13). The initial normal distance between the shell layers was set to 0.5 mm to avoid any initial contact penetration.

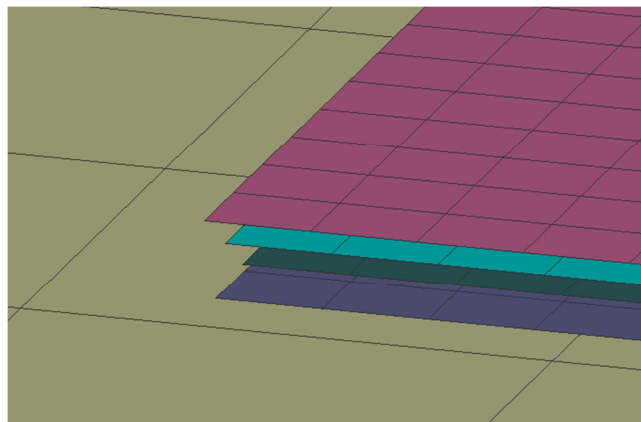


Fig. 6-13 Disarrangement of the shell layers to avoid nodes lying on top of each other

In first simulations difficulties showed up due to the small contact thickness (0.23 mm) of the shell layers. The accordingly high contact stiffness led to numerical instabilities and an abortion of the FE solver. It had been counteracted by adding a non-linear penalty factor (FSVNL) in the contact definition which ensured a more stable behavior.

The tackiness of the AFP material was modeled by defining a separation stress (SEP-STR) in the contact definition card. It defines the required stress to tear them apart two plies which are in contact with each other. A detailed description of the underlying mechanism was neither provided by the software manual nor by the technical support

of *ESI Group*. Throughout various simulations a value of $1.0e-2$ MPa found out to show the most realistic behavior and was used in the following simulations.

To keep the computational effort low the Teflon foils of the experiment were not included in the simulation model. Anyhow, their influence was taken into account in the friction definition. The friction coefficient between Teflon foil and tooling was defined on the laminate shells in the simulation. As the Teflon foils were darts in the experiment no other influence on the draping behavior besides the friction should occur.

6.4.3 Comparison

With the parameter set from chapter 1 the simulation did not showed the expected result (Fig. 6-14-Fig. 6-15). Although the lateral draw-in of the laminate looked alike the experimental preform the wrinkle formation was not satisfyingly modeled. In the experiment wrinkles evolved in the sides and developed until the hemisphere. The simulation did not showed any wrinkle at this location (Fig. 6-14).

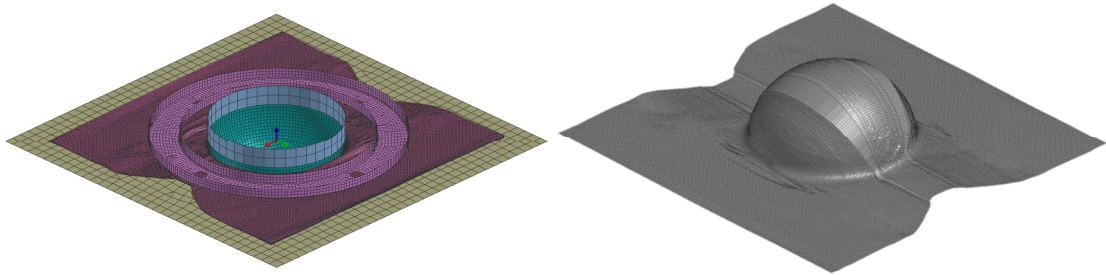


Fig. 6-14 Simulation of the hemisphere forming
Final forming state (left); formed top ply (right)



Fig. 6-15 AFP preform of the hemisphere forming experiment

The lack of wrinkles in the simulation indicated too low shear stiffness. Usually wrinkles occur due to a limitation of the shear deformation (cf. 2.1.1). In this case, the shell element underwent a high shear deformation by only low shear stresses. This effect

was proven by repeating the simulation with higher shear stiffness properties. Fig. 6-16 shows three simulation results with different shear stiffness. In comparison with the previous simulation only the shear stiffness had been altered by up scaling the shear modulus curve in the material model. The higher the shear stiffness the more wrinkles occurred. By just comparing the wrinkle formation, the simulation with the three times higher shear stiffness was most realistic. The one with the double shear stiffness showed a better behavior than the original one but did not fit perfectly. The one with five times higher shear stiffness showed too many wrinkles even at locations where no wrinkles showed up in the experiments.

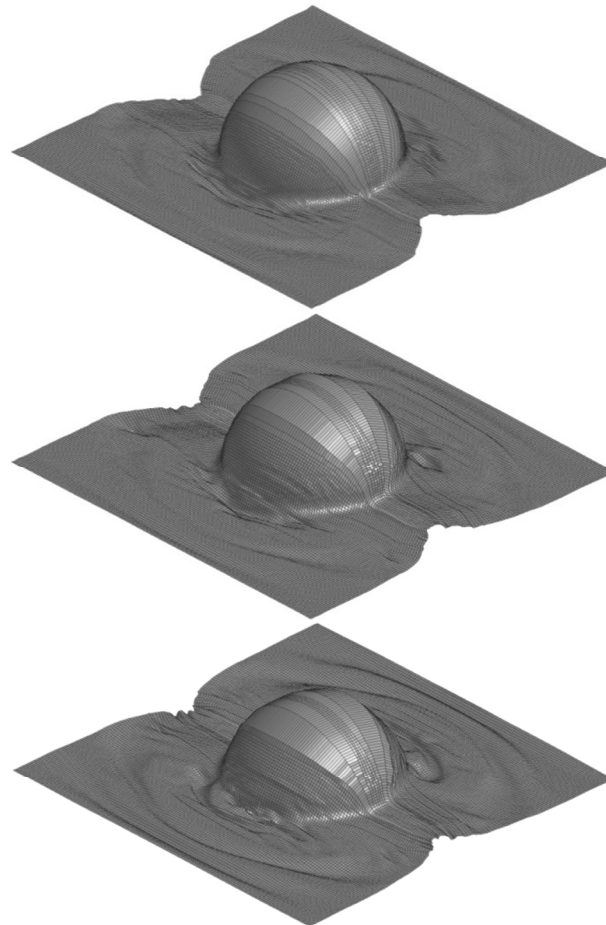


Fig. 6-16 Hemisphere forming simulations with different shear stiffness
2x G-curve (top), 3x G-curve (middle); 5x G-curve (bottom)

Fig. 6-17 shows the four different simulations but with contour plots of the logarithmic strain in matrix direction. As the macro scale modeling cannot account for the separation of adjacent tows the matrix strain can be used alternatively for indicating those locations. In the experiment the preform showed ruptures in the flanges and openings on the hemisphere (Fig. 6-11 and Fig. 6-15). All simulations had a high matrix strain on the hemisphere in common. Even though the predicted strain seems too high, the strain only occurred at single rows of elements. In the experiment the matrix strain and tow separation, respectively, was more evenly distributed on the hemisphere. This

cannot be modeled by the simulation as the main strain will be possessed by single element rows which already reached the strain to rupture.

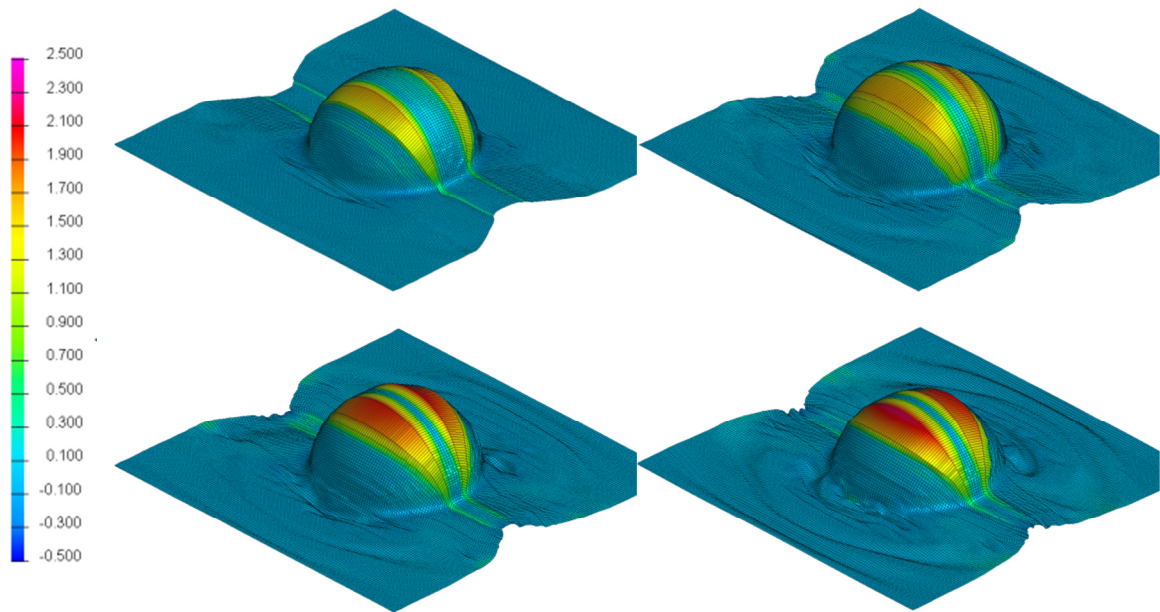


Fig. 6-17 Hemisphere simulations showing the strain in matrix direction
Standard G-curve (top left); 2x G-curve (top right); 3x G-curve (bottom left); 5x G-curve (bottom right)

Fig. 6-18 plots the shear angle distribution for the four simulations. In all simulations shear angles of more than 40° showed up. Those shear angles seemed too high compared to PFT testing in which shear angles of maximum $\sim 4^\circ$ were possible before the specimen started to wrinkle. But the shear angle maxima were located in areas where the specimen wrinkled (simulation and experiment). As described in subchapter 2.1.1, the shear of AFP plies is more an inter-tow shear rather than an intra-tow shear (Fig. 2-5). But regarding the four simulations no qualitative statement can be given as the inter-tow shear and the geometries of the wrinkles cannot be directly measured in the experiment.

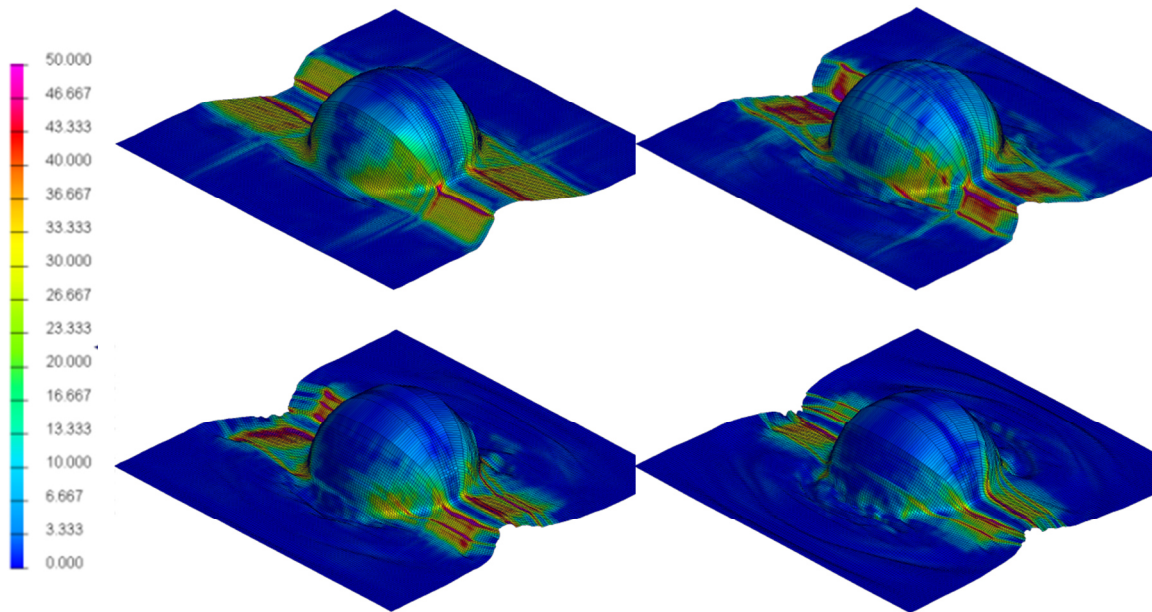


Fig. 6-18 Hemisphere simulations showing the shear angle distribution
 Standard G-curve (top left); 2x G-curve (top right); 3x G-curve (bottom left); 5x G-curve (bottom right)

The comparison with the MATLAB routine was done at 10 specific points located in 0° , 45° and 90° with respect to the fiber direction and on a polar angle of 0° , 18° , 36° and 54° (Fig. 6-19). They had been chosen to cover most of the preform and to be able to measure without any collision of the sensor with the preform or the tooling.

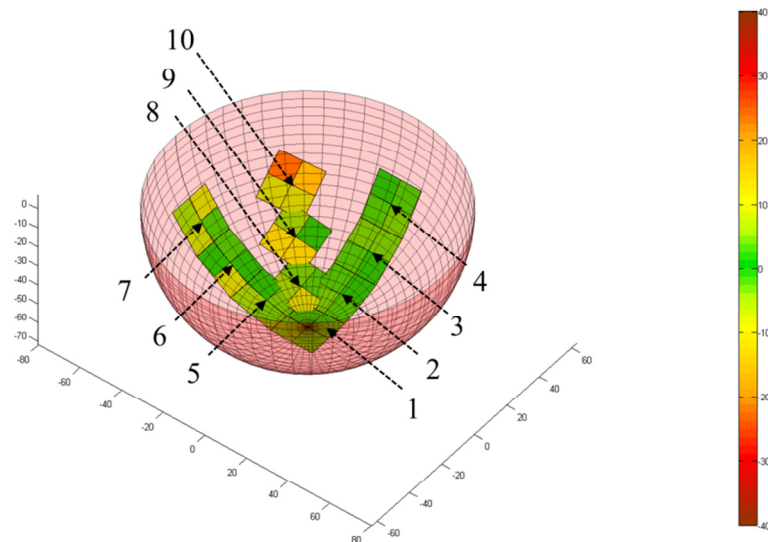


Fig. 6-19 Comparison plot of hemisphere simulation with the numbering of the ten measurement areas

The comparison was made with the simulation of the unmodified G-curve and the one with the double shear stiffness. Regarding the color plot in Fig. 6-19, the simulation showed a good agreement to the experiment. Only at measurement area 10 a higher

deviation was detected. This was mainly due to wrinkles in the preform at this location. The simulation does not show any wrinkle at this area and consequently has a high deviation (Fig. 6-20).

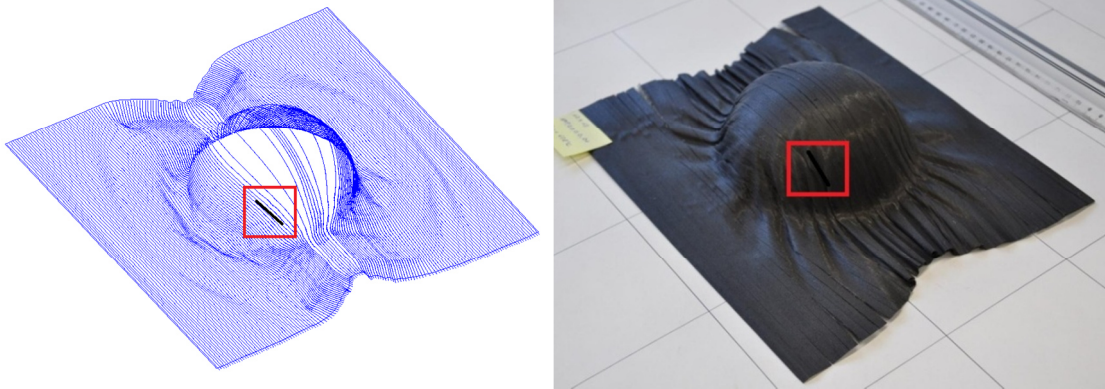


Fig. 6-20 Comparison of fiber direction at measurement area 10

Plot of fiber direction 1 in the simulation with the unmodified shear stiffness (left); experimental result (right)

The values of the fiber direction with respect to the global y-axis are quoted in Tab. 6-1. The experimental values are the averages from three different preforms. In fiber and perpendicular direction (areas 1-7) the simulations differs less than 1.8° and 1.4° from the experiment. The simulation with the double shear stiffness properties was closer to the experiment in most of the areas. In 45° -direction (areas 8 - 10) the deviation increased in both simulations the farther the measurement was taken from the hemisphere pole. Again, the simulation with the double shear stiffness provided better results than the simulation with the unmodified shear stiffness.

Tab. 6-1 Deviation of fiber direction with respect to the projected y-axis for the hemisphere simulations (standard shear stiffness and double shear stiffness) and the experiments

area	experiment average [$^\circ$]	standard G-curve (abs. deviation) [$^\circ$]	2x G-curve (abs. deviation) [$^\circ$]
1	-1.8	0.0 (1.8)	-0.5 (1.3)
2	-1.6	-0.4 (1.2)	-0.3 (1.3)
3	-2.0	-0.6 (1.4)	0.2 (1.4)
4	-1.7	-0.6 (1.1)	0.6 (1.1)
5	-1.2	0.3 (1.5)	-0.4 (0.8)
6	-0.8	0.6 (1.4)	-0.6 (0.2)
7	-0.6	-0.6 (1.2)	-1.5 (0.9)

8	-1.9	1.1 (3.0)	0.9 (2.0)
9	-1.9	4.4 (6.3)	3.1 (5.0)
10	-1.4	14.2 (15.6)	10.3 (11.7)

The predicted fiber directions of both simulations in areas 1 – 7 are sufficiently good. But it has to be mentioned that the results could be even better. The values from the experiments in areas 1 – 7 showed angles of up to 2°. Theoretically the angles should be zero here. These deviations could come from the measurement. Since the hemisphere is rotary symmetric the preform might not have been correctly positioned on the tool during measurement (Fig. 6-5).

6.5 Validation with the Double Sine

Likewise the previous subchapter, the experimental forming and simulation of the Double Sine geometry will be presented here. In contrast to the hemisphere geometry, the Double Sine geometry has smoother curvatures and lead to fewer defects when draping AFP laminates. Furthermore, a second geometry can proof the findings of previous simulations on the hemisphere.

6.5.1 Experiment

The forming experiments on the Double Sine geometry was done with the same material layup (0/0/0/0) as in the hemisphere forming. The laminate dimension (300 mm x 300 mm) and the process conditions ($T = 65^\circ \text{C}$; $v = 200 \text{ mm/min}$) were defined accordingly. Fig. 6-21 shows a forming trial on the Double Sine at its initial position and its final position.

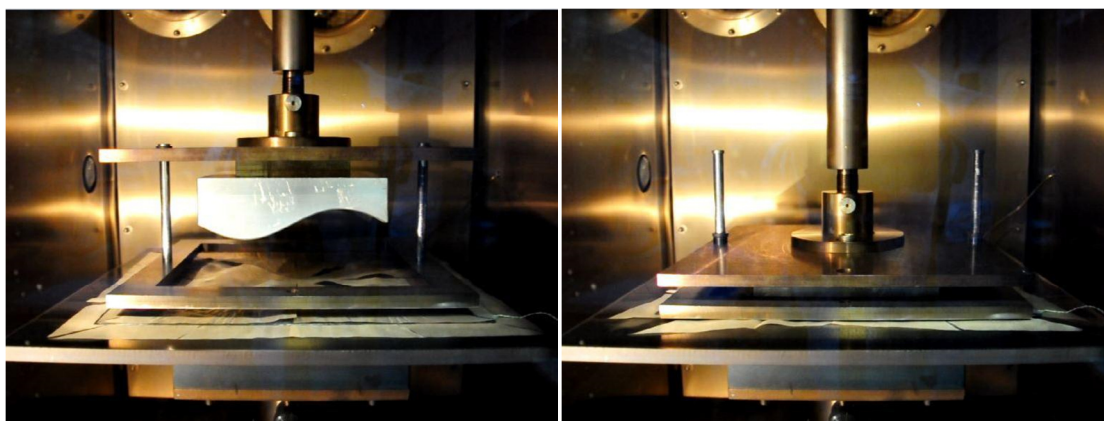


Fig. 6-21 Forming experiment of the Double Sine geometry

The final preforms of the Double Sine are shown in Fig. 6-22. In contrast to the hemisphere preforms these preforms had fewer wrinkles. Wrinkles and folds only occur at the edges of the tool and propagate towards the laminate edges. At the edges the tensile

stresses tore the laminate apart and led to cuts. It also led to a single tow gap on top of the Double Sine. In addition, the laminate draw-ins at the edges were again qualitatively the same.



Fig. 6-22 Top view of three preforms from the Double Sine forming experiments

6.5.2 Simulation

The simulation model of the Double Sine forming consisted of four shell layers for the laminate, the blankholder, the male mold, and female mold (Fig. 6-23). The meshing and the BCs were defined according to the hemisphere simulation. To check again the influence of higher shear stiffness, the Double Sine simulation was also carried out with different shear stiffness properties.

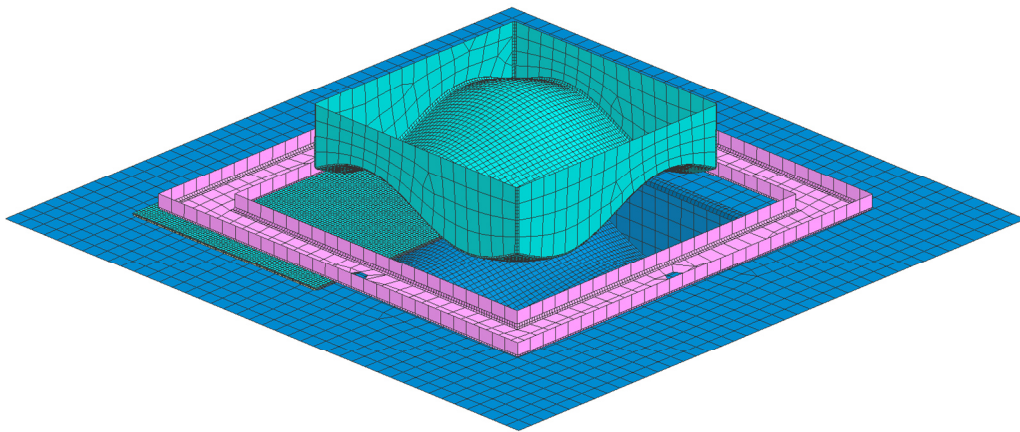


Fig. 6-23 Setup of Double Sine forming simulation
With a cut-section view of the laminate for a better visibility

6.5.3 Comparison

Using the unmodified material parameter set, the Double Sine simulation offered a better accordance to the experiments rather than the hemisphere simulation (Fig. 6-24 and Fig. 6-25). Main reason was the lower deformation grades in the formed part. On the top face of the Double Sine mainly stresses in matrix direction occurred which

were also shown in the simulation. The wrinkles at the edges of the Double Sine were also present in the simulation. Moreover, the draw-in of the edges in fiber direction showed the same characteristic shape as in the experimental preform. But the simulation showed a draw-in of the laminate in cross direction, where no draw-in in the experiment occurred.

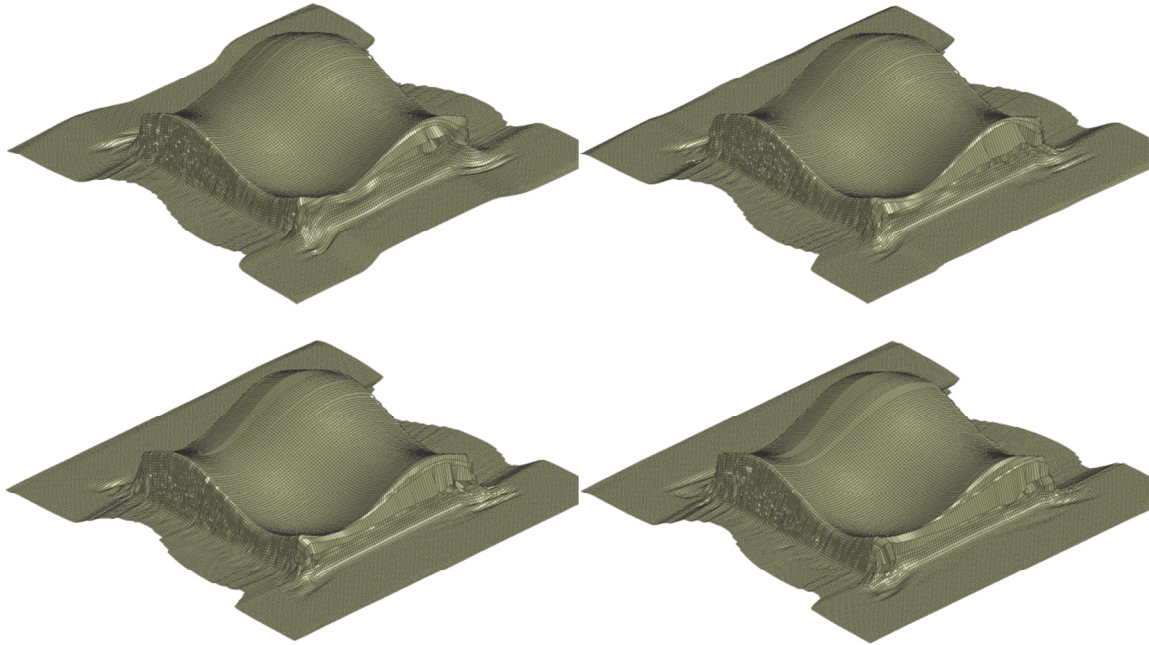


Fig. 6-24 Double Sine forming simulations with different shear stiffness
Standard G-curve (top left); 2x G-curve (top right); 3x G-curve (bottom left); 5x G-curve (bottom right)



Fig. 6-25 AFP preform of the Double Sine forming experiment

The simulation results with the different shear stiffness showed less difference as in the hemisphere simulations. Regarding the wrinkling behavior the simulations looked almost similar (Fig. 6-24). Main difference showed up to be the strain in matrix direction. The strain on the top surface and at the flanks increased with higher shear stiffness (Fig. 6-26). In return, the draw-in at the cross sides vanished with the higher shear stiffness.

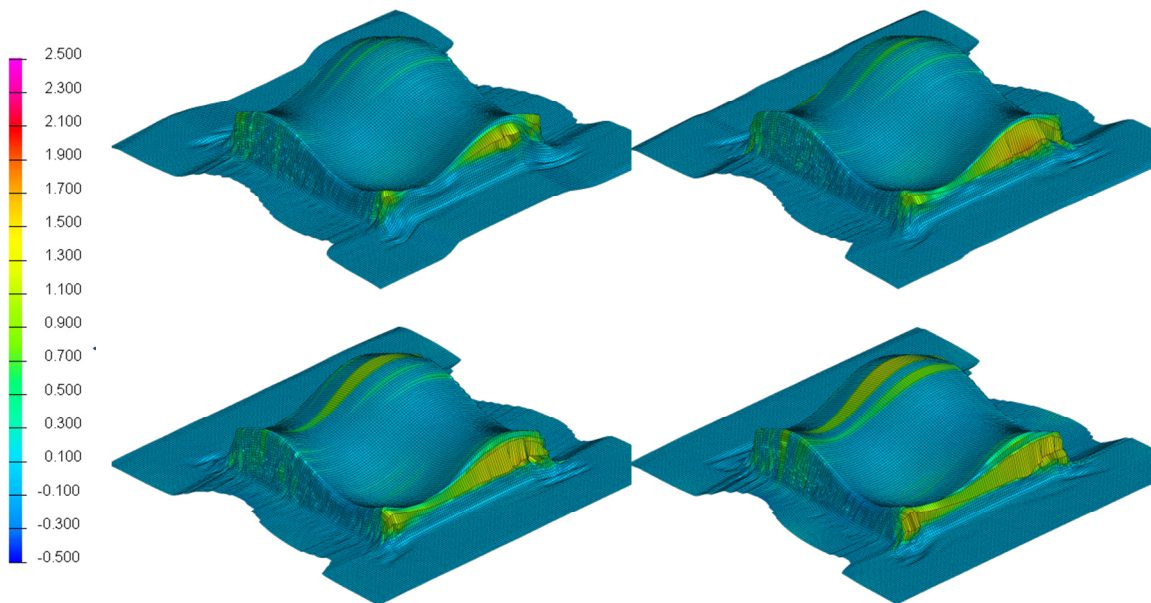


Fig. 6-26 Double Sine simulations showing E2-strain

Standard G-curve (top left); 2x G-curve (top right); 3x G-curve (bottom left); 5x G-curve (bottom right)

Likewise in the hemisphere simulation the best accordance with the experimental results was provided in the simulation with the double shear stiffness. Although the strain at the flank was too large, the draw-in at the cross sides was more realistic as in the standard simulation. The strain on top of the Double Sine was more realistic as well. The simulation with the three and five times increased stiffness showed a too large matrix strain on the Double Sine top face.

Fig. 6-27 shows the shear angles for all simulations. No major differences were detected here. All simulations show the highest shear angles in the areas where the wrinkles occurred. This approves the behavior which was already seen in the hemisphere simulations.

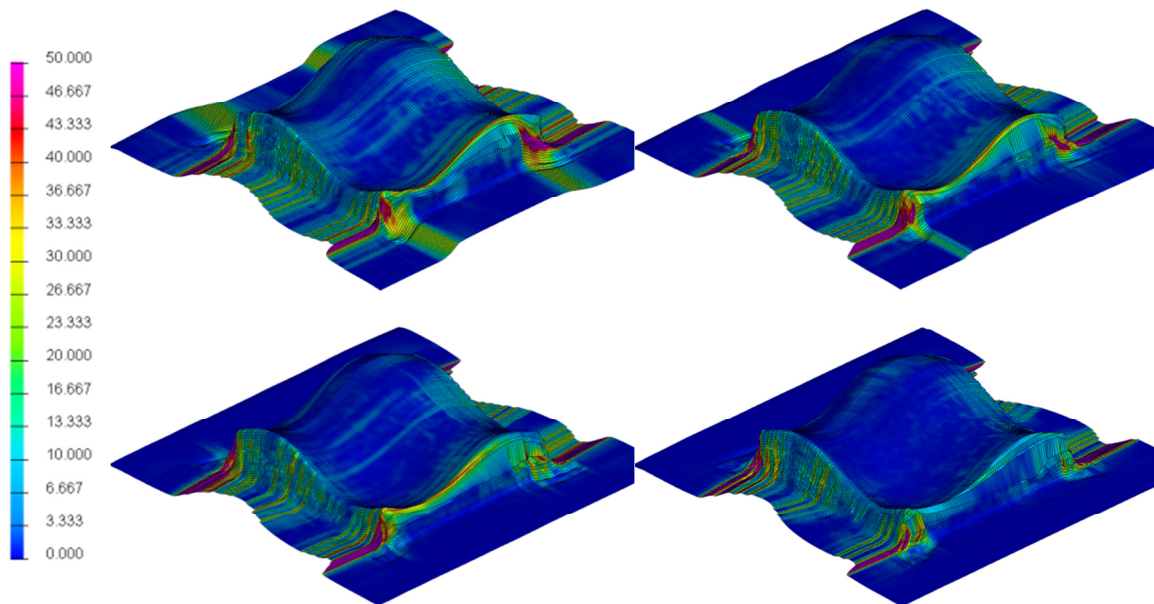


Fig. 6-27 Double Sine simulations showing the shear angle distribution
Standard G-curve (top left); 2x G-curve (top right); 3x G-curve (bottom left); 5x G-curve (bottom right)

With respect to the wrinkle behavior, the matrix strain distribution and the shear angle distribution, the simulation with the double shear stiffness properties showed the most realistic results.

For comparison of the simulation result with the experiments five locations on the Double Sine geometry had been defined. With its symmetry about its diagonal these locations were defined on one side of the diagonal (Fig. 6-28). They had been orientated such that the projected global x-axis defines the 0° -direction.

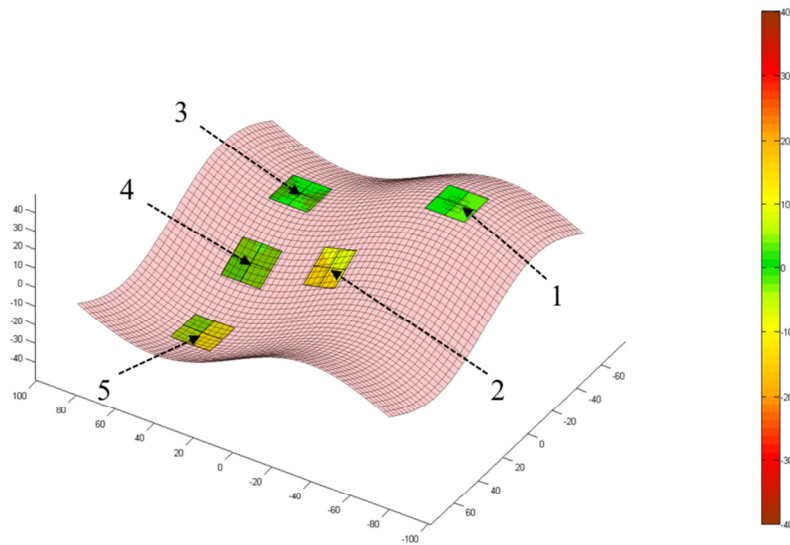


Fig. 6-28 Comparison plot of Double Sine simulation with the numbering of the five measurement areas

As in the hemisphere simulation, the Double Sine simulations with the unmodified shear stiffness properties and the double shear stiffness were used for comparison with the average of the experimental data. The result of the comparison is summarized in Tab. 6-2.

Tab. 6-2 Deviation of fiber direction with respect to the projected x-axis for the Double Sine simulations (standard shear stiffness and double shear stiffness) and the experiments

area	experiment average [°]	standard G-curve (abs. deviation) [°]	2x G-curve (abs. deviation) [°]
1	90.0	89.9 (0.1)	90.7 (0.7)
2	88.4	94.9 (6.5)	96.0 (7.6)
3	88.2	89.7 (1.5)	89.8 (1.6)
4	89.2	89.9 (0.7)	90.5 (1.3)
5	89.7	90.1 (0.4)	89.7 (0.0)

Except area 2 the maximum deviations in the simulations were 1.5° and 1.6° . The simulation with the unmodified shear properties revealed a better prediction of the fiber direction than the simulation with the double shear stiffness. In area 2, both simulations had their maximum deviation from the experiment. Nonetheless, a visual comparison at that measurement area reveals an almost similar fiber orientation. Fig. 6-29 highlights this fiber orientation at the measurement area 2, as top view of the Double

Sine. Two explanations for the fiber deviation from the MATLAB output might be possible. First, the positioning of the PROFACTOR sensor with the robot was done manually via teaching mode. This method cannot ensure an exact positioning. Area 2 required a rotation of the sensor about three axes, whereas the other areas required a rotation only about two axes. Second, the preforms were scanned weeks after forming and were hardening in the meantime. The resulting warping of the preform did not allowed a proper placing on the tooling for the measurement. Even by using double-faced adhesive tape to fix the preform on the tool, it still slightly lifted off the tooling. This offset could also change the fiber orientation with respect to the global x-axis.

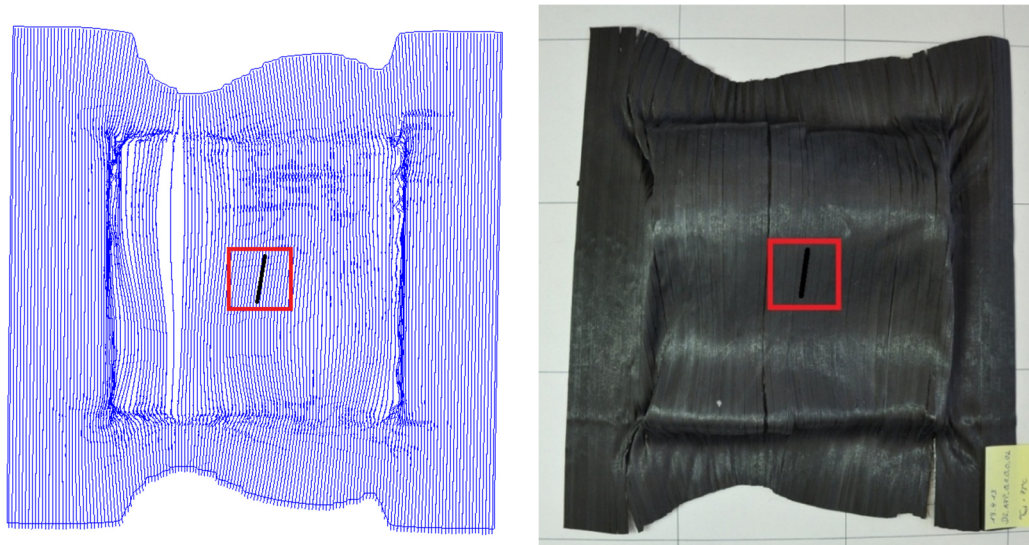


Fig. 6-29 Comparison of fiber direction at measurement area 2
Plot of fiber direction 1 in the simulation with the doubled shear stiffness (left); experimental result (right)

6.6 Conclusion

To validate the material model a stamp forming process was set up with two different geometries to be formed on. With the stamp forming process robust forming results were ensured. With the hemisphere and the Double Sine tools two geometries were used which applied different degrees of deformation on the laminate. The hemisphere led to strong wrinkling of the AFP laminates whereas in the Double Sine forming wrinkles only occurred in the edges. These different forming characteristics suited well for validating the simulation. On the one hand, the model could be checked in terms of predicting the fiber direction. And on the other hand, it was checked whether the simulation is able to model defects like wrinkles or gaps.

The simulation model was set up according to the forming trials. All relevant parts of the process were included. The Teflon foils, in which the laminate was wrapped, were not modeled, but accounted for in the contact definitions. In first simulations the mate-

rial model, as derived in chapter 1, was applied. Additionally, simulations with higher shear stiffness were carried out to check their influence and impact on the results.

For comparison of the simulation results with the experimental trials the fiber angle sensor of PROFACTOR GmbH and a MATLAB routine were applied. The sensor was attached to a robot which positioned the sensor for the measurements at different predefined locations. With the FScan software the measured fiber direction were exported into a MATLAB file. The MATLAB also imports the results from the simulation. By mapping both data on each other their deviations were computed and plotted. Using this comparison method allowed an exact measurement of the preform.

The first validation was done on the hemisphere tool. The simulation was carried out with the material parameter set of chapter 1 and with two, three and five times increased shear stiffness properties. By increasing the shear stiffness the formation of wrinkles increased in parallel. The simulation with the three times higher shear stiffness showed qualitatively the most realistic wrinkling formation. Regarding the matrix strain distribution, all simulations showed locally high strains, but in the experiment the strain was more evenly distributed on the hemisphere. This effect evolved from the tensile description in the material model. As one row of elements first reached the strain above rupture, they strained further while the tensile stress decreased. Other elements did not strain any longer at this point. In the comparison of the fiber directions, the simulation with standard shear stiffness and double shear stiffness showed sufficiently good results in the measurements areas in fiber direction and in perpendicular direction. Deviations of up to 15° showed up in 45° direction of the hemisphere. The wrinkles which lay in this area led to these deviations.

The second validation was carried out on the Double Sine geometry. Again, simulations with varying shear stiffness properties were carried out. Since less wrinkles occurred in the Double Sine forming as in the hemisphere forming, the increase of the shear stiffness did not lead to improved simulation results. But with respect to the draw-in of the laminate and the predicted matrix strain, the simulation with the double shear stiffness properties provided the most realistic result. Comparing the fiber directions, the simulation with the standard shear stiffness showed slightly better results. Deviations of up to 8° occurred in the measurement area at the center. A visual comparison showed a better accordance. The measured values might be wrong, because positioning of the sensor in this measurement area was quite difficult. If the sensor was perfectly positioned or rotated, the simulation results might be even better.

All in all, the simulations of the hemisphere and the Double Sine showed qualitatively good results. The simulations were more realistic if the material parameter set of chapter 1 is used, but with the shear stiffness properties two times increased. This effect results from a too conservative shear stiffness measurement in the PFT. Within the PFT the AFP material reached only low shear angles before wrinkling and rupture of the specimen started. While by forming an AFP laminate adjacent plies stabilize each

other and allow higher shear angles before wrinkling starts. Hence, the boundary conditions under which shearing of the AFP material takes place are different in the PFT and in laminate forming.

A good accordance of all material parameters except the shear stiffness properties was revealed by applying a validation on the material model. But to take this inconsistency into account simulations with standard shear stiffness and double shear stiffness will be done again in the flange forming simulations of the following chapter.

7 Flange forming simulation

The foregoing validation of the simulation model showed promising results for the stamp forming of the hemisphere and the Double Sine geometry. The following chapter now applies the simulation model on an actual industrial application. In this application thick laminates consisting of 36 plies are placed flatly on a circular mandrel and are formed by inflating an underlying bladder in a subsequent step. The laminates are either formed into a closed loop L- or Z-flange. Fig. 7-1 depicts a quarter fractions of the two geometries. For both geometries the mandrel had a radius of ~ 584 mm and the laminate bended up by ~ 25 mm resulting in a hoop strain of 4.2 %. The laminates were built up by layers from 0° until $\pm 65^\circ$. The underlying bladder was made of bagging film and was pressurized with pressures of up to 10 psi (0.69 bar) to form the laminate onto the upper tooling.

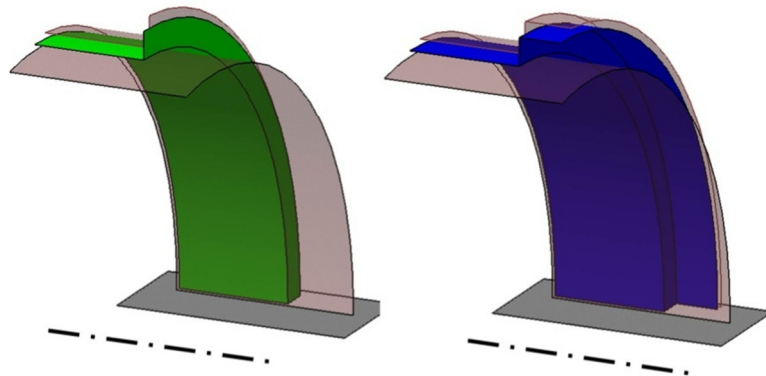


Fig. 7-1 Sketch of the curved L- and Z-flange geometries

To provide detailed simulation results each layer of the laminate needs to be modeled separately. But the simulation of the whole circular flanges would require a too high computational effort. It was therefore resolved to carry out the forming trials on a subscale tooling with a fraction of the flanges. The tool was manufactured out of ABS by rapid prototyping. This allowed the tool to be additionally installed in a CT scanner and to analyze the state of forming of the laminate without disassembling the tool. Moreover it allows investigating the through-thickness mechanisms taking place in the inside of the laminate. This is of great importance especially when forming thick, multi-layered laminates.

In the following chapter, first, the forming trials with the subscale tooling and the used laminate will be described. Afterwards the modeling of the forming process will be described. A special attention will be paid to the meshing of the single plies. Especially for this kind of forming process the meshing technique is crucial. In the main part of

this chapter the results of the final simulation are presented and compared with the images from the CT scanning. A discussion and summary is given at the end of the chapter.

7.1 Forming process

The tool consisted of two parts which clamp the laminate by closing the two parts (Fig. 7-2). For the Z-flange geometry a laminate of 76.2 mm x 76.2 mm size (3" x 3") and ~ 6.4 mm thickness was used. For the L-flange geometry the laminate had a dimension of 76.2 mm x 33.8 mm (3" x 1.3"). The curved tool had a radius of 254 mm (10") at the bottom and 285.8 mm (11.25") at the top. As in the full scale tooling also an inflatable bladder was included to form the laminate. To avoid any breakage of the tooling pressures of maximum 5 psi were applied.

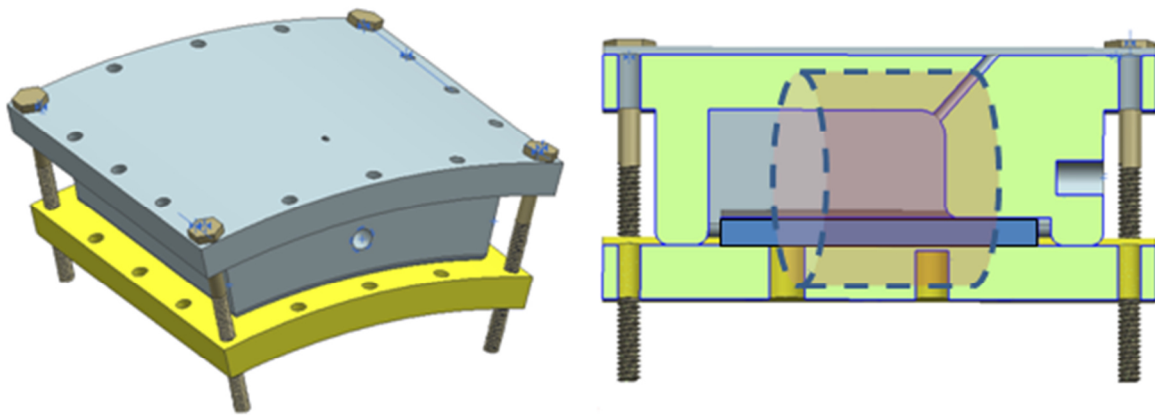


Fig. 7-2 CAD model of the CT forming tool
ABS tooling (light green), AFP laminate (dark blue) and field of view of the CT scanner (dashed line area) [GE]

The laminate consisted of 36 AFP plies in a 0/+45/-45/0 layup. On the top and bottom of the laminate Teflon foils were included to decrease friction on the tooling and to ensure a better demolding afterwards. Prior to forming the laminate was heated up to 65.6° C (150° F) by placing the whole assembly in an oven. The temperature of the laminate was checked by a thermocouple which was attached on the top of the laminate. With a valve the bladder was then pressurized manually up to the desired pressure to form the laminate. In Fig. 7-3 the assembly of the tooling is shown as well as examples of the formed laminates.

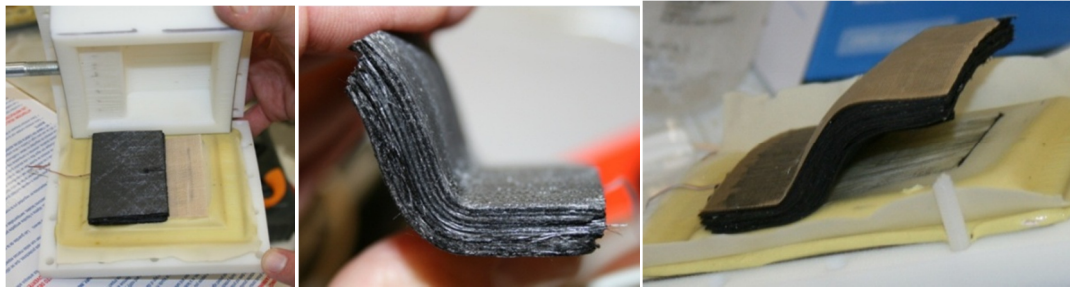


Fig. 7-3 CT forming tool
Positioning of the specimen for the L-flange forming (left); formed L-flange specimen (center); formed Z-flange specimen (right) [GE]

After forming the pressure was released and the closed assembly was placed in the CT scanner. The tool was positioned to scan the laminate at the center (Fig. 7-2). The CT scanner allowed a field of view with 50 mm diameter. For comparison with the simulation the cross section cuts in the center and the through thickness views were provided.

7.2 Simulation model

The description of the simulation model is divided into two parts. First, the model setup will be presented and second, the meshing technique of the plies. As the meshing technique is crucial, it will be addressed separately. Different simulations had been carried out to emphasize the impact on the simulation results depending on the meshing technique.

7.2.1 Model setup

The simulation model included each single ply of the laminate, the bladder, the outer tooling, and a partial plane of the inner tooling. The Teflon foils were not modeled as they do not influence the forming directly. They had been accounted for by modifying the friction coefficient between plies and tooling/bladder accordingly.

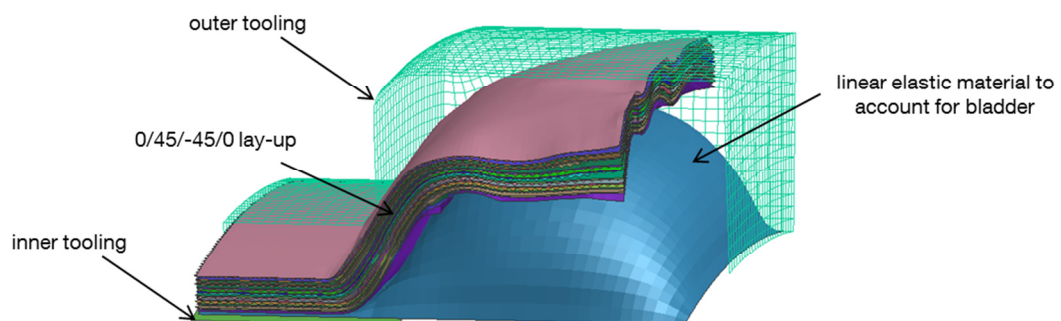


Fig. 7-4 Model setup of the CT forming simulation

The inner tooling was modeled partly as it only touches the bladder in the clamping area. Modeling the whole inner tooling would lead to a higher computational time and was therefore neglected.

Even though the bladder has a non-linear strain behavior while inflating, it was modeled with a linear elastic material. A non-linear material model was not used as no stress-strain data of the bladder material were present. But to account for the correct behavior, tests with the empty tooling at different pressures were carried out. A hole was drilled in the outer tooling and with a wooden stick the position of the bladder was detected for different pressures. For each pressure the Young's modulus of the bladder was determined by replicating the measured values from the wooden sticks. By this method it was possible to use the correct Young's modulus in the linear elastic material model for each simulated pressure.

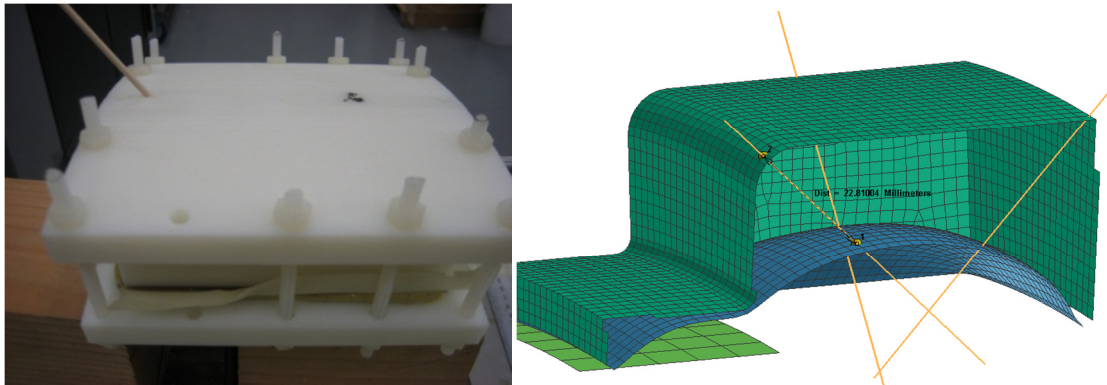


Fig. 7-5 Pressure tests with the empty tooling to determine the elastic behavior of the bladder at different pressures

Closed and pressurized tooling with wooden stick to determine the position of the bladder (left) [GE]; measurements of the bladder position in the simulation (right)

In the simulation the bladder was inflated by using the fluid cell option (*FLCEL*). This option assumes an enclosed volume underneath the bladder which is filled by a compressible fluid and blows up the bladder until the desired pressure. The fluid cell option ensures a smoother inflating of the bladder rather than standard shell pressure. Preliminary simulations with a standard shell pressure showed high dynamic effects which influence the simulation results.

7.2.2 Meshing technique

The way of meshing the laminate and the single plies, respectively, was a crucial step for this geometry. Besides the element size, the alignment of the elements is very important in forming simulations. As mentioned in chapter 3.4, the elements for each ply should be aligned in direction of the fibers to avoid shear/tension locking effects. These effects are critical at high shear deformations. In this case, the used AFP material possess a high shear stiffness (cf. 4.1) and shows only small shear deformations during draping. As an example Fig. 7-6 shows the shear angles in a formed laminate having a maximum shear angle of 12° . The maximum shear angle is located at the edges of the plies and is more a numerical effect rather than a draping effect. In fact, the maximum shear angle within the plies is approx. $\sim 4^\circ$. From the numerical point of

view, these low shear angles are beneficial since possible tension locking effects are negligible small at these states.

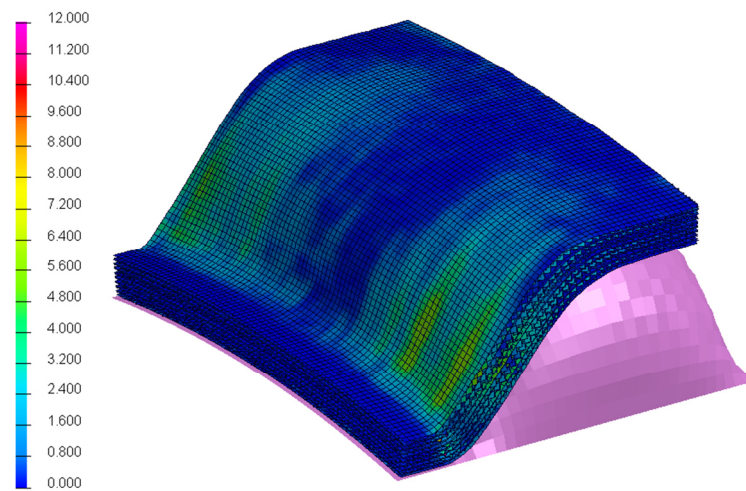


Fig. 7-6 Shear angle distribution in the formed laminate

Especially for this geometry it was difficult to mesh each layer along the according fiber direction. As the laminate had an initial curvature, the meshing of the 45° -plies was not possible with standard meshing tools. Fig. 7-7 shows the difference of the $0^\circ/90^\circ$ ply and the $\pm 45^\circ$ ply. The $\pm 45^\circ$ ply has square-edged boundaries to ensure a homogenous mesh of quadratic shaped elements. A planar $\pm 45^\circ$ ply mesh can be generated by creating a larger $0^\circ/90^\circ$ ply mesh, rotate it accordingly and cut the mesh in the desired shape by deleting elements. An initially curved $0^\circ/90^\circ$ mesh cannot be rotated without losing the bending direction. This mesh here was generated by the help of a kinematic draping tool (PAM-Quikform). First the curved surface was modeled. Then a kinematic draping simulation was performed on it with the E_1 -direction in 45° -direction. The resulting mesh was then exported and used as the FE mesh in the actual draping simulation. This meshing method is effective but gets time consuming if many plies need to be meshed. Therefore the draping simulation was additionally analyzed with a non-oriented mesh in which all plies had a $0^\circ/90^\circ$ mesh (Fig. 7-8). To account for the different fiber directions, the part and materials cards of each ply were accordingly set.

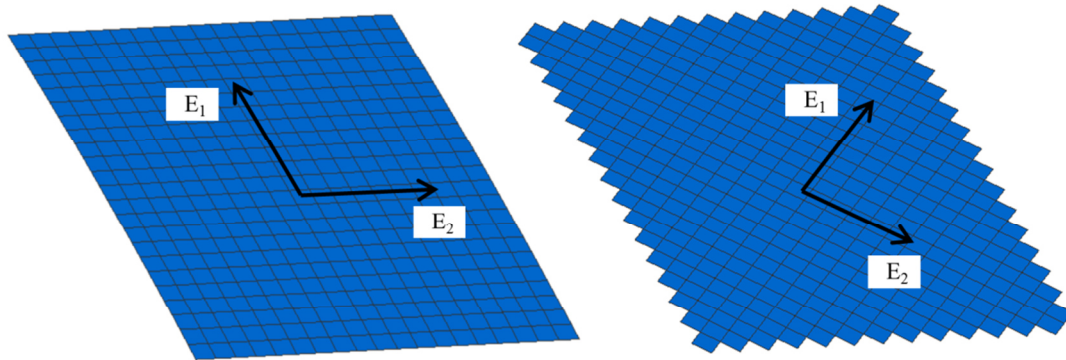


Fig. 7-7 $0^\circ/90^\circ$ - and $\pm 45^\circ$ - mesh of a bended plane

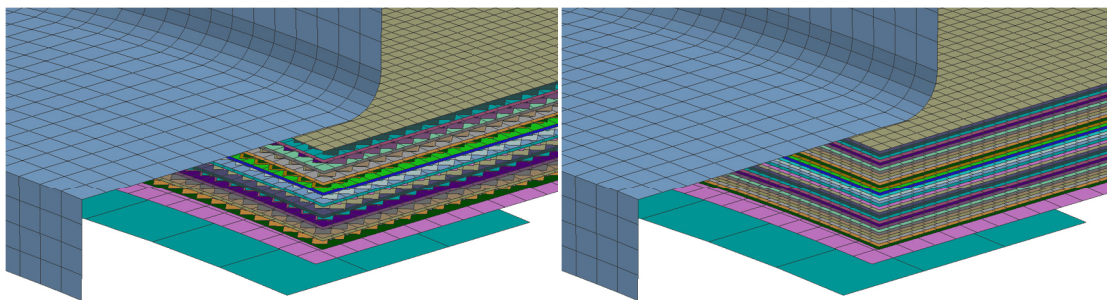


Fig. 7-8 Different meshing methods in the flange forming simulation

All elements aligned with the according fiber direction (left); all elements oriented with the global axis of the model (right)

A direct comparison of the two meshes revealed a more realistic forming behavior of the non-oriented mesh (all elements in the same direction). Especially at the clamping area, the non-oriented mesh bended better around the lower radius as the oriented mesh (Fig. 7-9). The oriented mesh was not able to undergo the same bending curvature as the non-oriented mesh.

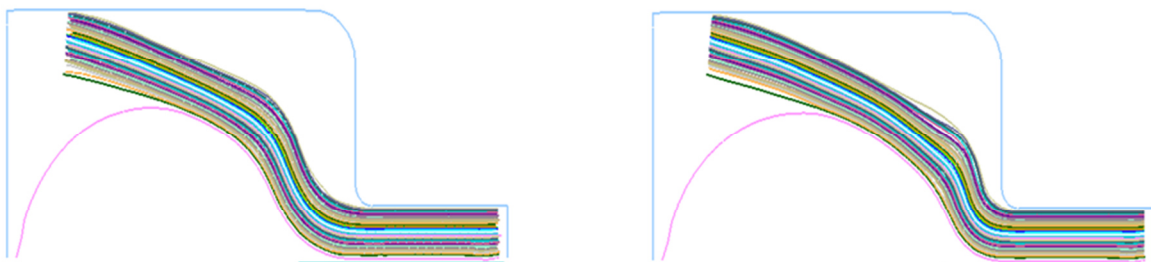


Fig. 7-9 Comparison of the two different meshing techniques

Simulation with the elements oriented in fiber direction (left); simulation with the non-oriented mesh (right)

Obviously the oriented mesh evolves a higher bending stiffness than the non-oriented mesh. This behavior is due to the fact that a standard shell element has a softer bending

in element direction as in diagonal direction. A mesh with quadratic shell elements (8 nodes) would not show such differences, but MAT140 can be only used with linear shell elements.

The different forming behaviors of the two meshing techniques do not allow a clear statement about the most suitable meshing technique for the flange forming. Therefore both meshing techniques will be applied and validated in the following.

7.3 Results

The forming experiments were carried out with pressure from 0.5 psi till 2.5 psi and simulated likewise. The CT scans provided images of the laminates cross-section view and through-thickness view. In the following subchapter, these CT scans were used to analyze the simulation results in terms of laminate bending, shear deformation, matrix strain, gap opening, tow rotation and ply delamination. For each geometry four simulations with different modeling were carried out. On the one hand the two aforementioned meshing techniques were applied and on the other hand the standard (measured) shear stiffness and the doubled shear stiffness like in the validation chapter were used. An interpretation and explanation of the simulation results will be given for both geometries.

L-flange

The L-flange forming was done with pressures of 1.5 psi (0.103 bar) and 2.5 psi (0.172 bar). The CT scans provided the cut-section views at the center plane and the through-thickness views of the up bended laminate (Fig. 7-10). The through-thickness views were a flattened view along the plies to generate a top view of each single ply. Fig. 7-10 depicts the path along which the through-thickness views had been generated.

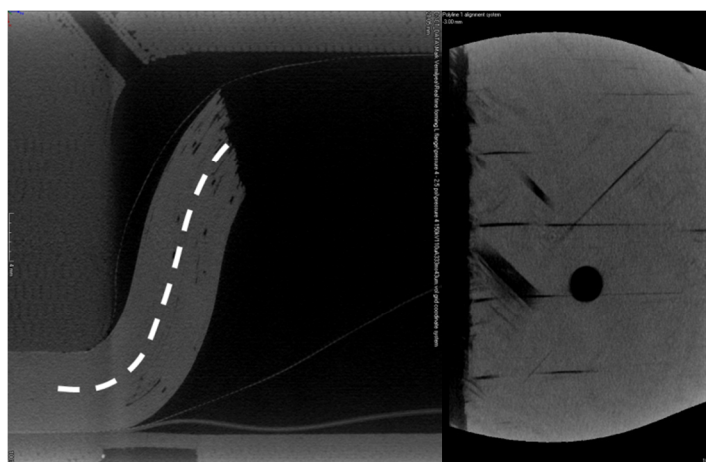


Fig. 7-10 Views provided from the CT scans

Cut-section view of the center plane (left); through-thickness view along the dashed line [GE]

In Fig. 7-11 and Fig. 7-12 the simulation results for the 1.5 psi and the 2.5 psi pressure are shown, respectively. The simulation results of the oriented mesh and the non-oriented mesh are presented each with the standard shear stiffness and the doubled shear stiffness.

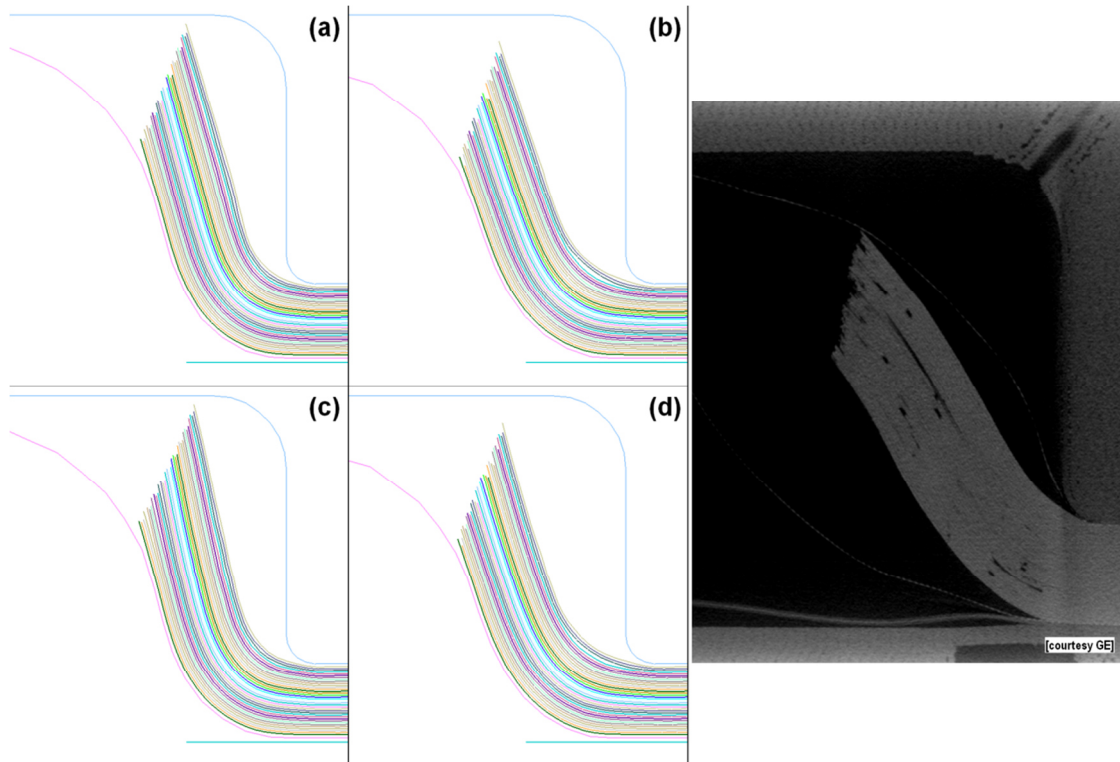


Fig. 7-11 L-flange forming at 1.5 psi

Non-oriented mesh (a); oriented mesh (b); non-oriented mesh with doubled shear stiffness (c); oriented mesh with doubled shear stiffness (d)

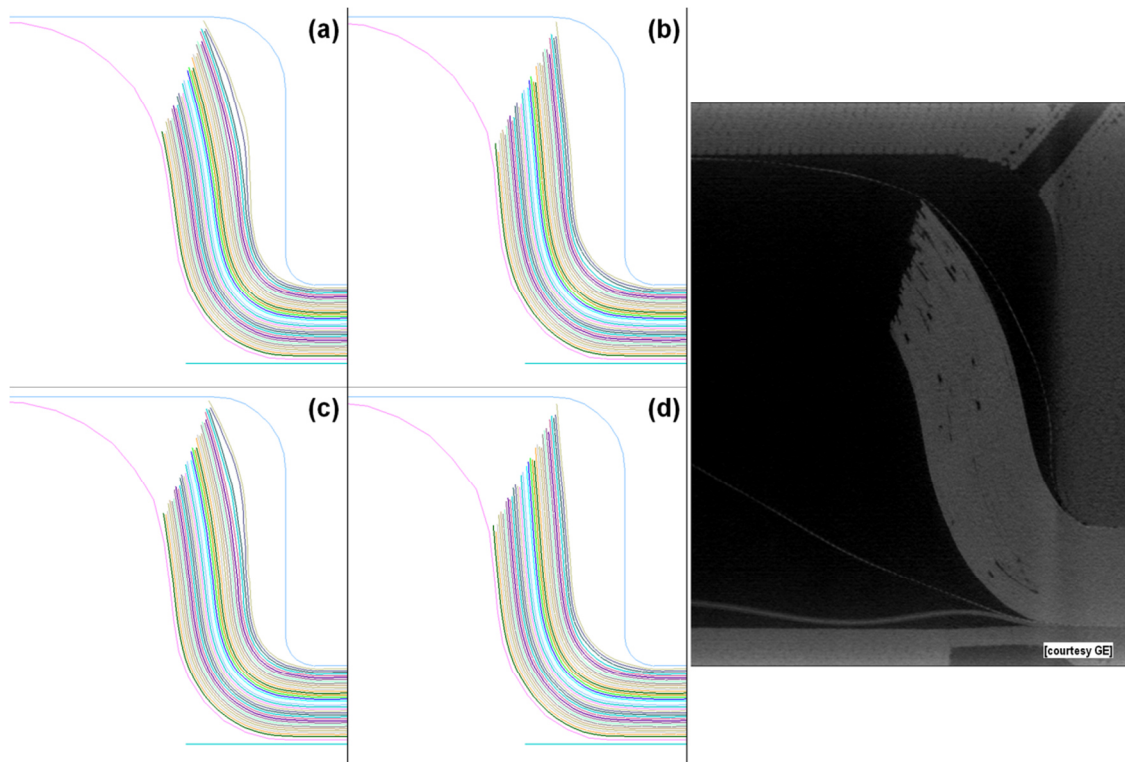


Fig. 7-12 L-flange forming at 2.5 psi

Non-oriented mesh (a); oriented mesh (b); non-oriented mesh with doubled shear stiffness (c); oriented mesh with doubled shear stiffness (d)

In contrast to the simulations of the validation tests, there were no noticeable differences between the simulations with the standard shear stiffness and the double shear stiffness. The slope of the upright laminate and the bending curvatures were similar for both shear stiffness. This indicates again the low shear deformation taking place in this forming process.

Regarding the different meshing techniques, differences in the laminate slope and the bending curvature are clearly visible. The simulations with the non-oriented mesh underwent higher bending curvatures than the oriented mesh. Nevertheless, none of the simulation models were able to form exactly about the lower radius like in the experiment.

The through-thickness views were used to investigate the matrix strain or tow spread, respectively, and the rotation of the tows. The freeware tool ImageJ was used to analyze the CT scans and to measure the tow widths and angles. To do so, the tow edges needed to be tracked which was not possible for all tows in a single CT image. For a more accurate measurement up to six consecutive CT images were used to measure a single tow. The measurements were done for the 2.5 psi experiments as the deformations of the tows were higher than in the 1.5 psi experiment and better to measure.

Fig. 7-13 - Fig. 7-15 compares the tow spread-up (matrix strain) of the experiment and the simulation with the standard shear stiffness and the non-oriented mesh. The CT

images show the tows/plies with the clamping area at the right hand side. Initially, the tows had a width of 6.35 mm (0.25"). After forming a widening of the measured tows is clearly visible for all ply directions. This effect results from the forming curved laminate from a lower bending radius to a higher bending radius. The tows have to undergo a hoop strain at the upper end of the laminate to do so. Especially the 0° tows show this stretch. The here shown tow has a strain of $\epsilon_{ln} = 0.022$ at its upper part. The predicted strain in the simulation is $\epsilon_{ln} \approx 0.055$ which in addition involves the separation of the tows. This tow separation was not taken into account in the measurements of the CT images but can be clearly seen when following the gap next to the tow from its clamping till its upper end. The predicted matrix strain is therefore realistic and satisfyingly good.

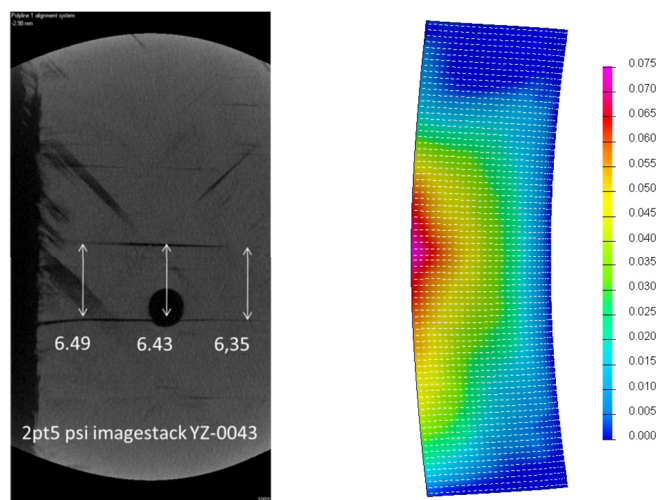


Fig. 7-13 Tow spread-up/matrix strain of a 0° ply

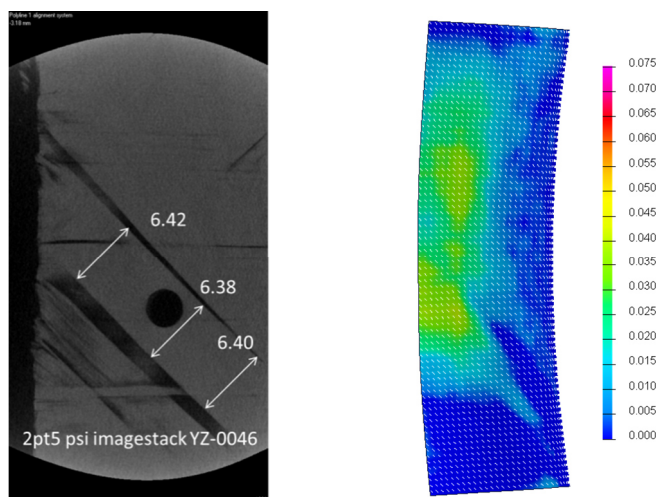


Fig. 7-14 Tow spread-up/matrix strain of a $+45^\circ$ ply

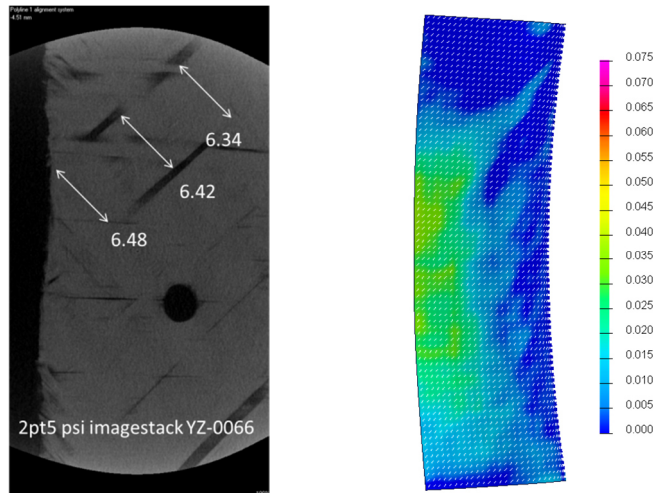


Fig. 7-15 Tow spread-up/matrix strain of -45° ply

The rotations of the $\pm 45^\circ$ tows were measured with respect to the adjacent 0° tows. As the tow rotation changes gradually along their length the measurements were not absolutely precise. For the measurements locations had been chosen where it was possible to track the edges of the $\pm 45^\circ$ tows and a 0° tow in single image. By this method a tow angle of 44.4° and 46.0° were measured in the CT images (Fig. 7-16).

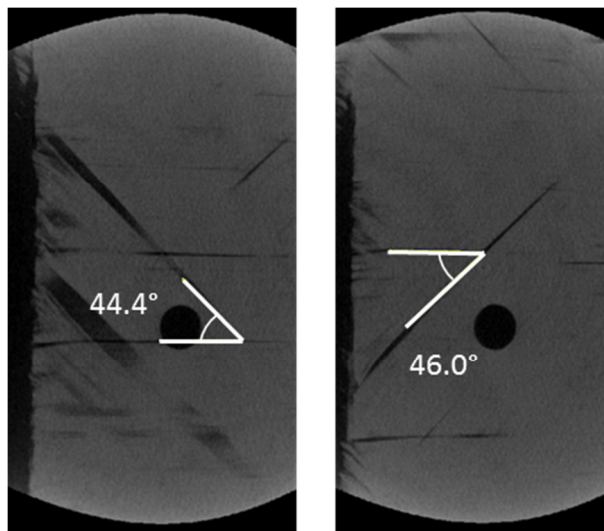


Fig. 7-16 Tow rotation of a $+45^\circ$ and -45° tow [GE]

Within the post-processor Visual-Environment it was not possible to directly plot the angles between different plies. Only the direction vector of the fibers for each element is provided. To measure the tow rotation the fiber direction vectors of an element of the $\pm 45^\circ$ plies were read as well as the fiber direction vector from an adjacent element of the 0° ply. This has been made at different positions, roughly in the area where the measurements of the CT images had been taken. Angles between 43° and 47° were calculated, which again indicates a satisfyingly good result of the simulation.

All in all the simulation of the L-flange forming provided good results. The main forming effects like low shear deformation, high matrix strain, gap openings and tow

rotations were reflected in the simulation. Only the bending behavior at the lower radius was not modeled correctly. The bending behavior was too stiff, especially in the simulation with the mesh oriented according to the fiber directions. The mesh with the $0^\circ/90^\circ$ orientation showed an improved behavior but was still too stiff. To avoid this effect one possibility might be to use a finer mesh. This would increase the plies flexibility but also lead to a higher computational time.

Z-flange

The Z-flange was formed with pressures of 0.5 psi (0.034 bar), 1.0 psi (0.069 bar) and 1.5 psi (0.103 bar). From the CT scans only the cross-section views were provided. Again, the simulation was carried out with the standard shear stiffness and the double shear stiffness of the AFP plies as well as with an oriented and a non-oriented FE mesh. Fig. 7-17 - Fig. 7-19 show the simulation results in comparison with the CT scans.

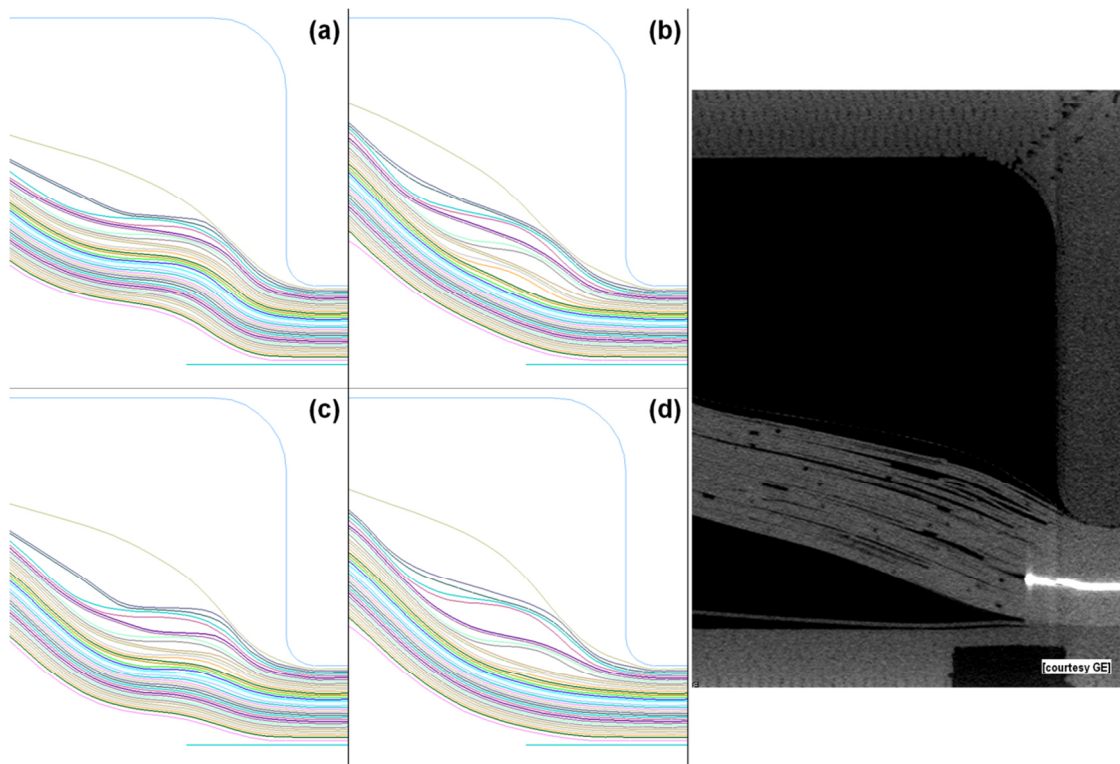


Fig. 7-17 Z-flange forming at 0.5 psi

Non-oriented mesh (a); oriented mesh (b); non-oriented mesh with doubled shear stiffness (c); oriented mesh with doubled shear stiffness (d)

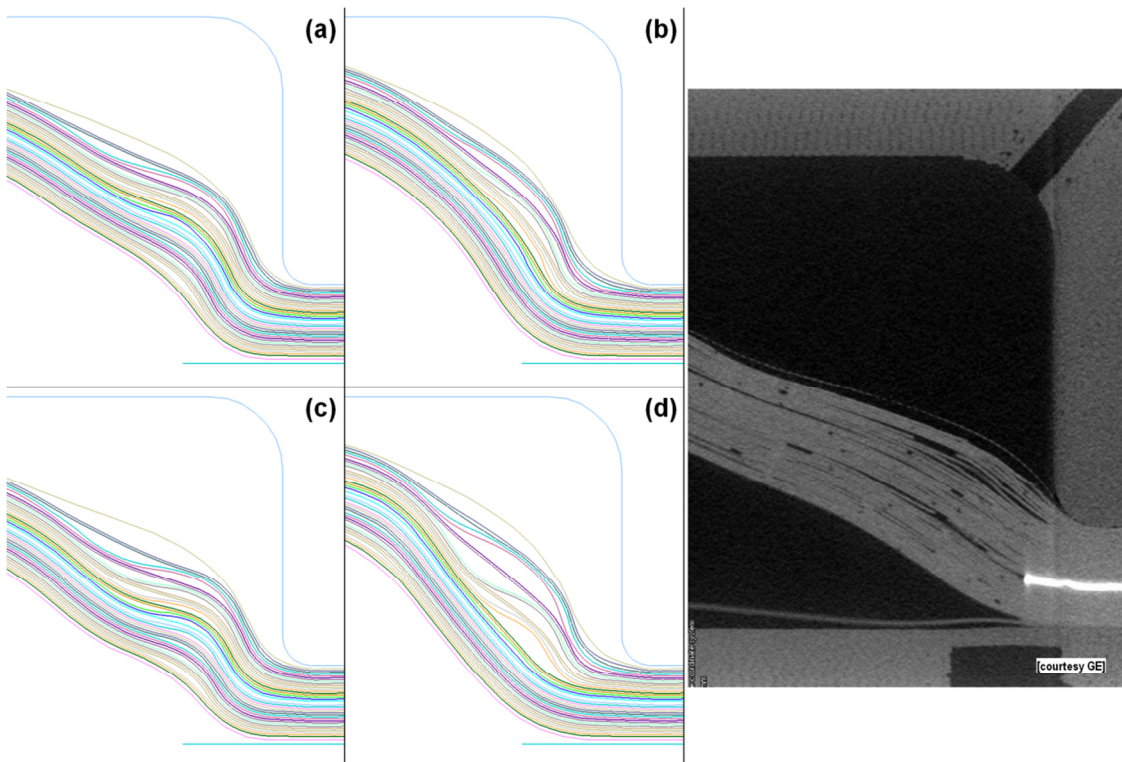


Fig. 7-18 Z-flange forming at 1.0 psi

Non-oriented mesh (a); oriented mesh (b); non-oriented mesh with doubled shear stiffness (c); oriented mesh with doubled shear stiffness (d)

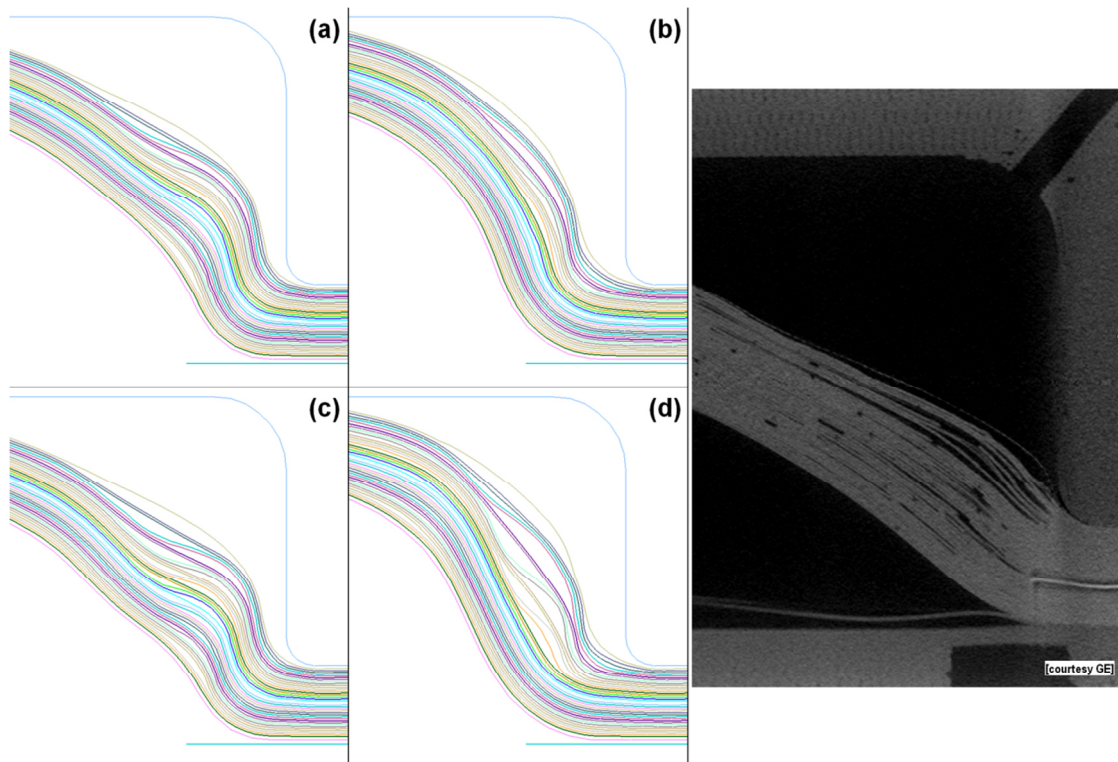


Fig. 7-19 Z-flange forming at 1.5 psi

Non-oriented mesh (a); oriented mesh (b); non-oriented mesh with doubled shear stiffness (c); oriented mesh with doubled shear stiffness (d)

In contrast to the L-flange forming, a delamination of the plies takes place in the Z-flange. Already by forming with a pressure of 0.5 psi the top plies separate from the laminate. With higher pressures this effect gets even stronger. The delamination starts at the lower radius but closes again after 10-15 mm.

This delamination is also shown in the simulation results. However, the simulation results differ much more as in the L-flange simulation. Especially a strong difference between the simulations with the standard shear stiffness and the double shear stiffness can be seen. The simulations with the double shear stiffness overestimate the delamination. Apparently, the higher shear stiffness lead to higher in-plane stresses which in turn result in stronger buckling effects and consequently higher delamination. Regarding the simulations with the standard shear stiffness reveal a better modeling of the delamination in the simulation with the oriented mesh. On the other hand, the simulation with the non-oriented mesh ($0^\circ/90^\circ$) bends better around the lower radius.

The laminate angle and laminate curvature is well modeled by all simulations at 1.0 psi and 1.5 psi. But for 0.5 psi pressure the simulation predicts a slightly higher laminate angle as in reality.

In summary all simulations showed acceptable results. By looking at the laminate angle, the delamination of the plies and the bending around the lower radius, the simulation model with the standard shear stiffness and the $0^\circ/90^\circ$ mesh provides the best re-

sult. Like in the L-flange simulations the simulation with the $0^\circ/90^\circ$ mesh has a more realistic bending behavior as the oriented mesh. The shear stiffness only influences the delamination behavior of the plies. With higher shear stiffness the delamination increases as well. The laminate angle and the laminate curvature are not influenced by the shear properties. This aspect demonstrates again the low shear deformability of the AFP material.

7.4 Conclusion

The simulation model which was derived in the foregoing chapters was used in this chapter to simulate the forming process of curved L- and Z-flanges. Instead of simulating a whole 360° flange, a subscale tooling was developed to carry out the forming trials at a smaller size and to keep the computational effort in an acceptable time frame. Within this subscale tooling an AFP laminate with 36 plies was formed by an inflatable bladder at different pressures. The whole tooling was transferred into a CT scanner to investigate the formed laminate without opening the tooling.

These forming processes were likewise modeled in the simulation and compared with the CT images. In the simulation and in previous studies a strong dependency of the meshing technique on the simulation results was shown. The forming of the L- and Z-flanges primarily leads to a bending of the laminate; the shear deformation plays only a minor role. Due to the low shear deformations the meshing of the plies is not as crucial as in the previous simulations. Generally, it is recommended to orient the mesh of each ply along the fiber direction to avoid shear/tension locking effects. In this case it was more convenient to have the mesh aligned with the main bending radius. Since the linear shell elements have a more realistic bending behavior along their element edges, they formed better about the lower radius of the tooling as the simulation with the individual meshed plies. This issue is not only important for the L- and Z-flange forming, but for forming AFP materials in general. In chapter 4.1 the PFT results showed the low shear capabilities of the AFP material. The meshing of AFP materials is therefore not as crucial as for woven fabrics. Hence, for further simulations of AFP laminates it is recommended to mesh the plies not strictly according to the fiber direction, but also take bending curvatures into account.

Like for the hemisphere and Double Sine simulations, simulations of the flanges with standard and double shear stiffness were also done. In the L-flange simulations both models showed almost the same forming behavior. In the Z-flange the two models showed the same results with respect to the laminate bending angle, but had different results with respect to the delamination behavior. The models with the double shear stiffness had a stronger delamination of the plies. With the higher shear stiffness the plies are more likely to buckle and consequently lead to this severe delamination behavior.

For the L-flange the CT scans provided additionally through-thickness images of the laminate. From these images the matrix strain, the gap opening and the tow rotation were analyzed and measured. The simulation provided the same effects and had a good correlation with the experiment. Even though the simulation is not able to model the gap opening directly, it was still able to account for it by looking at the matrix strain. Also the tow rotation was well predicted by the simulation.

8 Discussion

The following chapter will revise and discuss the results of this work. The gained findings from each chapter will be related to findings and results of other chapters. This chapter will lead to a comprehensive understanding about the whole procedure of performing a forming simulation for AFP materials. Potentials and limitations will be given as well.

Within the material characterization five different tests were used: the PFT, the Cantilever bending test, the friction test on the horizontal plane, the uniaxial tensile test, and the thickness measurement.

The PFT provided the shear behavior of the AFP material within low shear strains. Higher shear strains were not possible to apply due to the boundary conditions in the PFT. The laminate is not constrained in thickness direction and consequently the formation of wrinkles is not hindered. In real forming processes the laminate is often constrained in thickness direction. Single plies are stabilized by adjacent plies or the tooling keeps the laminate in plane. Hence, the PFT is able to apply shear deformation on the laminate but not under conditions as in real forming processes. However, the measured values were applied in the simulation and showed up to be too conservative. By applying stiffer shear properties the simulation provided better results. For an exact shear characterization of the AFP material an alternative test method is required.

The other material characterization tests provided sufficient results for the material model. Even though the Cantilever bending test was difficult to handle, the test derived useful bending stiffness values of the AFP material in the linear region. If the bending behavior of the AFP material need to be tested in the non-linear region, the Cantilever test is not sufficient anymore. Nevertheless, in PAM-FORM only constant bending stiffness values are usable.

The same holds for the friction test on the horizontal plane. The values which had been derived were sufficient for the material model. The dynamic friction coefficients were determined for all material pairs which occur in the flange forming simulation. The viscous dependent friction behavior was not possible to be determined by the horizontal friction test, but also cannot be accounted for in the simulation. An alternative friction test is required if the friction behavior needs to be characterized also to this extend.

The uniaxial tensile test provided satisfying results even though the specimens showed high deviations due to manufacturing tolerances. In those specimens where the tows were not exactly placed next to each other, the gaps in between acted as rupture initia-

tion and lowered the tensile stiffness. The tensile test was carried out in a tensile testing machine with a 10 kN load cell; the lowest available at the LCC. Still, it was able to measure the low forces which were required to pull the specimen apart. But to further improve the tensile characterization, one has to use another test method which allows measuring the forces with a higher resolution than the used load cell.

Last step of the material characterization was the thickness measurement. It provided sufficient results and did not need any improvement.

With respect to simulating AFP laminates, the material model MAT140 of PAM-FORM was not as robust as required. Implementing the measured material parameters directly in the material model, partially led to unexpected behavior. This behavior necessitated to simulate the material characterization test to derive the parameters which ensured a correct behavior. Except the thickness measurement all conducted material characterization tests were simulated for that purpose.

First simulation was the friction test. As the contact and friction definition is independent of MAT140 and a standard option in PAM-FORM, it revealed a robust behavior which did not required any altering of the measured friction coefficients. In this work the orthotropic friction model was used to account for the direction dependency of the AFP material. PAM-FORM also offers a velocity-dependent and a pressure-dependent friction model, to account for the viscous frictional behavior. A combination of all friction models would increase the quality of the simulation model, but only a single one can be defined in the simulation at a time.

The second simulation modeled the tensile test. It was possible to modify the tensile behavior, to ensure the same behavior as in the experiment until the strain when rupture started. Beyond this point it was not possible to ensure an absolute correct behavior. The descending path of the stress-strain curve shows a degrading material behavior (softening) and was difficult to capture in PAM-FORM. Nevertheless, the overall tensile behavior was sufficiently good. To improve the material model, it would require a better post-rupture behavior or an element elimination option with a predefined strain.

The third simulation modeled the bending test. Difficulties showed up to keep the bended specimen in a static position. It was realized by applying a material damping option and defining a long simulation time. To ensure a correct bending behavior the material model needed to be modified. In the 0° bending test the material model initially was too soft and in the 90° bending test initially too stiff. Most probably the measured values were not absolutely correct and led to this discrepancy. In the tests the specimen were heated by an air gun. The airstream might have influenced the bending of the specimen. Hence, the bending test method must be improved rather than the material model. Promising results of an alternative method were recently presented by Margossian [112].

Last simulation of the material characterization tests was the PFT. The simulation showed the same wrinkling behavior as in the experiment. Additionally the matrix

strain and the shear angle distribution indicated the locations where rupture occurred. The force-displacement curve of the initial simulation showed a too stiff shear behavior of the material model. After calibrating the shear modulus curve the material model was able to represent the experimental force-displacement curve until a shear angle of 25°. Further shearing led to a locking of the material model and it was not able to compensate this stiffening. Since the AFP material does not undergo such high shear strains in forming processes, this limitation is acceptable. But if textiles with high shear capabilities (e.g. dry woven fabrics) should be simulated, it might be possible that shear locking turns up if the textile is highly deformed.

In summary, the simulations of the characterization tests showed how important it is to perform a reverse approach for determining the required material parameters for the simulation model. Especially the tensile stiffness and shear stiffness were modified to ensure a correct material behavior. The deviation of the measured material parameters and those which were finally used in the simulation arose from two reasons. First, the material model MAT140 is able to represent a robust behavior only until a certain degree of deformation. But if the material model is highly deformed and reaches highly non-linear states it shows unrealistic behavior. Second reason is the limitations and boundary conditions of the material characterization tests. The tests used in this work mainly originate from dry woven fabric testing. By testing AFP materials the test results might not show the expected behavior (e.g. early wrinkling in PFT). Hence, to improve the quality of the measured parameters, AFP specific material characterization tests need to be developed in future.

By performing a validation of the derived material model, its overall deformation behavior was checked and the interactions among the different material parameter were investigated. A robust forming process was developed by stamp forming on the hemisphere and on the Double Sine. Using the PROFACTOR fiber angle sensor allowed an exact measurement of the fiber alignment at predefined locations on the preforms. With a MATLAB routine the measured results were then mapped onto the simulation results and compared with each other. Additionally, a visual comparison of the general forming behavior in terms of wrinkling and gap opening was done. In summary the simulations with doubled increased shear stiffness provided the most realistic behavior. The wrinkling formation, the gap opening and the draw-in of the AFP laminate were best in this simulation model. The simulations with the unmodified shear parameters often underestimated the wrinkling behavior. In the hemisphere simulation the model with the double shear stiffness also provided better results with respect to the predicted fiber alignment. In contrast, in the Double Sine simulation the model with the original shear stiffness had in average a better behavior than the one with the double shear stiffness. At locations with high deformations of the AFP laminate, all simulations were not able to provide a sufficient prediction of the fiber alignment. It was mainly due to wrinkles which were present in the experiment but not in the simulations. Nevertheless, the material model showed in general sufficient results. It has to be

mentioned that deviation of the predicted fiber orientation might be even lower, as an exact positioning of the PROFACTOR sensor was not possible by programming the robot in the teaching mode. For further validations it is recommended to recheck the positioning of the robot.

The differences of the original shear stiffness and the increased shear stiffness were additionally investigated in the final simulations of the L- and Z-flange forming. In experiments thick AFP laminates were formed by an inflating bladder within an ABS tooling to examine the forming by a CT scanner. The simulation of this forming process showed minor differences when comparing the different shear stiffness. To form the curved L- or Z-flanges the laminate undergoes only small shear strains. Hence, the shear stiffness was not as sensitive in these simulations as in the previous simulations of the hemisphere and the Double Sine. More important was the type of FE mesh applied. The simulations with the FE mesh oriented along the flange axis had a better forming behavior than the simulations with the mesh oriented along to the fiber directions of each ply. Since the shell elements bend easier along their edges and the flange forming is dominated by bending deformation rather than shear deformation, the simulation with the non-oriented mesh formed better into the flange geometries. Even though this mesh might lead to shear/tension locking, the occurring maximum shear angles were below the region where shear/tension locking occurs. In the case of the L- and Z-flange forming it is therefore recommended to use the non-oriented mesh. But for other geometries or forming processes this recommendation might be wrong. Best practice would be to perform simulations with different meshes and examine the maximum occurring shear angles. If these shear angles are quite low, the risk of shear/tension locking is also low. Other aspects like high bending deformations or high tensile strains might then be the crucial factors. Another possibility would be to apply a material model which is free of any shear/tension locking effects and which can be used with quadratic shell elements. In such a case, the mesh dependency would only be related to the element size.

Altogether this work presented a whole procedure to simulate the forming of AFP layups. The gained results were sufficiently good and helped to understand the deformation mechanisms taking place in AFP laminate forming. Even though the applied material model and the material characterization tests are mainly used in forming simulations of dry woven fabrics, it was possible to extend them to AFP laminates. Dominated by its tow-based structure, the tension in cross-fiber direction was more influencing than the shear deformation as in dry textile forming. To further improve the quality of AFP laminate forming simulations other material models and material characterization methods are required which account better for this effect. A suitable material model would either allow element elimination to account for tow separations or represent the laminate a mesoscopic scale. The latter would allow a very detailed investigation of the tow mechanics but also needs a high computational effort.

9 Summary and Outlook

This work presented a procedure of using the FEM to simulate the forming of AFP laminates. The goal was to apply the forming simulation for supporting the development of new forming processes. Besides the forming simulation the work further included the characterization of the AFP material, the implementation of the data into the material model and the validation of the material model. It showed methods of how to perform each step and reveals the possibilities and limits.

For characterizing the AFP materials and laminates, respectively, existing test methods were used and adapted accordingly. The material characterization tests allowed determining the material parameters which are required in the material model of the simulations. Not all test methods showed up to be suitable for testing AFP materials. Therefore, all tests were simulated again and checked whether the determined parameters lead to a correct behavior in the simulation or not. The friction test and the bending test showed quite robust results and did not require major modifications of the measured parameters. The highly non-linear behavior in the tensile test and PFT showed larger deviations in the simulations. With modifications of the material parameters a more realistic behavior was finally achieved.

The updated material model was additionally checked in a validation process to proof its quality. Forming trials on two geometries were carried out and the fiber alignments in the preforms were scanned by an optical sensor. The forming trials were simulated in parallel by using the updated material model. With an MATLAB routine the measured fiber alignments and the simulation results were mapped onto each other and their deviations were computed. In general acceptable results were shown but could be improved by altering the shear stiffness in the material model. The validation proofed the low shear capabilities of the AFP materials but also the unsatisfactory measurement of the PFT. The measured shear stresses from the PFT were too conservative and led to higher shear deformations as in reality. To gain more accurate results in future an improved test method for characterizing the shear behavior of the AFP material would be required.

Finally, the material model was applied to simulate the forming process of thick AFP laminates into curved L- and Z-flanges. Forming trials were carried out which were inspected by a CT scanner. The CT images allowed to investigate the deformation mechanisms taking place within the laminate and were compared with the simulation results. Due to low shear deformations in the flanges, a correction of the shear stiffness as in the validation was not required. The material model was able to provide the same behavior in tow spread and tow rotation as in the experiment. Only the bending behav-

ior of the laminates was critical in the simulation. The bending behavior showed up to be strongly dependent on the orientation of the FE mesh. An orientation of the mesh along the main fiber direction led to a too stiff bending behavior. A mesh oriented along the main bending radius led to a more realistic behavior since the used linear shell elements bended more easily along their element edges.

This work showed a way to simulate the forming process of AFP materials. For each required step solutions were presented. This work also showed the possibilities in the forming simulation of AFP materials but also its limitations. Even though, the provided results were satisfyingly good, there is still potential for improving the quality of the simulation. Mainly, the material model and the material characterization tests could be improved. The material model might be adapted to better present the tow-based structure of the AFP laminates and its deformation mechanisms. The material characterization tests which were generally used to test dry textile materials might not be the perfect solution for the AFP laminates. For more accurate results new test methods are required.

Forming of impregnated materials gains increasingly interest in composite industry and so in the research community as well as on the software side the covered topics in this work gain more and more importance.

Literature

- [1] J. Hale, “Boeing 787 from the Ground Up”, *Boeing - Aero*, no. 4, 2006.
- [2] G. Hellard, *Composites in Airbus: A Long Story of Innovations and Experiences*. 2008.
- [3] D. Brosius, *Boeing 787 Update: Approaching rollout and first flight, the 787 relies on innovations in composite materials and processes to hit its targets*. <http://www.compositesworld.com/articles/boeing-787-update>. 2007.
- [4] D. H.-J. Lukaszewicz, C. Ward, and K. D. Potter, “The engineering aspects of automated prepreg layup: History, present and future”, *Composites Part B: Engineering*, vol. 43, no. 3, pp. 997–1009, 2012.
- [5] S. Bagherpour, *Fibre Reinforced Polyester Composites*, 2012.
- [6] J. Chen, D. S. Lussier, J. Cao, and X. Peng, “Materials characterization methods and material models for stamping of plain woven composites”, *International Journal of Forming Processes*, vol. 4, pp. 269–284, 2001.
- [7] A.C. Long, Ed, *Composites forming technologies*. Boca Raton: CRC Press [u.a.], 2007.
- [8] J. Cao, R. Akkerman, P. Boisse, J. Chen, H. S. Cheng, E. F. de Graaf, J. L. Gorczyca, P. Harrison, G. Hivet, J. Launay, W. Lee, L. Liu, S. V. Lomov, A. Long, E. de Luycker, F. Morestin, J. Padvoiskis, X. Q. Peng, J. Sherwood, T. Stoilova, X. M. Tao, I. Verpoest, A. Willems, J. Wiggers, T. X. Yu, and B. Zhu, “Characterization of mechanical behavior of woven fabrics: Experimental methods and benchmark results”, *Composites Part A: Applied Science and Manufacturing*, vol. 39, no. 6, pp. 1037–1053, 2008.
- [9] S. Bel, P. Boisse, and F. Dumont, “Analyses of the Deformation Mechanisms of Non-Crimp Fabric Composite Reinforcements during Preforming”, *Applied Composite Materials*, pp. 1–16, 2011.
- [10] P. Badel, E. Vidal-Sallé, E. Maire, and P. Boisse, “Simulation and tomography analysis of textile composite reinforcement deformation at the mesoscopic scale”, *Composites Science and Technology*, vol. 68, no. 12, pp. 2433–2440, 2008.
- [11] P. Boisse, A. Gasser, B. Hagege, and J.-L. Billoet, “Analysis of the mechanical behavior of woven fibrous material using virtual tests at the unit cell level”, *J Mater Sci*, vol. 40, no. 22, pp. 5955–5962, 2005.

- [12] R. Akkerman, B. Rietman, S. Haanappel, and U. Sachs, “Towards Design for Thermoplastic Composites Manufacturing Using Process Simulation” Bremen, 2012.
- [13] P. Boisse, “Simulations of Composite Reinforcement Forming” in *Woven Fabric Engineering*, P. D. Dubrovski, Ed.: InTech, 2010, pp. 387–414.
- [14] P. Boisse, B. ZOUARI, and A. Gasser, “A mesoscopic approach for the simulation of woven fibre composite forming”, *Composites Science and Technology*, vol. 65, no. 3-4, pp. 429–436, 2005.
- [15] T. Gereke, O. Döbrich, M. Hübner, and C. Cherif, “Experimental and computational composite textile reinforcement forming: A review”, *Composites Part A: Applied Science and Manufacturing*, vol. 46, pp. 1–10, 2013.
- [16] M. Duhovic and D. Bhattacharyya, “Simulating the deformation mechanisms of knitted fabric composites”, *Composites Part A: Applied Science and Manufacturing*, vol. 37, no. 11, pp. 1897–1915, 2006.
- [17] D. Durville, “Simulation of the mechanical behaviour of woven fabrics at the scale of fibers”, *Int J Mater Form*, vol. 3, no. S2, pp. 1241–1251, 2010.
- [18] A. C. Long and M. J. Clifford, “1. Composite forming mechanisms and materials characterisation” in *Woodhead Publishing in textiles, Composites forming technologies*, A. C. Long, Ed, Boca Raton: CRC Press [u.a.], 2007.
- [19] K. Drechsler, S. Bel, and D. Leutz, “Process Simulation and Material Modeling of Composites - 05 -Draping Simulation” München, 2013.
- [20] A. Willems, S. Lomov, I. Verpoest, and D. Vandepitte, “Optical strain fields in shear and tensile testing of textile reinforcements”, *Composites Science and Technology*, vol. 68, no. 3-4, pp. 807–819, 2008.
- [21] A.C. Long, Ed, *Design and Manufacture of Textile Composites*: Woodhead Publishing Limited, 2005.
- [22] J. Launay, G. Hivet, A. V. Duong, and P. Boisse, “Experimental analysis of the influence of tensions on in plane shear behaviour of woven composite reinforcements”, *Composites Science and Technology*, vol. 68, no. 2, pp. 506–515, 2008.
- [23] G. Hivet and A. V. Duong, “A contribution to the analysis of the intrinsic shear behavior of fabrics”, *Journal of Composite Materials*, vol. 45, no. 6, pp. 695–716, 2011.
- [24] S. V. Lomov, “Picture Frame Test of Woven Composite Reinforcements with a Full-Field Strain Registration”, *Textile Research Journal*, vol. 76, no. 3, pp. 243–252, 2006.

- [25] S. V. Lomov, M. Barbarski, T. Stoilova, I. Verpoest, R. Akkerman, R. Loendersloot, and R. H. W. Thije ten, “Carbon composites based on multiaxial multiply stitched preforms: Part 3: Biaxial tension, picture frame and compression tests of the preforms”, *Composites: Part A*, no. 36, pp. 1188–1206, 2005.
- [26] S. Haanappel and R. Akkerman, “Shear characterisation of uni-directional fibre reinforced thermoplastic melts by means of torsion”, *Composites Part A: Applied Science and Manufacturing*, vol. 56, pp. 8–26, 2014.
- [27] E. Bilbao, D. Soulat, G. Hivet, and A. Gasser, “Experimental Study of Bending Behaviour of Reinforcements”, *Exp Mech*, vol. 50, no. 3, pp. 333–351, 2010.
- [28] P. Boisse, N. Hamila, E. Vidal-Sallé, and F. Dumont, “Simulation of wrinkling during textile composite reinforcement forming. Influence of tensile, in-plane shear and bending stiffnesses”, *Composites Science and Technology*, vol. 71, no. 5, pp. 683–692, 2011.
- [29] J. Wang, A. C. Long, M. J. Clifford, H. Lin, E. Cueto, and F. Chinesta, “Energy Analysis of Reinforcement Deformations during Viscous Textile Composite Forming”, *AIP Conf. Proc.*, vol. 907, no. 1, pp. 1098–1106, 2007.
- [30] B. Liang, N. Hamila, M. Peillon, and P. Boisse, “Analysis of thermoplastic prepreg bending stiffness during manufacturing and of its influence on wrinkling simulations”, *Composites Part A: Applied Science and Manufacturing*, vol. 67, pp. 111–122, 2014.
- [31] E. Bilbao, D. Soulat, G. Hivet, J. Launay, and A. Gasser, “BENDING TEST OF COMPOSITE REINFORCEMENTS”, *Int J Mater Form*, vol. 1, no. S1, pp. 835–838, 2008.
- [32] T. K. Ghosh, S. K. Batra, and R. L. Barker, “The Bending Behaviour of Plain-woven Fabrics Part I: A Critical Review”, *Journal of The Textile Institute*, vol. 81, no. 3, pp. 245–254, 1990.
- [33] W. R. Yu, M. Zampaloni, F. Pourboghraat, K. Chung, and T. J. Kang, “Analysis of flexible bending behavior of woven preform using non-orthogonal constitutive equation”, *Composites Part A: Applied Science and Manufacturing*, vol. 36, no. 6, pp. 839–850, 2005.
- [34] F. T. Peirce, “26—THE “HANDLE” OF CLOTH AS A MEASURABLE QUANTITY”, *Journal of the Textile Institute Transactions*, vol. 21, no. 9, pp. T377, 1930.
- [35] P. Szablewski and W. Kobza, “Numerical Analysis of Peirce’s Cantilever Test for the Bending Rigidity of textiles”, *Fibres and Textiles in Eastern Europe*, vol. 11, no. 4, p. 43, 2003.

- [36] F. H. Hummel and W. B. Morton, “XXXII. On the large bending of thin flexible strips and the measurement of their elasticity”, *Philosophical Magazine Series 7*, vol. 4, no. 21, pp. 348–357, 1927.
- [37] *Bestimmung der Biegesteifigkeit - Verfahren nach Cantilever*, DIN 53362:2003-10, 2003.
- [38] *Prüfverfahren für Vliesstoffe*, DIN EN ISO 9073-7 : 1998, 1998.
- [39] S. Kawabata, *The standardization and analysis of hand evaluation*. Osaka, Japan: Textile Machinery Society of Japan, 1980.
- [40] S. V. Lomov, I. Verpoest, M. Barburski, and J. Laperre, “Carbon composites based on multiaxial multiply stiched preforms: Part 2. KES-F characterisation of the deformability of the preforms at low loads”, *Composites: Part A*, no. 34, pp. 359–370, 2003.
- [41] A. C. Long, P. Boisse, and F. Robitaille, “Mechanical analysis of textiles” in *Design and Manufacture of Textile Composites*, A. C. Long, Ed.: Woodhead Publishing Limited, 2005, pp. 62–109.
- [42] G. Hivet, J. Launay, A. Gasser, J. L. Daniel, and P. Boisse, “Mechanical Behavior of Woven Composite Reinforcements While Forming”, *Journal of Thermoplastic Composite Materials*, vol. 15, no. 6, pp. 545–555, 2002.
- [43] K. D. Potter, “In-plane and out-of-plane deformation properties of unidirectional preimpregnated reinforcement”, *Composites Part A: Applied Science and Manufacturing*, vol. 33, no. 11, pp. 1469–1477, 2002.
- [44] D. Leutz, M. Kluepfel, F. Dumont, R. Hinterhoelzl, K. Drechsler, C. Weimer, and G. Menary, “FE-Simulation of the Diaphragm Draping Process for NCF on a Macro-Scale Level”, *AIP Conference Proceedings*, vol. 1353, no. 1, pp. 1019–1024, 2011.
- [45] K. Fetfatsidis, L. Gamache, J. Gorczyca, J. Sherwood, D. Jauffrès, and J. Chen, “Design of an apparatus for measuring tool/fabric and fabric/fabric friction of woven-fabric composites during the thermostamping process” (English), *International Journal of Material Forming*, vol. 6, no. 1, pp. 1–11, 2013.
- [46] U. Sachs, S. Haanappel, B. Rietman, and R. Akkerman, “Friction testing of thermoplastic composites” Paris, 2011.
- [47] J. L. Gorczyca-Cole, J. A. Sherwood, and J. Chen, “A friction model for thermostamping commingled glass–polypropylene woven fabrics”, *Composites Part A: Applied Science and Manufacturing*, vol. 38, no. 2, pp. 393–406, 2007.
- [48] G. Lebrun, M. N. Bureau, and J. Denault, “Thermoforming-Stamping of Continuous Glass Fiber/Polypropylene Composites: Interlaminar and Tool–

- Laminate Shear Properties”, *J Thermoplast Compos*, vol. 17, no. 2, pp. 137–165, 2004.
- [49] R. H. W. ten Thije, R. Akkerman, L. Meer, and M. P. Ubbink, “Tool-ply friction in thermoplastic composite forming”, *Int J Mater Form*, vol. 1, no. S1, pp. 953–956, 2008.
- [50] J. L. Gorczyca, “Modeling of Friction and Shear in Thermostamping of Composites - Part I”, *Journal of Composite Materials*, vol. 38, no. 21, pp. 1911–1929, 2004.
- [51] G. Hivet, S. Allaoui, B. T. Cam, P. Ouagne, and D. Soulat, “Design and Potentiality of an Apparatus for Measuring Yarn/Yarn and Fabric/Fabric Friction”, *Exp Mech*, vol. 52, no. 8, pp. 1123–1136, 2012.
- [52] S. Haanappel, U. Sachs, R. Thije ten, B. Rietman, and R. Akkerman, “Shear Characterisation of UD Thermoplastic Composites” Auckland, 2011.
- [53] Y. R. Kim, S. P. McCarthy, and J. P. Fanucci, “Compressibility and relaxation of fiber reinforcements during composite processing”, *Polym. Compos*, vol. 12, no. 1, pp. 13–19, 1991.
- [54] P. Hubert and A. Poursartip, “A method for the direct measurement of the fibre bed compaction curve of composite prepregs”, *Composites Part A: Applied Science and Manufacturing*, vol. 32, no. 2, pp. 179–187, Feb. 2001.
- [55] M. Li, Y. Gu, Z. Zhang, and Z. Sun, “A simple method for the measurement of compaction and corresponding transverse permeability of composite prepregs”, *Polym Compos*, vol. 28, no. 1, pp. 61–70, Feb. 2007.
- [56] T.-C. Lim and S. Ramakrishna, “Modelling of composite sheet forming: a review”, *Composites Part A: Applied Science and Manufacturing*, vol. 33, no. 4, pp. 515–537, 2002.
- [57] R. Akkerman and E. A. D. Lamers, “2. Constitutive modelling for composite forming” in *Woodhead Publishing in textiles, Composites forming technologies*, A. C. Long, Ed, Boca Raton: CRC Press [u.a.], 2007.
- [58] P. Boisse, J. Cao, N. Hamila, F. Helenon, and B. Hagege, “Different approaches for woven composite reinforcement forming simulation”, *Int J Mater Form - Springer*, 2008.
- [59] C. Mack and H. M. Taylor, “The fitting of woven cloth to surfaces”, *Journal of The Textile Institute*, vol. 47, no. 8, pp. 477–488, 1956.
- [60] A. C. Long and C. D. Rudd, “A simulation of reinforcement deformation during the production of preforms for liquid moulding processes”, *ARCHIVE: Proceedings of the Institution of Mechanical Engineers, Part B: Journal of*

- Engineering Manufacture 1989-1996 (vols 203-210)*, vol. 208, no. 42, pp. 269–278, 1994.
- [61] F. van der Weeën, “Algorithms for draping fabrics on doubly-curved surfaces”, *Int. J. Numer. Meth. Engng*, vol. 31, no. 7, pp. 1415–1426, Mai. 1991.
- [62] A. C. Long, B. J. Souter, F. Robitaille, and C. D. Rudd, “Effects of fibre architecture on reinforcement fabric deformation”, *plas. rub. compos*, vol. 31, no. 2, pp. 87–97, 2002.
- [63] E.A.D. Lamers, S. Wijskamp, and R. Akkerman, Eds, *Modelling of fabric draping: Finite elements versus a geometrical method*. Liège (B), 2001.
- [64] N. Hamila, P. Boisse, F. Sabourin, and M. Brunet, “A semi-discrete shell finite element for textile composite reinforcement forming simulation”, *Int. J. Numer. Meth. Engng*, vol. 79, no. 12, pp. 1443–1466, 2009.
- [65] R. ten Thije, R. Akkerman, and J. Huétink, “Large deformation simulation of anisotropic material using an updated Lagrangian finite element method”, *Computer Methods in Applied Mechanics and Engineering*, vol. 196, no. 33-34, pp. 3141–3150, 2007.
- [66] S. Gatouillat, A. Bareggi, E. Vidal-Sallé, and P. Boisse, “Meso modelling for composite preform shaping – Simulation of the loss of cohesion of the woven fibre network”, *Composites Part A: Applied Science and Manufacturing*, vol. 54, no. 0, pp. 135–144, 2013.
- [67] Y. Aimène, E. Vidal-Sallé, B. Hagège, F. Sidoroff, and P. Boisse, “A Hyperelastic Approach for Composite Reinforcement Large Deformation Analysis”, *Journal of Composite Materials*, vol. 44, no. 1, pp. 5–26, 2010.
- [68] P. Badel, S. Gauthier, E. Vidal-Sallé, and P. Boisse, “Rate constitutive equations for computational analyses of textile composite reinforcement mechanical behaviour during forming”, *Composites Part A: Applied Science and Manufacturing*, vol. 40, no. 8, pp. 997–1007, 2009.
- [69] L. Dong, C. Lekakou, and M. G. Bader, “Processing of Composites: Simulations of the Draping of Fabrics with Updated Material Behaviour Law”, *Journal of Composite Materials*, vol. 35, no. 2, pp. 138–163, 2001.
- [70] R. H. W. ten Thije and R. Akkerman, “A multi-layer triangular membrane finite element for the forming simulation of laminated composites”, *Composites Part A: Applied Science and Manufacturing*, vol. 40, no. 6-7, pp. 739–753, 2009.
- [71] R. H. W. ten Thije and R. Akkerman, “Finite Element Simulation of laminated composites forming processes” vorgetragen von Haanappel. Brescia (Italien), Apr. 2010.

- [72] P. Wang, N. Hamila, and P. Boisse, “Numerical simulation of multi-layered textile composite reinforcement forming”, *AIP Conference Proceedings*, vol. 1353, no. 1, pp. 918–923, 2011.
- [73] N. Hamila and P. Boisse, “Tension locking in finite-element analyses of textile composite reinforcement deformation”, *Comptes Rendus Mécanique*, vol. 341, no. 6, pp. 508–519, 2013.
- [74] S. Bel, N. Hamila, P. Boisse, and F. Dumont, “Finite element model for NCF composite reinforcement preforming: Importance of inter-ply sliding”, *Composites Part A: Applied Science and Manufacturing*, vol. 43, no. 12, pp. 2269–2277, 2012.
- [75] A. Cherouat and J. L. Billoët, “Mechanical and numerical modelling of composite manufacturing processes deep-drawing and laying-up of thin pre-impregnated woven fabrics”, *PART 1: CONTAINING PAPERS PRESENTED AT INTERNATIONAL CONFERENCE ON ADVANCES IN MATERIALS PROCESSING TECHNOLOGY*, vol. 118, no. 1–3, pp. 460–471, 2001.
- [76] L. Liu, J. Chen, X. Li, and J. Sherwood, “Two-dimensional macro-mechanics shear models of woven fabrics”, *Composites Part A: Applied Science and Manufacturing*, vol. 36, no. 1, pp. 105–114, 2005.
- [77] X. Q. Peng and J. Cao, “A continuum mechanics-based non-orthogonal constitutive model for woven composite fabrics”, *Composites Part A: Applied Science and Manufacturing*, vol. 36, no. 6, pp. 859–874, 2005.
- [78] P. Harrison, R. Gomes, and N. Curado-Correia, “Press forming a 0/90 cross-ply advanced thermoplastic composite using the double-dome benchmark geometry”, *Composites Part A: Applied Science and Manufacturing*, vol. 54, pp. 56–69, 2013.
- [79] O. Döbrich, T. Gereke, C. Cherif, and S. Krzywinski, “Analysis and finite element simulation of the draping process of multilayer knit structures and the effects of a localized fixation”, *Advanced Composite Materials*, vol. 22, no. 3, pp. 175–189, 2013.
- [80] ESI Group, *PAM-FORM 2009: Solver Notes*, 2009.
- [81] A. Margossian, S. Bel, J. M. Balvers, D. Leutz, R. Freitas, and R. Hinterhoelzl, “Finite element forming simulation of locally stitched non-crimp fabrics”, *Composites Part A: Applied Science and Manufacturing*, vol. 61, pp. 152–162, 2014.
- [82] A. K. Pickett, G. Creech, and P. de Luca, “Simplified and advanced simulation methods for prediction of fabric draping”, *Revue Européenne des Éléments*, vol. 14, no. 6-7, pp. 677–691, 2005.

- [83] G. Creech and A. K. Pickett, “Meso-modelling of Non-Crimp Fabric composites for coupled drape and failure analysis”, *J Mater Sci*, no. 41, pp. 6725–6736, 2006.
- [84] B. B. Boubaker, B. Haussy, and J.-F. Ganghoffer, “Mesoscopic fabric models using a discrete mass-spring approach: Yarn-yarn interactions analysis”, *J Mater Sci*, vol. 40, no. 22, pp. 5925–5932, 2005.
- [85] E. Vidal-Sallé, Q. Nguyen, A. Charmetant, J. Bréard, E. Maire, and P. Boisse, “Use of numerical simulation of woven reinforcement forming at mesoscale: Influence of transverse compression on the global response”, *International Journal of Material Forming*, vol. 3, pp. 699–702, 2010.
- [86] P. Boisse, Y. Aimène, A. Dogui, S. Dridi, S. Gatouillat, N. Hamila, M. Aurangzeb Khan, T. Mabrouki, F. Morestin, and E. Vidal-Sallé, “Hypoelastic, hyperelastic, discrete and semi-discrete approaches for textile composite reinforcement forming” (English), *Int J Mater Form*, vol. 3, no. 2, pp. 1229-1240, 2010.
- [87] N. Hamila and P. Boisse, “Locking in simulation of composite reinforcement deformations. Analysis and treatment”, *Composites Part A: Applied Science and Manufacturing*, vol. 53, no. 0, pp. 109–117, 2013.
- [88] X. Yu, B. Cartwright, D. McGuckin, L. Ye, and Y.-W. Mai, “Intra-ply shear locking in finite element analyses of woven fabric forming processes”, *Composites Part A: Applied Science and Manufacturing*, vol. 37, no. 5, pp. 790–803, 2006.
- [89] R. ten Thije and R. Akkerman, “Solutions to intra-ply shear locking in finite element analyses of fibre reinforced materials”, *Composites Part A: Applied Science and Manufacturing*, vol. 39, no. 7, pp. 1167–1176, 2008.
- [90] P. Harrison, M. J. Clifford, and A. C. Long, “Shear characterisation of viscous woven textile composites: a comparison between picture frame and bias extension experiments”, *Composites Science and Technology*, vol. 64, no. 10-11, pp. 1453–1465, 2004.
- [91] M. Birnkammer, “Entwicklung von Prüfständen zur Charakterisierung von Faserverbundtextilien für die numerische Simulation des Drapierprozesses” Diplomarbeit, Lehrstuhl für Carbon Composites, Technische Universität München, München, 2011.
- [92] K. Potter, “Bias extension measurements on cross-plyed unidirectional prepreg”, *Composites Part A: Applied Science and Manufacturing*, vol. 33, no. 1, pp. 63–73, 2002.
- [93] M. Hübner, O. Diestel, C. Sennewald, T. Gereke, and C. Cherif, “Simulation of the Drapability of Textile Semi-Finished Products with Gradient-

- Drapability Characteristics by Varying the Fabric Weave”, *Fibres & Textiles in Eastern Europe*, vol. 20, no. 5, pp. 88–93, 2012.
- [94] K. Potter, “Bias extension measurements on cross-ply unidirectional prepreg”, *Composites Part A: Applied Science and Manufacturing*, vol. 33, no. 1, pp. 63–73, 2002.
- [95] R. H. W. ten Thije, R. Loendersloot, and R. Akkerman, “Material characterisation for Finite Element simulations of draping with non-crimp fabrics”, 2003.
- [96] J. Cao, H.S. Cheng, T.X. Yu, B. Zhu, X.M. Tao, S.V. Lomov, T. Stoilova, I. Verpoest, P. Boisse, and J. Launay, Eds, *A cooperative benchmark effort on testing of woven composites: Proceedings of the seventh Esaform conference on material forming, Trondheim, Norway*, 2004.
- [97] S.P. Haanappel, R. Thije ten, U. Sachs, A.D. Rietman, and R. Akkerman, “In-Plane Shear Characterisation of Uni-Directionally Reinforced Thermoplastic Melts” in *The 14th International ESAFORM Conference on Material Forming*: American Institute of Physics, 2011, pp. 930-935.
- [98] P. Badel, E. Vidal-Sallé, and P. Boisse, “Computational determination of in-plane shear mechanical behaviour of textile composite reinforcements”, *Computational Materials Science*, vol. 40, no. 4, pp. 439–448, 2007.
- [99] *Standard Test Method for Stiffness of Fabrics*, ASTM D 1388 – 96, 1999.
- [100] U. J. Santner, “Materialcharakterisierung von CFK Halbzeugen für den Drapierprozess” Semesterarbeit, Lehrstuhl für Carbon Composites, Technische Universität München, München, 2012.
- [101] *Bestimmung der Biegesteifigkeit - Verfahren nach Schlenker*, DIN 53864, 1978.
- [102] L. Dong, C. Lekakou, and M. G. Bader, “Solid-mechanics finite element simulations of the draping of fabrics: a sensitivity analysis”, *Composites Part A: Applied Science and Manufacturing*, vol. 31, no. 7, pp. 639–652, 2000.
- [103] *Mit Kautschuk oder Kunststoff beschichtete Textilien - Bestimmung der Koeffizienten von Haftreibung und Bewegungsreibung*, DIN EN 14882:2005, 2005.
- [104] *Standard Test Method for Static and Kinetic Coefficients of Friction of Plastic Film and Sheeting*, ASTM D 1894-01, 2001.
- [105] U. Sachs, K. A. Fetfatsidis, J. Schumacher, G. Ziegmann, S. Allaoui, G. Hivet, E. Vidal-Salle, and R. Akkerman, “A Friction-Test Benchmark with Twintex PP”, *KEM*, vol. 504-506, pp. 307–312, 2012.
- [106] K. Vanclooster, S. V. Lomov, and I. Verpoest, “Investigation of interply shear in composite forming”, *Int J Mater Form*, vol. 1, no. S1, pp. 957–960, 2008.

-
- [107] U. J. Santner, “FE Simulation of Composite Textile Tests for Setting up Material Cards” Diploma Thesis, Lehrstuhl für Carbon Composites, Technische Universität München, München, 2013.
- [108] R. ten Thije, “Finite element simulations of laminated composites forming processes” Dissertation, Universiteit Twente, 2007.
- [109] A. Schug, “Validation Method for Evaluating Forming Simulations of Composite Textiles” Diplomarbeit, Lehrstuhl für Carbon Composites, Technische Universität München, München, 2013.
- [110] W. Palfinger, S. Thumfart, and C. Eitzinger, “Photometric stereo on carbon fiber surfaces”, Machine Vision Department, Profactor GmbH, Steyr-Gleink, Austria, Mai. 2011.
- [111] S. Thumfart, W. Palfinger, M. Stöger, and C. Eitzinger, “Accurate Fibre Orientation Measurement for Carbon Fibre Surfaces” in *Lecture Notes in Computer Science, Computer Analysis of Images and Patterns*, R. Wilson, E. Hancock, A. Bors, and W. Smith, Eds.: Springer Berlin Heidelberg, 2013, pp. 75–82.
- [112] A. Margossian, M. Ding, L. Avila Gray, S. Bel, and R. Hinterhölzl, “Flexural Characterisation of Unidirectional Thermoplastic Tapes using a Dynamic Mechanical Analysis system” in *ECCM 16*

A Appendix

Tab. A-1 Stress-strain curve definition for the AFP material in E2-direction

ϵ_{ln}	σ_T
0	0
0.02	2.1 e-5
0.04	3.1 e-5
0.06	3.7 e-5
0.08	3.8 e-5
0.1	3.7 e-5
0.15	3.1 e-5
0.2	2.7 e-5
0.3	2.5 e-5

Tab. A-2 Shear modulus vs. frame angle definition for the AFP material in E2-direction

$\cos(\phi)$	G^* $\cos(\phi)$	$\cos(\phi)$	G^* $\cos(\phi)$	$\cos(\phi)$	G^* $\cos(\phi)$
0	0.0 e0	0.017756	1.2 e-5	0.2628	1.1 e-5
0.000707	5.0 e-6	0.021326	1.2 e-5	0.302843	9.0 e-6
0.001415	6.0 e-6	0.028484	1.3 e-5	0.343511	6.0 e-6
0.001769	7.0 e-6	0.035668	1.4 e-5	0.384803	4.0 e-6
0.002122	7.0 e-6	0.042876	1.4 e-5	0.426721	1.0 e-9
0.00283	8.0 e-6	0.05011	1.4 e-5	0.469264	1.0 e-9
0.003539	9.0 e-6	0.057369	1.5 e-5	0.512432	1.0 e-9
0.00531	1.0 e-5	0.071961	1.5 e-5	0.556225	1.0 e-9
0.007084	1.1 e-5	0.108879	1.5 e-5	0.600643	1.0 e-9
0.010635	1.1 e-5	0.146421	1.4 e-5	0.645685	1.0 e-9
0.014192	1.2 e-5	0.223382	1.3 e-5		

B Publications

Journal Papers

- [P1] D. Leutz, T. Wallmersperger “Thermo-Mechanical Behavior of Functionally Graded Materials: Modeling, Simulation and Error Estimation”, *Mechanics of Advanced Materials and Structures*, vol. 18, iss. 1, 2011.
- [P2] A. Margossian, S. Bel, J. Balvers, D. Leutz, R. Freitas, R. Hinterhoelzl, “Finite element forming simulation of locally stitched non-crimp fabrics”, *Composites Part A: Applied Science and Manufacturing*, vol. 61, pp. 152–162, 2014.
- [P3] D. Leutz, M. Vermilyea, S. Bel, R. Hinterhölzl, “Forming simulation of AFP laminates and validation with live CT imaging”, submitted to: *International Journal of Material Forming*

Conference Proceedings / Presentations

- [C1] D. Leutz, M. Kluepfel, F. Dumont, R. Hinterhoelzl, K. Drechsler, C. Weimer, “FE-Simulation of the Diaphragm Draping Process for NCF on a Macro-Scale Level”, *ESAFORM conference proceedings*, Brescia, 2011.
- [C2] D. Leutz, R. Hinterhoelzl, K. Drechsler, “FE-Simulation of the Diaphragm Draping Process for NCF on a Macro-Scale Level”, *EUCOMAS Conference*, Hamburg, 2012
- [C3] D. Leutz, M. Kluepfel, A. Margossian, S. Bel, F. Dumont, C. Weimer, K. Drechsler, “Virtual Stitches in Formability Studies of NCF Preforms”, *8th European Solid Mechanics Conference*, Graz, 2012
- [C4] D. Leutz, S. Bel, R. Hinterhoelzl, K. Drechsler, “Forming Simulation for Part and Process Development”, *CCeV Faser-Verbund-Werkstoff-Simulationstag*, Augsburg, 2012
- [C5] D. Leutz, S. Bel, A. Schug, R. Hinterhoelzl, K. Drechsler, “New Approaches of Testing and Validating CFRP Composite Textiles for Forming Simulation”, *ESAFORM conference*, Aveiro, 2013

C Advised student works

In the following all student works are lists which had been advised by the author.

- [S1] M. Maier, "Entwicklung einer Matlab Routine zur geometrischen, analytischen Flechtsimulation", Semesterarbeit, LCC, TUM, 2010
- [S2] M. Moeller Bichler, "Entwicklung einer Konstruktionsmethodik für Faserverbundbauteile in Catia V5 Composite Design", Semesterarbeit, LCC, TUM, 2010
- [S3] M. Birnkammer, "Entwicklung von Prüfständen zur Charakterisierung von Faserverbundtextilien für die numerische Simulation des Entwicklung von Prüfständen zur Charakterisierung von Faserverbundtextilien für die numerische Simulation des Drapierprozesses", Diplomarbeit, LCC, TUM, 2011
- [S4] J. Assenbrunner, "Optimiertes Drapieren einer Kajakspitze mittels kinematischer Drapiersimulation unter Verwendung von PAM-QuikForm", Semesterarbeit, LCC, TUM, 2011
- [S5] A. Boeck, "FE-basierte Drapiersimulation von CFK-Textilien mittels Abaqus/Explicit", Bachelor Thesis, LCC, TUM, 2011
- [S6] M. Schieber, "Benchmarkstudie analytischer Flechtsimulationen in der Faserverbundtechnologie", Semesterarbeit, LCC, TUM, 2011
- [S7] U. Santner, "Materialcharakterisierung von CFK Halbzeugen für den Drapierprozess", Semesterarbeit, LCC, TUM, 2012
- [S8] M. Maier, "Finite Element Modeling of the Double Diaphragm Forming Process for Plain 2D/2,5D Composite Layer Structures", Diplomarbeit mit Airbus Helicopters, LCC, TUM, 2012
- [S9] M. Kluepfel, "Modelling of production processes for multi-ply preforming operations", Diplomarbeit, LCC, TUM, 2012
- [S10] J. Glaser, "Befähigung eines Drucksensorsystems für die Messung von Textilien im 3D-Drapierprozess", Master Thesis mit BMW Group, LCC, TUM, 2013
- [S11] A. Schug, "Validation Method for Evaluating Forming Simulations of Composite Textiles", Diplomarbeit, LCC, TUM, 2013

- [S12] A. v. Biberstein, “Konstruktion eines Diaphragma-Prozesses zur Drapierung von Carbonfaser-Prepregs auf einer Thermoformpresse“, Diplomarbeit, LCC, TUM, 2013
- [S13] M. Pernicka, “Development and construction of a stamp forming process to validate the draping simulation“, Semesterarbeit, LCC, TUM, 2013
- [S14] U. Santner, “FE Simulation of Composite Textile Tests for Setting up Material Cards“, Diplomarbeit, LCC, TUM, 2013
- [S15] T. Steffen, “Material-Charakterisierung für ein Drapiersimulationstool und deren Validierung“, Semesterarbeit, LCC, TUM, 2013
- [H1] C. Hirth, Studentische Hilfskraft, LCC, TUM, 2010/11
- [H2] M. Maier, Studentische Hilfskraft, LCC, TUM, 2011
- [H3] M. Kluepfel, Studentische Hilfskraft, LCC, TUM, 2011/12
- [H4] U. Santner, Studentische Hilfskraft, LCC, TUM, 2012
- [H5] J. Haderlein, Forschungspraktikum, LCC, TUM, 2013

Following student works partly contributed to this work: [S3], [S5], [S7], [S8], [S9], [S10], [S11], [S12], [S13], [S14], [S15], [H1], [H2], [H3], [H4] & [H5]